

# Forward and Side Two Dimensional Scattered Light Patterns Studies of Single Cell for Label-Free Flow Cytometry

by

Hesam Shahin

A thesis submitted in partial fulfillment of the requirements for the degree of

Master of Science

in

Microsystems and Nanodevices

Department of Electrical and Computer Engineering

University of Alberta

©Hesam Shahin, 2016

## **Abstract**

A technique using two dimensional scattered light patterns from single cells to extract useful information from cells has been investigated experimentally and numerically. The technique can be implemented in label-free cytometry as an alternative to conventional fluorescent-activated flow cytometry. In this thesis two dimensional scattered light patterns in both forward and side directions from latex beads with spherical and elliptical shapes, Hematopoietic Stem Cells and Very Small Embryonic Like Stem Cells have been studied. The ability to measure the patterns of a cell in forward and side direction simultaneously is an important step forward for such technique. In particular it has been demonstrated that useful information of a cell under investigation including the size and shape of its nucleus and its mitochondria distribution can be obtained from its simultaneously captured forward and side two dimensional scattered light patterns.

## **Dedication**

To my dad, mom and my sister ...

## **Acknowledgments**

I would like to express my sincere gratitude to my supervisor Dr. Ying Yin Tsui for the continuous support of my study and related research, for his patience, motivation, and immense knowledge. I would like to appreciate my co-supervisor Dr. Wojciech Rozmus for many meetings, conversations and precious support. My sincere thanks go to Dr. Manisha Gupta and Dr. Anna Janowska-Wieczorek who helped me with their comments in this work.

Last but not the least, I would like to thank my family: my parents and my sister for supporting me spiritually throughout writing this thesis and my life in general.

# Table of Contents

<b>1. Introduction .....</b>	<b>1</b>
1.1. Current technologies involve with cell sorting and detection .....	1
1.2. Structure of a cell .....	2
1.3. Stem cells .....	4
1.4. Hematopoietic vs. non-hematopoietic stem cells .....	5
1.5. Our approach and thesis's goals .....	8
<b>2. Background .....</b>	<b>10</b>
2.1. Fluorescence-activated flow cytometry .....	10
2.2. Laser light scattering studies of single cell .....	15
2.3. Mie scattering theory.....	17
2.4. FDTD method .....	25
2.4.1. Yee's algorithm .....	25
2.4.2. Grid consideration.....	28
2.4.3. Near-to-Far field transformation (NTF).....	29
2.4.4. Validation of the numerical AETHER code .....	31
2.5. Full angle scattering benefits.....	32
2.6. Viewing angle detection.....	32
<b>3. Light scattering study of beads.....</b>	<b>38</b>
3.1. Introduction .....	38
3.1.1. Setup design .....	38
3.2. Polystyrene spherical beads experimental and simulated results.....	44
3.3. Beads radius vs. periodic harmonics .....	46
3.4. Elliptical polystyrene latex beads.....	48
<b>4. Light scattering study of cells .....</b>	<b>54</b>
4.1. Introduction .....	54
4.2. Nucleus.....	54
4.2.1. Nucleus size changes .....	55

4.2.2.	Non-spherical nucleus.....	60
4.3.	Mitochondria .....	63
4.3.1.	Mitochondria's distribution .....	65
4.4.	Light scattering from umbilical cord blood hematopoietic stem cells.....	67
4.5.	Umbilical cord blood very small embryonic-like stem cells light scattering study .....	72
<b>5.</b>	<b>Conclusions.....</b>	<b>79</b>
5.1.	Summary .....	79
5.2.	Future work .....	80
	<b>References.....</b>	<b>83</b>
	<b>Appendices.....</b>	<b>89</b>
A.1.	AETHER code compilations and code run .....	89
A.1.1.	Compiling and running AETHER codes .....	89
A.1.2.	Extracting and plotting results input values.....	91
A.1.3.	Spherical polystyrene bead .....	91
A.1.4.	Non-spherical polystyrene bead input values .....	93
A.1.5.	Biological cell input values.....	94
A.2.	Comments on laser used for light scattering of cells .....	97
A.3.	Speckle analysis .....	101

## List of Tables

Table 1.1: Properties of internal components in an eukaryotic cell [24-27].....	3
Table 4.1: Parametes for necleus and cytoplasm used in the simulations with results presented in Figure 4.7 .....	62

# List of Figures

Figure 1.1: Illustration of biological cell showing internal parts and some organelles. .... 2

Figure 1.2: Human body stem cells hierarchy. .... 5

Figure 1.3: Model of the human hematopoietic hierarchy. Very primitive **CD34** – HSCs are able to produce primitive **CD34** + HSCs. [34]..... 7

Figure 2.1: A schematic of hydrodynamic focusing process in a flow cytometer..... 11

Figure 2.2: A schematic diagram of a FACS flow cytometer..... 12

Figure 2.3: 2D histogram analysis of FACS. What it appears to be a single population in FSC or SSC axis, can be a combination of different cell type population. .... 13

Figure 2.4: This schematic depicts the process of attaching fluorescent antibody to the target protein in/on the cell. .... 14

Figure 2.5: Information contained in angular light scattering. .... 16

Figure 2.6: Light scattering geometry for a single scatterer is shown in this figure. The incident wave propagates along the +z direction, the scattered wave has a polar angle “ $\theta$ ” and an azimuth angle “ $\phi$ ” as shown in the figure. ( r,  $\theta$ ,  $\phi$ ) defines the spherical coordinates. The spherical scatterer with a radius “r” is centered at the origin. .... 19

Figure 2.7: Validation of MiePlot program results in full angular range. .... 24

Figure 2.8: Electric and magnetic field vector components in the Yee's space lattice are shown in this figure. .... 26

Figure 2.9: The geometry of the FDTD computational domain. .... 29

Figure 2.10: AETHER FDTD code validation compared with Mie simulation results..... 31

Figure 2.11: Two viewing angles are separated with dashed lines on AETHER simulated results for numerical model of 3  $\mu\text{m}$  radius bead. .... 33

Figure 2.12: This figure illustrates the small difference of scattered pattern observed on the surface of sphere comparing to the scattered pattern observed on the surface of CCD camera... 34

Figure 2.13: This figure shows the viewing cone angle ..... 35

Figure 2.14: This figure shows a simulated scattered pattern mapped on the surface of sphere (left) and the simulated pattern expanded on the flat surface of CCD (right). .... 37

Figure 3.1: Improved new designed experimental setup used in this project. Two viewing windows are shown aligned with side and forward direction's cameras. A laser light will be focused in the middle of new designed cuvette. .... 39

Figure 3.2: The scattered light beam will pass three medium with different refractive indices as it propagates from the scatterer to be observed by lens. .... 41

Figure 3.3: The cuvette designed with forward and side direction windows. .... 42

Figure 3.4: Top view schematic of cone volume movements in forward and side directions from position “A” to “B” for 300  $\mu\text{m}$  in forward and 200  $\mu\text{m}$  in side directions..... 43

Figure 3.5: Optical fiber used to calibrate and focused two optical systems to same area. Focused images of optical fiber and defocused images are shown. 2 beads captured in (D) are circled red. .....	44
Figure 3.6: Simulated MiePlot results for beads of 4 $\mu\text{m}$ , 6 $\mu\text{m}$ and 10 $\mu\text{m}$ diameter sizes in PBS solution.....	45
Figure 3.7: Observed forward and side direction scattered patterns from polystyrene latex beads diluted PBS solution. A-A' shows the 2-3 fringes in forward and 4 fringes in side direction. B-B' show 5 fringes in forward and side directions. There are 7 fringes in forward and 8 fringes in side direction of 10 $\mu\text{m}$ bead's scattered patterns (C-C')......	46
Figure 3.8: (A)-(C) shows the simulated forward direction 2D light scattered pattern of 4 $\mu\text{m}$ , 6 $\mu\text{m}$ and 10 $\mu\text{m}$ diameter size plastic bead respectively, dashed red line in the input values for 1D FFT function. (D) shows the measured horizontal frequency peaks of (A)-(C).....	47
Figure 3.9: Most dominant 1D FFT horizontal frequency comparison of forward direction 2D light scattered patterns of experimental and numerical results for polystyrene beads. ....	48
Figure 3.10: Experimental ellipsoid geometry dimensions. ....	48
Figure 3.11: Experimentally scattered patterns from elliptical latex beads sample. ....	49
Figure 3.12: Numerical elliptical shape models are presented in this figure. Model A shows the elliptical bead along the X-axis and the scattering patterns are shown. Model B and C show elliptical bead along Y-axis and Z-axis generated scattering patterns respectively. ....	50
Figure 3.13: This figure illustrates the geometry that laser beam traveling along the Z-axis sees on XY-plane cross-section of each of elliptical bead rotations shown in Figure 3.12. ....	51
Figure 3.14: Aspect ratio changes are studied with use of numerical modeling and AETHER simulated results presented in this figure. The elliptical aspect ratio of $r_z r_y$ changed from 1-0.1 in presented A-J models. The fringes orient as the aspect ratio varies from A-J. ....	51
Figure 3.15: Simulated scattered patterns of aspect ratio variations in forward and side directions for $0^\circ < \varphi < 180^\circ$ .....	52
Figure 3.16: Ellipsoid rotation is shown in this figure. Ellipsoid rotates over fixed $\varphi$ ( $\varphi = 90^\circ$ ) for A) $\theta = 0^\circ$ , B) $\theta = 22.5^\circ$ , C) $\theta = 45^\circ$ , D) $\theta = 67.5^\circ$ and E) $\theta = 90^\circ$ . Scattered patterns are simulated as shown in two directions of forward and side. Orientation of fringes can be seen due to ellipsoid rotation. ....	53
Figure 4.1: This figure shows the simulated forward direction patterns for A) solo cytoplasm, B) solo nucleus and C) cytoplasm and nucleus as whole cell.....	55
Figure 4.2: (A) Square area to be extracted for 2D FFT process. (B) Frequencies magnitude 2D plot as FFT function output.....	56
Figure 4.3: 1D FFT analysis of forward patterns in Figure 4.1 .....	57
Figure 4.4: Simulated forward 2D scattered light patterns with various nucleus/cytoplasm size ratio. ....	58
Figure 4.5: 1D FFT spectra of forward scattered light patterns in Figure 4.4. ....	59
Figure 4.6: The 2D scattered light patterns of spherical cytoplasm only (A-A'), elliptical nucleus only (B-B') and elliptical nucleus inside a spherical cytoplasm (C-C'). ....	61

Figure 4.7: Simulated 2D scattered light patterns from systems with nucleus and cytoplasm with various combinations of shapes defined in Table 4.1 .....	62
Figure 4.8: The simulated 2D scattered light patterns of due to various mitochondria's distributions.....	65
Figure 4.9: Experimental scattered light patterns for UCB HSCs in the forward and side directions.....	68
Figure 4.10: The simulated 2D scattered light patterns for cell models with spherical nucleus and several different mitochondria distributions. ....	69
Figure 4.11: The average area ratio over the number of the speckle peaks for UCB HSC's numerical models and experimental results side direction 2D light scattered patterns. ....	71
Figure 4.12: Experimental 2D scattered light patterns of UCB VSEL stem cells observed simultaneous in both forward and side directions.....	73
Figure 4.13: Images A-C presents TEM images of CB-derived VSELS. They possess a relatively large nucleus surrounded by a narrow rim of cytoplasm. This narrow rim of cytoplasm possesses a few mitochondria [35]. Non-spherical shape nucleus can be seen in these pictures. D-F pictures show VSEL cells microscope images. ....	74
Figure 4.14: Numerical models used for UCB VSEL simulations. These models consist of spherical/ellipsoid shape nucleus/cytoplasm and some small mitochondria placed in thin rim of nucleus and cytoplasm. Forward and side directions patterns are shown.....	76
Figure 5.1: This figure shows a prototype of identification part of multi-angle label-free cytometer machine (FSC=Forward Scattered Camera, SSC=Side Scattered Camera) .....	82

## List of Symbols

1D	one-dimensional
2D	two-dimensional
3D	three-dimensional
CB	cord blood
ABC	absorbing boundary condition
$c$	light speed in vacuum
CCD	charge coupled device
$\delta$	step size
$\Delta t$	time step size
$\Delta x$	space grid spacing along x axis
FFT	fast Fourier transform
$\vec{E}$	electric field
ESC	embryonic stem cells
$\epsilon$	permittivity
FACS	fluorescence-activated cell sorting
FDTD	Finite-Difference Time-Domain
FWHM	full width half maximum
FSC	forward scattered camera
fps	frame per second
GB	Gigabyte
HSC	hematopoietic stem cells
$\vec{H}$	magnetic field
$I$	intensity
$\vec{J}_s$	electric currents
$\vec{k}$	wave propagation vector
$\lambda$	wavelength
LOC	lab-on-chip
$m$	relative refractive index

$\vec{M}_s$	magnetic currents
$\mu m$	micrometer
$\mu$	permeability
mL	milliliter
mm	millimeter
mW	mill-watt
NA	numerical aperture
nm	nanometer
$n$	refractive index
$\omega$	angular frequency
$P_n^m$	associated Legendre functions
PB	peripheral blood
PBS	phosphate buffered saline
PDMS	polydimethylsiloxane
$\varphi$	azimuth angle
PML	perfectly matched layer
RBC	red blood cell
SC	stem cell
SSC	side scattered camera
$s$	second
S	element of the scattering amplitude matrix
S/N	signal to noise
$t$	amplitude transmission coefficient
T	transmission
TE	transverse electric
TF/SF	total-field/scattered-field
$\theta$	polar angle
TM	transverse magnetic
VSEL	very small embryonic like stem cell
UCB	umbilical cord blood
$z_n$	spherical Bessel functions

# 1. Introduction

## 1.1. Current technologies involve with cell sorting and detection

For years, the technique using labeling with fluorescence biomarkers has been used to identify and sort interested cell line<sup>1</sup> by researchers and technicians in scientific laboratories and clinical facilities. The labeling technique is used in flow cytometry as a pre-process step. Adding fluorescent light emitting bio-labels to the target cell line make the cell line identifiable in a mixture with other cell lines in the sample. However, finding unique bio-label for a cell line is a time consuming process and could be expensive. Additionally, many labeling steps may be needed to uniquely identify a target cell line. As an example, it takes 6-12 labeling steps to sort very small embryonic like (VSEL) stem cells (SCs) from an umbilical cord blood (UCB) [1-3]. Accordingly, a significant number of these cells (5-7  $\mu\text{m}$ ), which are smaller than red blood cells (RBCs), may be lost during gradient centrifugation as well as during routine volume depletion of UCB [1, 4]. Thus, there is a need to find a more efficient system of enriching VSEL concentration that minimizes the number of cells lost.

Laser light scattering has been applied as a noninvasive technique to study cells and tissues based on their optical properties [5-15]. The laser light scattering has been used to study nucleus and its enlargement of cells [11, 16-19] and Mie theory has been used to analyze the experimental results. However, Mie theory is often not sufficient because cells typically have non-spherical shapes, and other internal structures in addition to nucleus. It needs other

---

<sup>1</sup> Cell lineage is a developmental history of a differentiated cell as tracked back to the cell type which it arises. Cell type of some organisms may have invariant or variable cell lineages.

numerical solutions for Maxwell equations to better describe the laser light scattering from cells. Finite-difference time domain (FDTD) has been used for modeling results of experiment of laser light scattering from cells and providing information of cell size and organelle distributions [8-10, 20].

## 1.2. Structure of a cell

All cells have membrane, cytoplasm and genetic materials [21]. Eukaryotic and Prokaryotic cells are two broad categories of cells. Eukaryotic are more complex cells and have organelles (little organ) which includes nucleus, mitochondria and other parts. Prokaryotic cells do not have nucleus or membrane-enclosed organelles. They do have genetic material but it is not contained within nucleus. Organelles are the components of cell that each plays unique role. Different cell's membrane-enclosed organelles are shown in Figure 1.1.

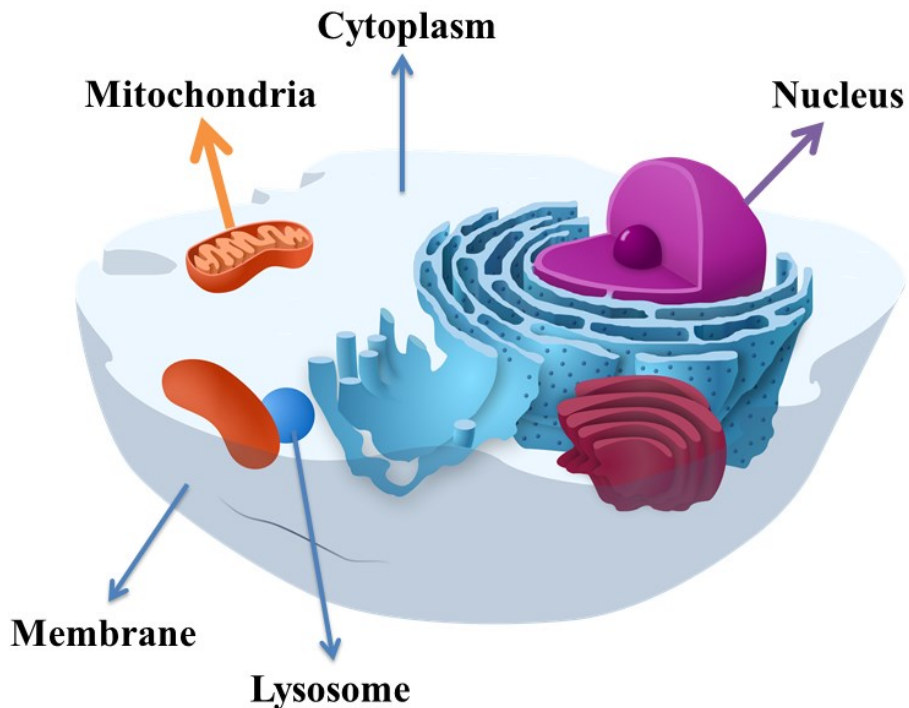


Figure 1.1: Illustration of biological cell showing internal parts and some organelles.

Nucleus, the control center of the cell, serves the function of information storage, retrieval and duplication of genetic information. Cytoplasm is a floating medium enclosed in the cell membrane letting parts to get connected and communicated. Lysosome is an animal cell organelle and they are garbage collectors and filled with enzymes that break down the cellular debris. The mitochondrion is the powerhouse organelle. Cells that need more energy have more mitochondria. Cells have other parts like cytoskeleton including microfilaments and microtubules which preserve cell's shape.

Among the different types of organelles, the nucleus and the mitochondria are widely studied for providing a better understanding of many diseases. Studies have found that cancerous cells have bigger nucleus size [11, 17, 22]. It has been reported that mitochondria's different distribution inside the cell is an evidence of cell health [8]. Additionally, mitochondria malfunction is the reason of many diseases such as Alzheimer's and Parkinson's [23].

**Table 1.1: Properties of internal components in an eukaryotic cell [24-27]**

<b>Cell organelle</b>	<b>Diameter (<math>\mu\text{m}</math>)</b>	<b>Refractive Index, n</b>	<b>% of cell by volume</b>
Cytoplasm	10-30	1.38	50-80
Nucleus	3-10	1.39	5-10
Mitochondria	0.3-0.7	1.42	5-15
Lysosome	0.2-0.5	1.3785	1-10*

\*Includes other remaining organelles

Physical and optical properties of internal components in an eukaryotic cell are presented in Table 1.1. Cytoplasm has the highest fractional volume among all components. A mitochondrion has the highest refractive index. A nucleus has a comparable fractional volume as the mitochondria but a slightly bigger size individually while has a slightly lower refractive index.

The rest of the components has a refractive index comparable to cytoplasm but a much smaller fractional volume and thus is expected to scatter less light when compared with the cytoplasm, nucleus and the mitochondria.

### **1.3.Stem cells**

A stem cell (SC) is a cell capable of renewing itself and differentiating into other cells [28]. There are many different types of SC classified according to their proliferative potential and ability to differentiate. SCs are very heterogeneous and there is a large degree of hierarchy within their pool. Totipotent SC is the earliest SC that develops an adult mammal and gives rise to cells of both placenta and embryo. As shown in Figure 1.2, totipotent SCs differentiate into pluripotent stem cells (PSCs) after the first division during embryonic development. PSCs can give rise to all three germ layers (ecto-, meso- and endoderm) as well differentiating into multipotent stem cells (MSCs) and tissue-specific stem cells (TSSCs). TSSCs are able to differentiate into only one type of cell tissue. TSSCs are important through the entire life of an individual that should be replaced every 48 hours (intestinal epithelium), 14 days (epidermis), 7 days (granulocytes) and 100-150 days (erythrocytes) [29, 30]. Due to SCs important role in everyday regeneration of several types of tissues, they are an attractive subject and object of interest for clinical use and modern pharmacology to improve the quality of life.

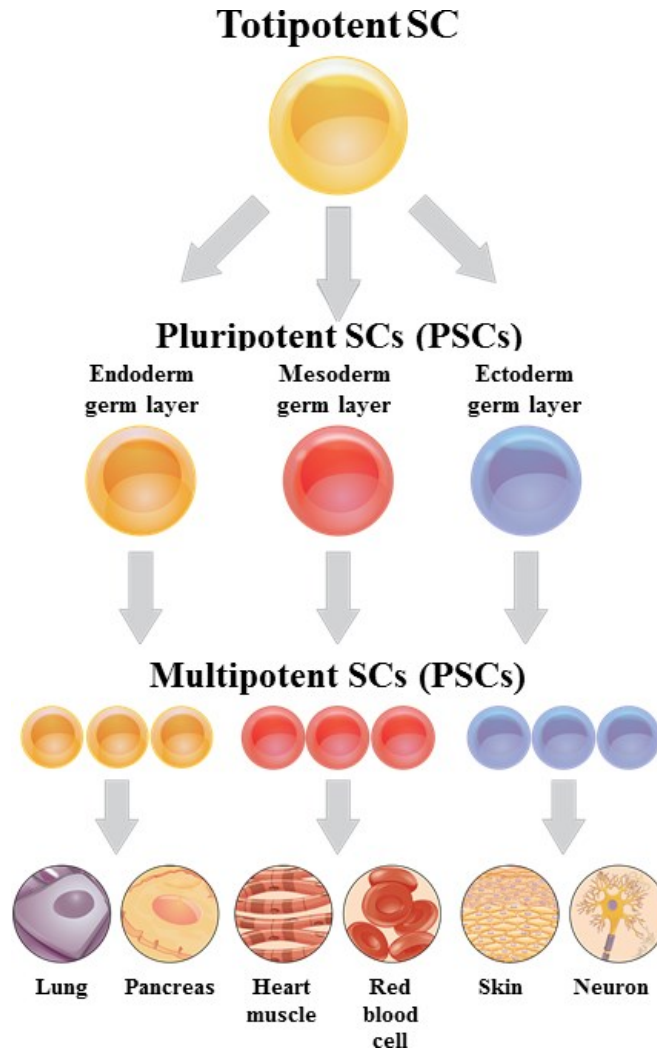


Figure 1.2: Human body stem cells hierarchy.

#### 1.4. Hematopoietic vs. non-hematopoietic stem cells

Umbilical cord contains three major blood vessels including one vein and two arteries harboring fetal blood named as umbilical cord blood (UCB) [31]. UCB is the main supplier of oxygen and nutrition elements required by developing fetus. Additionally, UCB removes metabolites and fetal waste products. UCB greatly enriched in immature cells including stem and progenitor cells (SPCs). SPCs are the only type of SCs that under certain physiological or experimental conditions are capable of giving rise into another type of cell with a more specialized function

including muscles, blood or different types of neuronal cell and other mature cells. SPCs available in UCB are divided into two main categories of hematopoietic and non-hematopoietic stem cells.

UCB contains an abundant population of hematopoietic stem cells (HSCs) [32]. Early stage HSCs are capable of constant repopulating and renewing whole hematopoietic and immunological system within the human lifespan. UCB has been reported as a source of primitive HSCs [33]. Currently, HSCs are characterized by certain hematopoietic antigens such as CD34 and CD133. However, CD34-negative ( $CD34^-$ ) HSCs is the main identifier for human primitive HSC compartment. A proposed model of the human hematopoietic hierarchy and ( $CD34^-$ ) HSCs and ( $CD34^+$ ) HSCs dependence is shown in Figure 1.3. As shown in this figure, very primitive ( $CD34^-$ ) HSCs are matured into ( $CD34^+$ ) HSCs. ( $CD34^+$ ) HSCs can give rise to various types of HPCs, as shown in the figure. In this thesis, a ( $CD34^-$ ) HSCs sample is used in the sample but the existence of ( $CD34^+$ ) HSCs inside the sample cannot be easily ruled out.

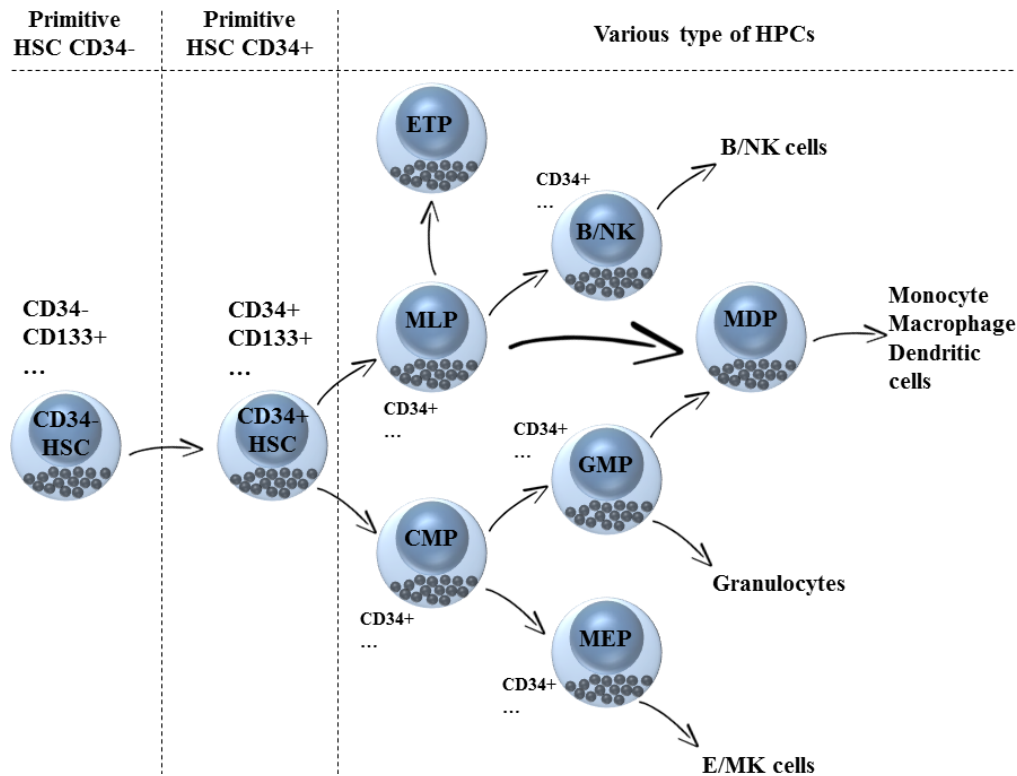


**Figure 1.3: Model of the human hematopoietic hierarchy. Very primitive  $CD34^-$  HSCs are able to produce primitive  $CD34^+$  HSCs. [34]**

Non-hematopoietic SPCs available in UCB consist of very small embryonic-like (VSEL) stem cells [1, 15, 35, 36], endothelial progenitor cells (EPCs) [37, 38], neural stem cells (NSCs) [39, 40], unrestricted somatic stem cells (USSCs) [41], mesenchymal stem cells (MSCs) [42, 43], and multipotent progenitor cells (MPCs) [44]. VSELs have embryonic characteristics that express typical PSCs marker (Oct-4, Nanog, and SSEA [45]). They have small size with high nuclear/cytoplasmic ratio. VSELs can differentiate into selected cell types derived from all three germ layers (ecto-, meso- and endoderm). VSEL SCs can differentiate into organ-specific cells. Currently, VSEL SCs are difficult to obtain in large number. In addition to their already low concentration in UCB, because of their small sizes, UCB-derived VSEL SCs could be easily lost at various steps of classical and standardized UCB preparation [1, 4]. Also as pointed out earlier

that the current technique for isolating VSEL SCs from UCB would require 6-12 labeling steps [1-3] as well as gradient centrifugation resulting in a significant loss in VSEL SCs. Thus, there is a need to find a more efficient way of enriching VSEL SCs' concentration.

### **1.5. Our approach and thesis's goals**

As described before, both HSCs and VSEL SCs have important roles and are significant SCs. These cells' populations vary for each type and category. Based on traditional fluorescent-activated cell sorting (FACS) technique, each cell line needs to be identified by a unique biomarker or a unique combination of biomarkers in order to enable its separation and sorting. UCB-derived VSEL SCs are rare and in a human-UCB (hUCB) sample there is less than 1 VSEL in 5000 total nucleated cells (TNC) [46]. Using FACS and centrifugation to extract VSELs led to considerable loss of ~60% [46] with six to twelve labels [1-3].

In this thesis, laser light scattering is used as a label-free technique for identification of HSC and VSEL. The study of 2D scattered light patterns from single cells will be discussed as a means to extract the cell's physical properties and morphological structure. The knowledge can be applied to identify and sort these cells.

Chapter 2 of this thesis will first provide a description about current traditional cell sorting techniques, follow with some remarks about laser light scattering from cells and end with introduction of theoretical models using Mie theory and Finite-difference time-domain (FDTD) technique.

Plastic beads were often used as a surrogate for cells to help improving the experimental setup and validating numerical modeling calculations. In chapter 3, experimental and numerical modeling results from spherical and non-spherical beads will be discussed.

The results of experimental and numerical modeling from laser light scattering of cells will be presented in chapter 4. Chapter 5 closes this thesis with conclusions and remarks for future work.

## 2. Background

### 2.1. Fluorescence-activated flow cytometry

Flow cytometry is a powerful technique for the analysis of the multiple parameters of individual cells in a heterogeneous population. Flow cytometers are used in many applications ranging from Immunophenotyping to Ploidy analysis, to cell counting and Green Fluorescent Protein (GFP) expression analysis. The flow cytometer performs this analysis by passing thousands of cells per second through a laser beam and its photodetectors capture the light that emits from each cell. The data gathered can be analyzed statistically by flow cytometry software to report cellular characteristics such as size distribution, complexity phenotype (morphology) and health status. The commonly used fluorescence-activated cell sorting (FACS) flow cytometry which includes cell sorting based data from scattered light intensities from cells and fluorescent emissions from bio-markers attached to cells. The main components of a FACS cytometer are: 1) the fluidics system, which moves sample cells to the interrogation point where they are irradiated by a laser beam, 2) the lasers, which are the light sources for inducing scattered light and fluorescence emissions, 3) the optics, which gather and direct the light, 4) the photodetectors, which convert the light signals into electrical signals and 5) the electronics and the peripheral computer system, which convert the electrical signals into digital data and perform the necessary analysis. The interrogation point is the heart of the system where the laser and the sample cells interact and the optics collects the resultant scattered light and fluorescence emissions. The cells are made to pass through the laser beam one at a time and most flow cytometers accomplish this by hydrodynamic focusing, as shown in Figure 2.1.

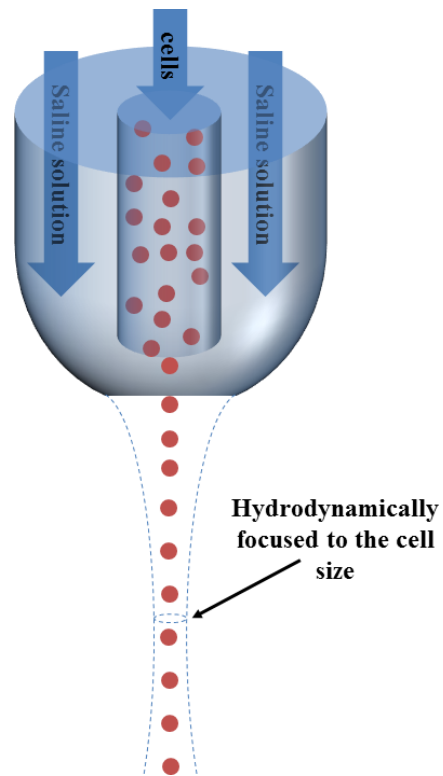


Figure 2.1: A schematic of hydrodynamic focusing process in a flow cytometer.

Hydrodynamic focusing is accomplished by injecting the sample stream containing the cells into a flowing stream of saline solution compressing the sample stream to roughly one cell diameter wide. Flow cytometers can accommodate cells that spanned roughly three orders of magnitude in size but they are commonly used for analyzing and sorting cells between 1 and 15 microns in diameter..

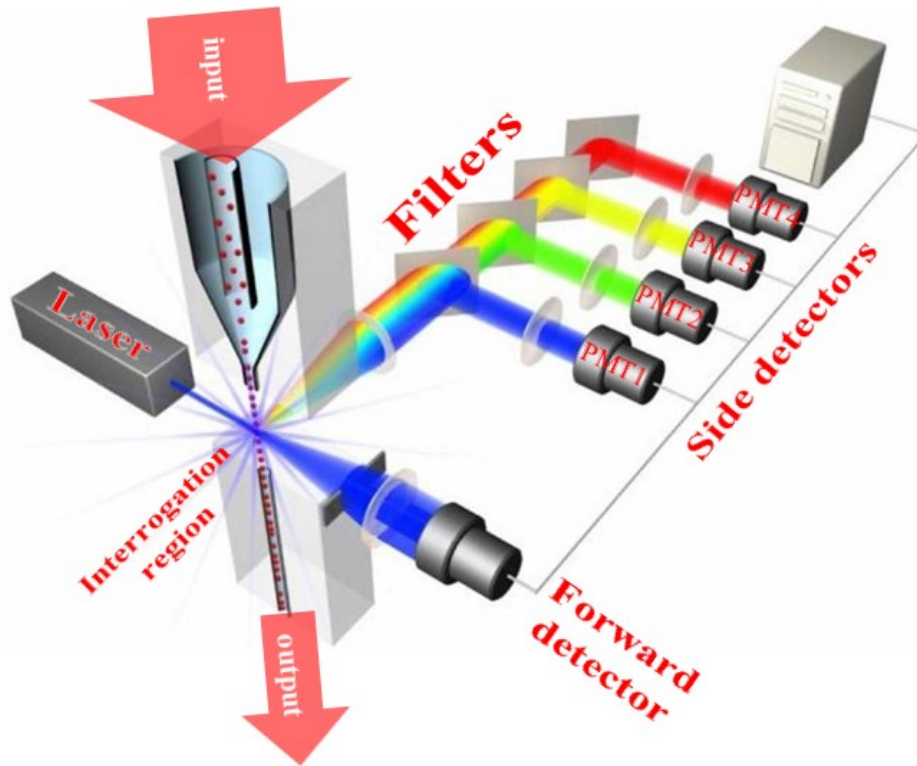
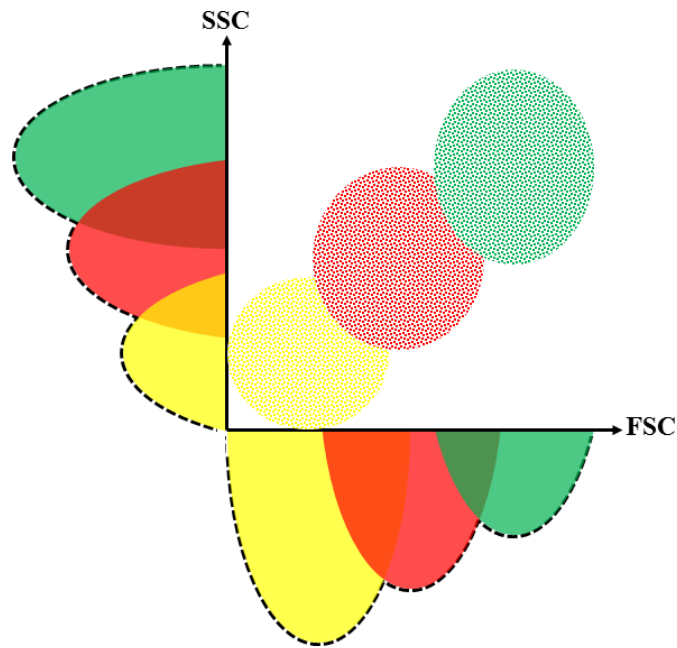


Figure 2.2: A schematic diagram of a FACS flow cytometer.

A schematic of flow cytometer is shown in Figure 2.2. As a cell passes through the laser, scattered light from the cell and fluorescent emissions from the biomarkers attached to the cell will radiate at all angles. Forward scattered light is the scattered light in an angle around zero degree respected to the forward laser direction. The intensity of the forward scattered light is roughly proportional to the size of the cell. In most cytometers, the blocking bar, called obscuration bar, is placed in front of the forward scatter detector to block any of the direct intense laser light. A histogram of forward scattered light intensities data is used as a graphical representation of the size distribution in the population.

Side scattered light at  $90^\circ$  to the laser beam direction is caused by the granularity and structural complexity inside the cell. This side scattered light is collected by a lens and is directed to a

photodetector (PMT1 in Figure 2.2) which often is a photomultiplier detector. The signals collected can be plotted on one-dimensional histograms like the graph in forward scatter (FSC).



**Figure 2.3: 2D histogram analysis of FACS. What it appears to be a single population in FSC or SSC axis, can be a combination of different cell type population.**

In reality, what appears to be a single population in forward scatter histogram can be multiple populations that can only be discerned by looking at the data in the 2nd dimension, Figure 2.3. This is done through the use of two dimensional dot or scatter plots. The peaks from forward and side scatter histograms correlate dots in a scatter plot

Multi-parametric analysis is a real advantage of the flow cytometry. Information about sample cell population and size distributions, and granularity differences of each cell category in the sample can be extracted from 2D histogram. Another parameter that can provide information about the cell's structure and functions is fluorescence.

Fluorescence is the term used to describe the excitation of fluorophore to a higher energy level followed by the return of that fluorophore to its ground state with the emission of the light. The

energy in the emitted light is dependent on the energy level to which the fluorophore is excited and that light has specific wavelength. This property is commonly used in cell biology to study cellular characteristics. In flow cytometry, the fluorophore containing antibodies or fluorescent biomarkers are added to the cell sample, as shown in Figure 2.4. The antibody then binds to the specific molecules/proteins on the cell surface or inside the cell. When the laser light irradiates the fluorophore, a fluorescent signal is emitted and detected by the photodetectors in flow cytometer.

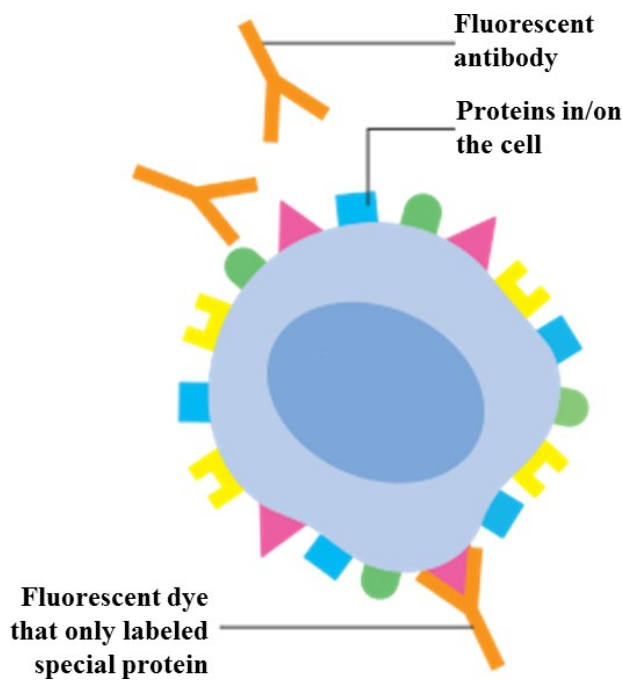


**Figure 2.4:** This schematic depicts the process of attaching fluorescent antibody to the target protein in/on the cell.

The multi-wavelength fluorescent light travel along the same path as the side scattered light is directed by mirrors, spectrally resolved by optical filters and is then measured by several photodetectors (PMT 2-4).

## **2.2.Laser light scattering studies of single cell**

Laser light scattering data can be used to obtain information about internal organelles in cells. An understanding of the physics of light scattering from biological cells is important to a number of non-invasive optical medical diagnostic technique like optical coherence tomography (OCT) [15], elastic scattering spectroscopy (ESS) [12, 13], and photon migration [14]. OCT uses backscattering infrared light from cells to construct a two-dimensional map of internal architectural morphology and cellular structures in the tissue [15]. ESS measures elastic-scattered light in a manner that is sensitive to both scattering and absorption properties over the range of wavelength [13]. Photon migration technique measures the optical absorption and reduced scattering coefficients of a modulated incident light after it propagates in the medium [14].

Cells have different sizes, shapes, and distribution of internal structures made of different materials. Different materials have different optical properties like refractive index. Changes on cell's optical and physical properties causing light to scatter differently resulting in variations of the amplitude of scattered light in different directions. The effects of laser light scattering due to cell's internal small structure distribution's changes and cell's size differences has been studied [8-10, 16, 22, 47-49]. It was found that cell's small internal structures such as mitochondria affect the angular distribution of scattered light, and variations on cell's sizes leads to scattered light amplitude differences [8, 9, 18, 47]. It was experimentally studied that single airborne particles of different shapes and geometries produces 2D scattered light patterns other than vertical fringes [50]. The study of geometry changes effects on 2D light scattering patterns in forward and

backward directions were also carried out for particles with different shapes of homogeneous and inhomogeneous spheres to deformed spheres (i.e. spheroid) and complex aggregates [51].

In laser scattering studies of cells, a low power of a few mW, coherent and continuous wave laser light is typically used. Low power is used in order not to damage the cell. The scattered light from the scatterer, as a function of angle with respect to the laser beam direction, carries information in regard to the scatterer's optical and physical properties. Forward scattered light in the small angular range ( $\theta < 2^\circ$ ) respect to the direction of incident light [48, 52] is related to cell's size and contains information about refractive index [48]. Forward scattered light at larger angles of  $5^\circ < \theta < 30^\circ$  is highly dependent on nucleus of the cell and nucleus/whole cell volume ratio [48]. Internal small organelles such as mitochondria contributing to light scattering at larger angles e.g. side direction ( $\theta = 90^\circ$ ). The backscatter region ( $160^\circ < \theta < 180^\circ$ ) is mainly affected by cell membrane. Figure 2.5 summaries the discussed scattering regions and their information.

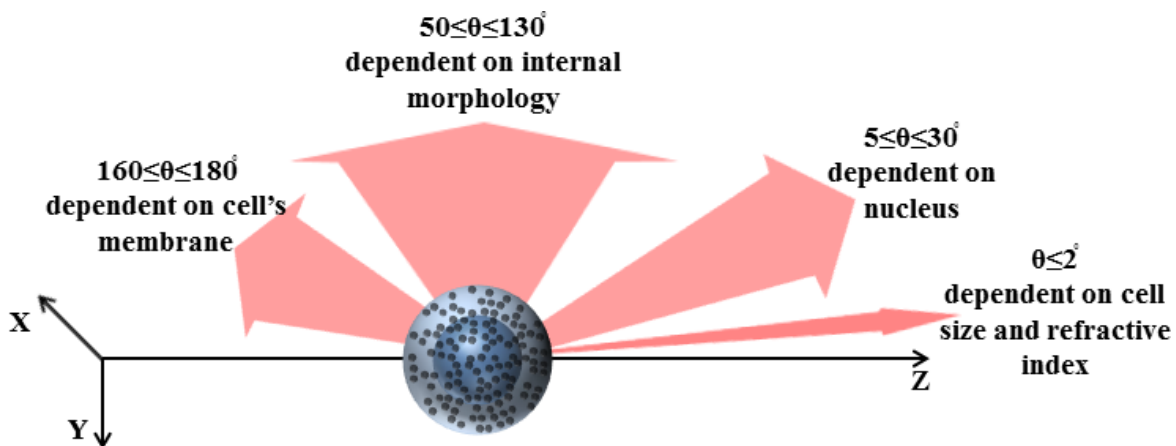


Figure 2.5: Information contained in angular light scattering.

Traditional cytometry technique is based on the ratio of forward scattered light intensity to side scattered intensity for narrow ranges of viewing angles. Widen the viewing angles will provide

us with improved information about the cells. The limitation can be overcome by using Charge-Coupled Device (CCD) to capture 2D scattered pattern.

When light wave travels through a cell made of different internal structures, due to changes in boundary conditions and refractive indices, the radiated field in all directions produces the scattered wave. Solving Maxwell's equations using analytical or numerical approaches provide solution to the light scattering problems. To solve the Maxwell's equations, a cell with internal structures can be modeled as several dielectric objects with different sizes, shapes and optical properties.

Mie theory is an exact analytical solution for light scattering problems involving a homogeneous spherical object interacts with a planar light wave [53, 54]. Mie theory is useful for modeling light scattering of spherical latex beads. Latex beads are commonly used as a surrogate for cells in laser light scattering studies. For more complex dielectric objects such as cells, numerical solutions are required. In this project, finite-difference time-domain (FDTD) method has been used to obtain exact numerical solutions of light scattering of cells.

A FDTD-based code, AETHER, has been developed in our group and can perform simulations of light scattering from cells with arbitrary shape and inner structure configurations. Mie theory is used to verify results generated from the AETHER code in simple cases involving single homogeneous dielectric spheres.

### **2.3.Mie scattering theory**

Mie theory is a solution for the Maxwell's equations in the special situation where the incident plane wave interacts with a homogenous dielectric sphere. In general, the amount of scattering light depends on the direction from the electromagnetic (EM) wave. The scattering light intensity

is the strongest in the forward directions and becomes weaker in other directions. Starting from Maxwell's equations, the time-harmonic plane waves satisfy the source-free below equations:

$$\nabla \cdot \vec{E} = 0 \quad 2.1$$

$$\nabla \cdot \vec{H} = 0 \quad 2.2$$

$$\nabla \times \vec{E} = j\omega\mu\vec{H} \quad 2.3$$

$$\nabla \times \vec{H} = -j\omega\varepsilon\vec{E} \quad 2.4$$

Where  $\omega$  is the angular frequency,  $\mu$  is the permeability, and  $\varepsilon$  is the permittivity. There are the incident field as donated by  $(\vec{E}_i, \vec{H}_i)$ , the scattered field as donated by  $(\vec{E}_s, \vec{H}_s)$  and the field inside the scatterer as donated by  $(\vec{E}_1, \vec{H}_1)$ . The incident plane wave traveling in +z direction is defined by  $\vec{E}_i = \vec{E}_0 e^{i(\vec{k} \cdot \vec{z} - \omega t)}$  and  $\vec{H}_i = \vec{H}_0 e^{i(\vec{k} \cdot \vec{z} - \omega t)}$  where  $k$  is the wave propagation vector ( $k^2 = \omega^2 \varepsilon \mu$ ).

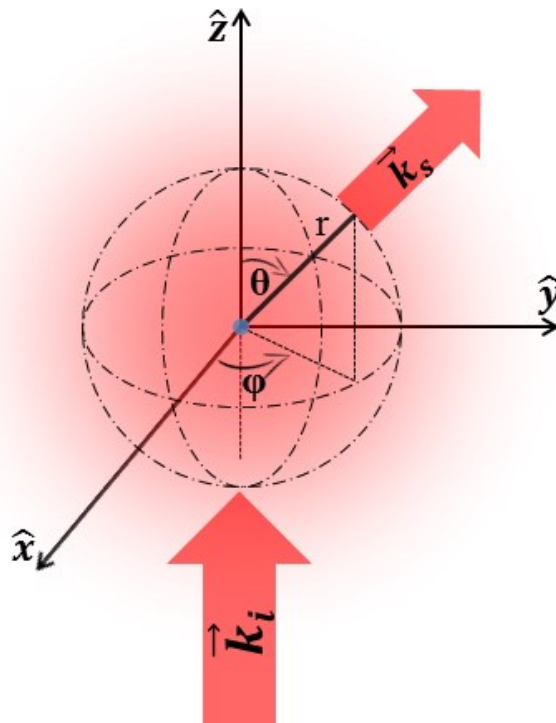


**Figure 2.6: Light scattering geometry for a single scatterer is shown in this figure. The incident wave propagates along the +z direction, the scattered wave has a polar angle “ $\theta$ ” and an azimuth angle “ $\varphi$ ” as shown in the figure. (  $r, \theta, \varphi$ ) defines the spherical coordinates. The spherical scatterer with a radius “ $r$ ” is centered at the origin.**

The light scattering schematic is shown in Figure 2.6. Scattered fluxes in terms of different polarizations (perpendicular denoted by 1, parallel denoted by 2 and unpolarized) can be defined as below where  $I_i$  is the incident flux:

$$I_{s,1} = \frac{i_1}{k^2 r^2} I_i \quad 2.5$$

$$I_{s,2} = \frac{i_2}{k^2 r^2} I_i \quad 2.6$$

$$I_s = \frac{i_1 + i_2}{k^2 r^2} I_i \quad 2.7$$

The scattered polarized intensities are defined by  $i_1 = |S_1|^2$  and  $i_2 = |S_2|^2$  where  $S_1$  and  $S_2$  are the elements of scattering amplitude matrix which correlates the incident and scattered fields and finding the analytical solution for them is the objective of analysis.

Above formulas, equations 2.1-2.4, should satisfy time-harmonic wave equations as below:

$$\nabla^2 \vec{E} + k^2 \vec{E} = 0 \quad 2.8$$

$$\nabla^2 \vec{H} + k^2 \vec{H} = 0 \quad 2.9$$

With use of variables' separations of solutions for wave equations in spherical polar coordinates and four spherical Bessel functions, the vector spherical harmonics can be found to expand the plane wave. The scalar wave equation in spherical polar coordinates can be writes as:

$$\frac{1}{r^2} \frac{\partial}{\partial r} \left( r^2 \frac{\partial \psi}{\partial r} \right) + \frac{1}{r^2 \sin \theta} \left( \sin \theta \frac{\partial \psi}{\partial \theta} \right) + \frac{1}{r^2 \sin \theta} \frac{\partial^2 \psi}{\partial \varphi^2} + k^2 \psi = 0 \quad 2.10$$

Solutions for 2.25 can be constructed by separation of variables,  $\psi(r, \theta, \varphi) = R(r)\Theta(\theta)\Phi(\varphi)$ , as follows:

$$\psi_{emn} = \cos(m\varphi) P_n^m(\cos \theta) z_n(kr) \quad 2.11$$

$$\psi_{omn} = \sin(m\varphi) P_n^m(\cos \theta) z_n(kr) \quad 2.12$$

Where subscripts  $e$  and  $o$  donate even and odd numbers,  $m=0,1,2,\dots$ ,  $n=m,m+1,\dots$ .  $P_n^m(\cos \theta)$  is the associated Legendre function as solution to  $\Theta(\theta)$ ,  $\sin(m\varphi)$  and  $\cos(m\varphi)$  are azimuth function as solutions for  $\Phi(\varphi)$  and  $z_n(kr)$  is any of the four spherical Bessel functions as solutions for  $R(r)$  as below:

$$j_n(\rho) = \sqrt{\frac{\pi}{2\rho}} J_{n+\frac{1}{2}}(\rho) \quad 2.13$$

$$n_n(\rho) = \sqrt{\frac{\pi}{2\rho}} N_{n+\frac{1}{2}}(\rho) \quad 2.14$$

$$h_n^{(1)} = j_n(\rho) + in_n(\rho) \quad 2.15$$

$$h_n^{(2)} = j_n(\rho) - in_n(\rho) \quad 2.16$$

Where  $\rho = kr$ . Two vector functions in spherical polar coordinates are defined as  $\vec{M} = \nabla \times (\vec{r}\psi)$  and  $\vec{N} = \frac{\nabla \times \vec{M}}{k}$  where  $\vec{M}$  and  $\vec{N}$  satisfy the wave equations (2.8 and 2.9). These two can be given as below based on 2.11 and 2.12,

$$\vec{M}_{emn} = \nabla \times (\vec{r}\psi_{emn}), \vec{M}_{omn} = \nabla \times (\vec{r}\psi_{omn}) \quad 2.17$$

$$\vec{N}_{emn} = \frac{\nabla \times \vec{M}_{emn}}{k}, \vec{N}_{omn} = \frac{\nabla \times \vec{M}_{omn}}{k} \quad 2.18$$

A plane wave can be expanded in vector spherical harmonics as

$$\vec{E}_i = E_0 \sum_{n=1}^{\infty} i^n \frac{2n+1}{n(n+1)} (\vec{M}_{o1n}^{(1)} - i\vec{N}_{o1n}^{(1)}) \quad 2.19$$

Where (1) denotes 1<sup>st</sup> Bessel function (2.13). The curl of 2.19 is the corresponding incident magnetic field as below:

$$\vec{H}_i = \frac{-k}{\omega\mu} E_0 \sum_{n=1}^{\infty} i^n \frac{2n+1}{n(n+1)} (\vec{M}_{o1n}^{(1)} - i\vec{N}_{o1n}^{(1)}) \quad 2.20$$

The internal field expansion can be given as,

$$\vec{E}_1 = E_0 \sum_{n=1}^{\infty} i^n \frac{2n+1}{n(n+1)} (c_n \vec{M}_{o1n}^{(1)} - id_n \vec{N}_{o1n}^{(1)}) \quad 2.21$$

$$\vec{H}_1 = \frac{-k_1}{\omega\mu_1} E_0 \sum_{n=1}^{\infty} i^n \frac{2n+1}{n(n+1)} (d_n \vec{M}_{o1n}^{(1)} - ic_n \vec{N}_{o1n}^{(1)}) \quad 2.22$$

And scattered field expansion is as follows:

$$\vec{E}_s = E_0 \sum_{n=1}^{\infty} i^n \frac{2n+1}{n(n+1)} (ia_n \vec{N}_{e1n}^{(3)} - ib_n \vec{M}_{o1n}^{(3)}) \quad 2.23$$

$$\vec{H}_s = \frac{-k}{\omega\mu} E_0 \sum_{n=1}^{\infty} i^n \frac{2n+1}{n(n+1)} (ib_n \vec{N}_{e1n}^{(3)} - a_n \vec{M}_{o1n}^{(3)}) \quad 2.24$$

Where (3) denotes 3<sup>rd</sup> Bessel function (2.15). Four main scattering coefficients,  $a_n, b_n, c_n$  and  $d_n$  generated from these steps can be found by solving boundary conditions with use of below formula:

$$E_{i\theta} + E_{s\theta} = E_{1\theta}, E_{i\varphi} + E_{s\varphi} = E_{1\varphi} \quad 2.25$$

$$H_{i\theta} + H_{s\theta} = H_{1\theta}, H_{i\varphi} + H_{s\varphi} = H_{1\varphi} \quad 2.26$$

$\theta$  and  $\varphi$  are polar and azimuth angles in spherical coordinates as shown in Figure 2.6. Scattering and internal coefficients are expressed as below:

$$a_n = \frac{\mu m^2 j_n(mx) [x j_n^{(1)}(x)]' - \mu_1 j_n(x) [m x j_n(mx)]'}{\mu m^2 j_n(mx) [x h_n^{(1)}(x)]' - \mu_1 h_n^{(1)}(x) [m x j_n(mx)]'} \quad 2.27$$

$$b_n = \frac{\mu_1 j_n(mx) [x j_n(x)]' - \mu j_n(x) [m x j_n(mx)]'}{\mu_1 j_n(mx) [x h_n^{(1)}(x)]' - \mu h_n^{(1)}(x) [m x j_n(mx)]'} \quad 2.28$$

$$c_n = \frac{\mu_1 j_n(x) [x h_n^{(1)}(x)]' - \mu_1 h_n^{(1)}(x) [x j_n(x)]'}{\mu_1 j_n(mx) [x h_n^{(1)}(x)]' - \mu h_n^{(1)}(x) [m x j_n(mx)]'} \quad 2.29$$

$$d_n = \frac{\mu_1 m j_n(x) [x h_n^{(1)}(x)]' - \mu_1 m h_n^{(1)}(x) [x j_n(x)]'}{\mu m^2 j_n(mx) [x h_n^{(1)}(x)]' - \mu_1 h_n^{(1)}(x) [m x j_n(mx)]'} \quad 2.30$$

Where  $x$  is the size parameter ( $x = \frac{2\pi na}{\lambda}$ ) and  $m$  is the relative refractive index ( $m = \frac{n_1}{n}$  where  $n_1$  and  $n$  are scatterer and medium refractive indices, respectively). The incident wavelength in vacuum is  $\lambda$ . The scattering matrix elements,  $S_1$  and  $S_2$ , are calculated as below:

$$S_1 = \sum_{n=1}^{\infty} \frac{2n+1}{n(n+1)} (a_n \pi_n + b_n \tau_n) \quad 2.31$$

$$S_2 = \sum_{n=1}^{\infty} \frac{2n+1}{n(n+1)} (a_n \tau_n + b_n \pi_n) \quad 2.32$$

Where  $a_n$  and  $b_n$  are the scattering coefficients and defined as:

$$a_n = \frac{m \psi_n(mx) \psi_n'(x) - \psi_n(x) \psi_n'(mx)}{m \psi_n(mx) \xi_n'(x) - \xi_n(x) \psi_n'(mx)} \quad 2.33$$

$$b_n = \frac{\psi_n(mx) \psi_n'(x) - m \psi_n(x) \psi_n'(mx)}{\psi_n(mx) \xi_n'(x) - m \xi_n(x) \psi_n'(mx)} \quad 2.34$$

$\psi(\rho) = \rho j_n(\rho)$  and  $\xi(\rho) = \rho h_n^{(1)}(\rho)$  are Riccati-Bessel functions where  $j_n$  is the  $n$ th-order Bessel function of first kind, and  $h_n^{(1)}$  is the  $n$ th-order Henkel function for the first time.  $\pi_n = \frac{P_n^1(\cos \theta)}{\sin \theta}$  and  $\tau_n = \frac{dP_n^1(\cos \theta)}{d\theta}$  are the angle dependent functions.

These Mie derivations are paraphrased from Su's thesis [55] based on Bohren and Huffman [54] and Grandy [53]. Full formulation of this theory can be found in Hulst [56] and Bohren and Huffman [54] textbooks. This theory has been implemented as Mie scattering algorithm in variety of computer programming languages such as FORTRAN, C, Matlab, Python and IDL, available as public codes. MiePlot [57] program was originally designed to provide a simple interface to the classic BHMIE algorithm [54] for Mie scattering from a sphere - as published by Bohren and Huffmann [54]. MiePlot version 4.5 has been used as a Mie scattering calculator in this thesis and in-depth information about this program can be found in provided program website in Reference [57].

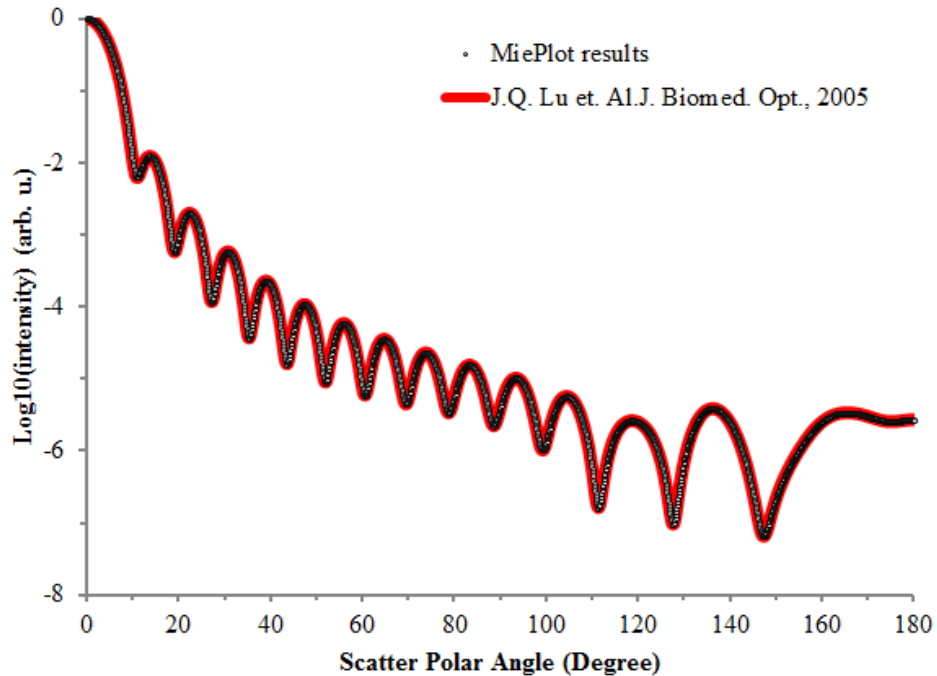


Figure 2.7: Validation of MiePlot program results in full angular range.

To validate the results, the published results were compared with generated results from MiePlot program. Based on Lu *et al.* [58] article, a  $2.655 \mu\text{m}$  radius homogeneous spherical scatterer with refractive index of 1.402 in a medium with refractive index of 1.35 was simulated. The unpolarized incident light has a wavelength of  $1 \mu\text{m}$ . The generated Mieplot results were normalized by the intensity at polar angle  $\theta = 0^\circ$ . The logarithmic values are then plotted. Figure 2.7 shows the comparison results indicating good agreement between MiePlot results and those from previously published simulations.

Mie theory approximated results are limited to the homogeneous symmetric scatterer as Mie theory involves strict boundary conditions which are not suitable for models of cells with non-uniform shapes and complex refractive indices structure configurations. FDTD method is needed for simulating heterogeneous models with complex inner material structures.

## 2.4.FDTD method

In this project the FDTD method-based AETHER code has been used to solve the Maxwell's equations and calculate the 2D scattered light patterns in the far field. A brief description of some of the basics of the AETHER code will be presented next. Information of compiling and running the codes using the Westgrid clusters can be found in Appendix A.1.

### 2.4.1. Yee's algorithm

In general, the circulating  $\vec{E}$  field induces a change in  $\vec{B}$  field. The  $\vec{B}$  field induces  $\vec{H}$  field in proportion to the permeability. A circulating  $\vec{H}$  field induces a change in the  $\vec{D}$  field at the center of circulation and a  $\vec{D}$  field induces  $\vec{E}$  field in proportion to the permittivity. Yee's FDTD is the algorithm that follows these sequences to solve for both the electric and magnetic field in time and in space. The slope value is assumed to be at the mid-point of the two grid points. The equations used in FDTD loop is calculated as below [20].

$$\nabla \times \vec{E}|_t = -\mu \frac{\vec{H}|_{t+\frac{\Delta t}{2}} - \vec{H}|_{t-\frac{\Delta t}{2}}}{\Delta t} \rightarrow \vec{H}|_{t+\frac{\Delta t}{2}} = \vec{H}|_{t-\frac{\Delta t}{2}} - \frac{\Delta t}{\mu} (\nabla \times \vec{E}|_t) \quad 2.35$$

$$\nabla \times \vec{H}|_{t+\frac{\Delta t}{2}} = \varepsilon \frac{\vec{E}|_{t+\frac{\Delta t}{2}} - \vec{E}|_t}{\Delta t} \rightarrow \vec{E}|_{t+\frac{\Delta t}{2}} = \vec{E}|_t - \frac{\Delta t}{\varepsilon} (\nabla \times \vec{H}|_{t+\frac{\Delta t}{2}}) \quad 2.36$$

Where the  $\Delta t$  is the time step and the subscript  $t \pm \Delta t/2$  define the electric and magnetic field values at the mid-point of a time step. Based on Maxwell's source-free curl equations 2.37 and 2.38, in 3D rectangular coordinate system as shown in Figure 2.8, The electric and magnetic components are centered in three-dimensional space so that every electric component is surrounded by four circulating magnetic components, and every magnetic component is surrounded by four circulating electric components.

$$\frac{\partial \vec{H}}{\partial t} = -\frac{1}{\mu} \nabla \times \vec{E} \quad 2.37$$

$$\frac{\partial \vec{E}}{\partial t} = -\frac{1}{\varepsilon} \nabla \times \vec{H} \quad 2.38$$

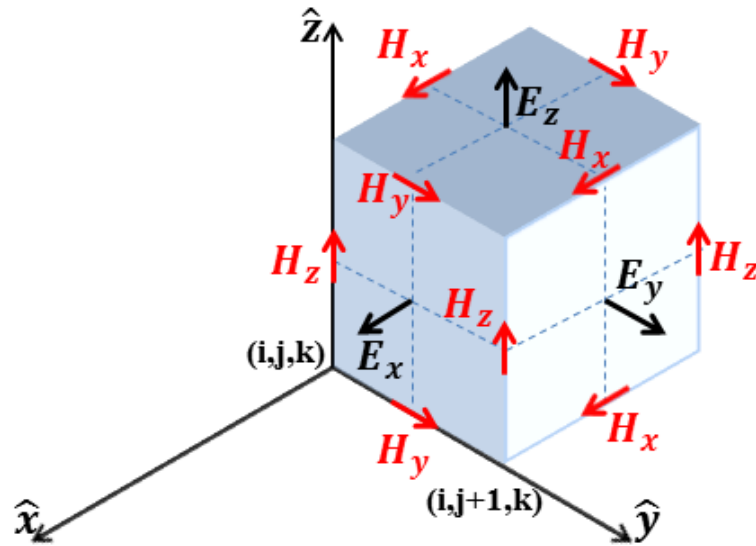


Figure 2.8: Electric and magnetic field vector components in the Yee's space lattice are shown in this figure.

A numerical scheme is needed to calculate derivatives based field values at discrete grid points for solving the Maxwell's Equations. Central finite-difference approximations are used to provide the slope value of a function by dividing the difference of the values of the function at two neighboring grid points by the step size.

Two curl equations in 2.37 and 2.38 can be written as,

$$\frac{\partial H_x}{\partial t} = \frac{1}{\mu} \left( \frac{\partial E_y}{\partial z} - \frac{\partial E_z}{\partial y} \right) \quad 2.39$$

$$\frac{\partial H_y}{\partial t} = \frac{1}{\mu} \left( \frac{\partial E_x}{\partial z} - \frac{\partial E_z}{\partial x} \right) \quad 2.40$$

$$\frac{\partial H_z}{\partial t} = \frac{1}{\mu} \left( \frac{\partial E_x}{\partial y} - \frac{\partial E_y}{\partial x} \right) \quad 2.41$$

$$\frac{\partial E_x}{\partial t} = \frac{1}{\mu} \left( \frac{\partial H_y}{\partial z} - \frac{\partial H_z}{\partial y} \right) \quad 2.42$$

$$\frac{\partial E_y}{\partial t} = \frac{1}{\mu} \left( \frac{\partial H_x}{\partial x} - \frac{\partial H_x}{\partial z} \right) \quad 2.43$$

$$\frac{\partial E_z}{\partial t} = \frac{1}{\mu} \left( \frac{\partial H_x}{\partial y} - \frac{\partial H_y}{\partial x} \right) \quad 2.44$$

Yee defines a uniform, rectangular lattice as shown in Figure 2.8 as  $(i, j, k) = (i\Delta x, j\Delta y, k\Delta z)$  where  $\Delta x$ ,  $\Delta y$  and  $\Delta z$  are grid spacing in x, y and z directions respectively. Based on Yee's discretization scheme, any function such as  $u_{i,j,k}^n = u(i\Delta x, j\Delta y, k\Delta z, n\Delta t)$ , where  $\Delta t$  is the time spacing and n is the time index, have first partial space derivative in the x direction at a fixed time  $t_n = n\Delta t$  as follows:

$$\frac{\partial u_{i,j,k}^n}{\partial x} = \frac{u_{i+1/2,j,k}^n - u_{i-1/2,j,k}^n}{\Delta x} \quad 2.45$$

The first partial time derivative of u at fixed space point (i,j,k) is,

$$\frac{\partial u_{i,j,k}^n}{\partial t} = \frac{u_{i,j,k}^{n+1/2} - u_{i,j,k}^{n-1/2}}{\Delta t} \quad 2.46$$

By substituting first partial space and time derivative into equations 2.39-2.44 and using central finite-difference approximations, the six coupled explicit second-order accurate finite difference equations, 2.47-2.52, are obtained.

$$H_x|_{i,j,k}^{n+\frac{1}{2}} = H_x|_{i,j,k}^{n-\frac{1}{2}} + \frac{\Delta t}{\mu_{i,j,k}} \left( \frac{E_y|_{i,j,k+\frac{1}{2}}^n - E_y|_{i,j,k-\frac{1}{2}}^n}{\Delta z} - \frac{E_z|_{i,j,k+\frac{1}{2}}^n - E_z|_{i,j,k-\frac{1}{2}}^n}{\Delta y} \right) \quad 2.47$$

$$H_y|_{i,j,k}^{n+\frac{1}{2}} = H_y|_{i,j,k}^{n-\frac{1}{2}} + \frac{\Delta t}{\mu_{i,j,k}} \left( \frac{E_z|_{i+\frac{1}{2},j,k}^n - E_z|_{i-\frac{1}{2},j,k}^n}{\Delta x} - \frac{E_x|_{i,j,k+\frac{1}{2}}^n - E_x|_{i,j,k-\frac{1}{2}}^n}{\Delta z} \right) \quad 2.48$$

$$H_z|_{i,j,k}^{n+\frac{1}{2}} = H_z|_{i,j,k}^{n-\frac{1}{2}} + \frac{\Delta t}{\mu_{i,j,k}} \left( \frac{E_x|_{i,j+\frac{1}{2},k}^n - E_x|_{i,j-\frac{1}{2},k}^n}{\Delta y} - \frac{E_y|_{i+\frac{1}{2},j,k}^n - E_y|_{i-\frac{1}{2},j,k}^n}{\Delta x} \right) \quad 2.49$$

$$E_x|_{i,j,k}^{n+1} = E_x|_{i,j,k}^n + \frac{\Delta t}{\varepsilon_{i,j,k}} \left( \frac{H_z|_{i,j+\frac{1}{2},k}^{n+\frac{1}{2}} - H_z|_{i,j-\frac{1}{2},k}^{n+\frac{1}{2}}}{\Delta y} - \frac{H_y|_{i,j,k+\frac{1}{2}}^{n+\frac{1}{2}} - H_y|_{i,j,k-\frac{1}{2}}^{n+\frac{1}{2}}}{\Delta z} \right) \quad 2.50$$

$$E_y|_{i,j,k}^{n+1} = E_y|_{i,j,k}^n + \frac{\Delta t}{\varepsilon_{i,j,k}} \left( \frac{H_x|_{i,j,k+\frac{1}{2}}^{n+\frac{1}{2}} - H_x|_{i,j,k-\frac{1}{2}}^{n+\frac{1}{2}}}{\Delta z} - \frac{H_z|_{i+\frac{1}{2},j,k}^{n+\frac{1}{2}} - H_z|_{i-\frac{1}{2},j,k}^{n+\frac{1}{2}}}{\Delta x} \right) \quad 2.51$$

$$E_z|_{i,j,k}^{n+1} = E_z|_{i,j,k}^n + \frac{\Delta t}{\varepsilon_{i,j,k}} \left( \frac{H_y|_{i+\frac{1}{2},j,k}^{n+\frac{1}{2}} - H_y|_{i-\frac{1}{2},j,k}^{n+\frac{1}{2}}}{\Delta x} - \frac{H_x|_{i,j+\frac{1}{2},k}^{n+\frac{1}{2}} - H_x|_{i,j-\frac{1}{2},k}^{n+\frac{1}{2}}}{\Delta y} \right) \quad 2.52$$

Where  $\varepsilon_{i,j,k}$  and  $\mu_{i,j,k}$  are values of permittivity and permeability of point (i,j,k), respectively.  $\Delta t$  is the time step. Subscripts i, j and k represent the grid number in X, Y, and Z directions.  $\Delta x$ ,  $\Delta y$  and  $\Delta z$  are grid spacing in X, Y, and Z directions respectively.

#### 2.4.2. Grid consideration

In order to minimize the computational error during calculations, the stability conditions should be considered. The Courant condition for equations 2.47-2.52 is given by [49]:

$$\Delta t_c \leq \frac{1}{c \sqrt{\frac{1}{(\Delta x)^2} + \frac{1}{(\Delta y)^2} + \frac{1}{(\Delta z)^2}}} \quad 2.53$$

Where, c is the speed of light. This equation suggests that the spatial grid spacing must be less than  $\lambda/10$  to diverge the error and stabilize the calculation process ( $\lambda$  is the wavelength of

incident light). Liao boundary conditions applied to minimize the reflection of signal from the boundaries.

### 2.4.3. Near-to-Far field transformation (NTF)

In order to calculate the scattering field, the total-field/scattering-field (TF/SF) technique is used [20]. As shown in Figure 2.9, the total field is calculated inside the TF/SF interface. Scattered field is only calculated outside of TF/SF interface. Therefore, using incident light values and calculated total field values, we can extract the scattered field domain values.

$$\vec{E}_{total} = \vec{E}_{incident} + \vec{E}_{scattering}, \vec{H}_{total} = \vec{H}_{incident} + \vec{H}_{scattering} \quad 2.54$$

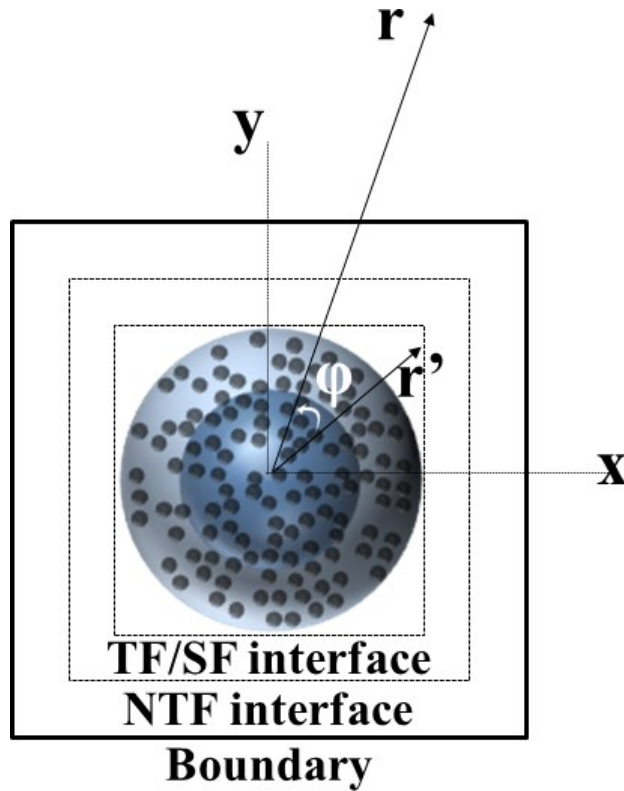


Figure 2.9: The geometry of the FDTD computational domain.

FDTD has been used to calculate electric and magnetic fields close to the scatterer. Using near-to-far field transformation we can measure the scattered field pattern far from the scatterer. Liu et

al. used the equivalent electric/magnetic currents technique to calculate the scattered field at a distance [20]. The radiation sources inside the NTF field interface as shown in Figure 2.9 can be virtually represented by electric currents and magnetic currents as below:

$$\vec{J}_s(\vec{r}') = \hat{n} \times \vec{H}, \vec{M}_s(\vec{r}') = -\hat{n} \times \vec{E} \quad 2.55$$

Where  $\vec{J}_s(\vec{r}')$  is virtual electric current,  $\vec{M}_s(\vec{r}')$  is magnetic current,  $\vec{r}'$  is a point on the surface, and  $\hat{n}$  is normal to the surface. The far field electric and magnetic field components are given by,

$$E_r=0 \quad 2.56$$

$$E_\theta = -\frac{jk \exp(-jkr)}{4\pi r} (L_\phi + \sqrt{\frac{\mu}{\epsilon}} N_\theta) \quad 2.57$$

$$E_\phi = -\frac{jk \exp(-jkr)}{4\pi r} (L_\theta + \sqrt{\frac{\mu}{\epsilon}} N_\phi) \quad 2.58$$

$$H_r=0 \quad 2.59$$

$$H_\theta = -\frac{jk \exp(-jkr)}{4\pi r} (N_\phi + \sqrt{\frac{\mu}{\epsilon}} L_\theta) \quad 2.60$$

$$H_\phi = -\frac{jk \exp(-jkr)}{4\pi r} (N_\theta + \sqrt{\frac{\mu}{\epsilon}} L_\phi) \quad 2.61$$

Where  $k$  is wave number and  $r$  is a point in the far field. Vectors potentials  $\vec{N}$  and  $\vec{L}$  are defined as follows:

$$\vec{N} = \iint_{surface} (\hat{x}J_x + \hat{y}J_y + \hat{z}J_z) \exp(jkr' \cos \Phi) dS' \quad 2.62$$

$$\vec{L} = \iint_{surface} (\hat{x}M_x + \hat{y}M_y + \hat{z}M_z) \exp(jkr' \cos \Phi) dS' \quad 2.63$$

Where  $\Phi$  is the angle between  $r$  and  $r'$  as shown in Figure 2.9 and  $r' \cos \Phi = x' \sin \theta \cos \phi + y' \sin \theta \sin \phi + z' \cos \theta$ . The far field scattered light intensity can be written as below,

$$I(\theta, \varphi) = \frac{1}{2} \text{Re}(E_{\theta} H_{\varphi}^*) + \frac{1}{2} \text{Re}(-E_{\varphi} H_{\theta}^*) \quad 2.64$$

#### 2.4.4. Validation of the numerical AETHER code

The AETHER code based on FDTD method and above described techniques was written in FORTRAN 90. In most of the cases in this thesis, the grid spacing used is  $\lambda/20$ . The validation of AETHER FDTD code was performed by comparing the results with Mie theory results. Figure 2.10 shows the full angle intensity changes of 3  $\mu\text{m}$  radius polystyrene bead with refractive index of 1.59 and in a Phosphate Buffered Saline (PBS) medium with refractive index of 1.334 [59].

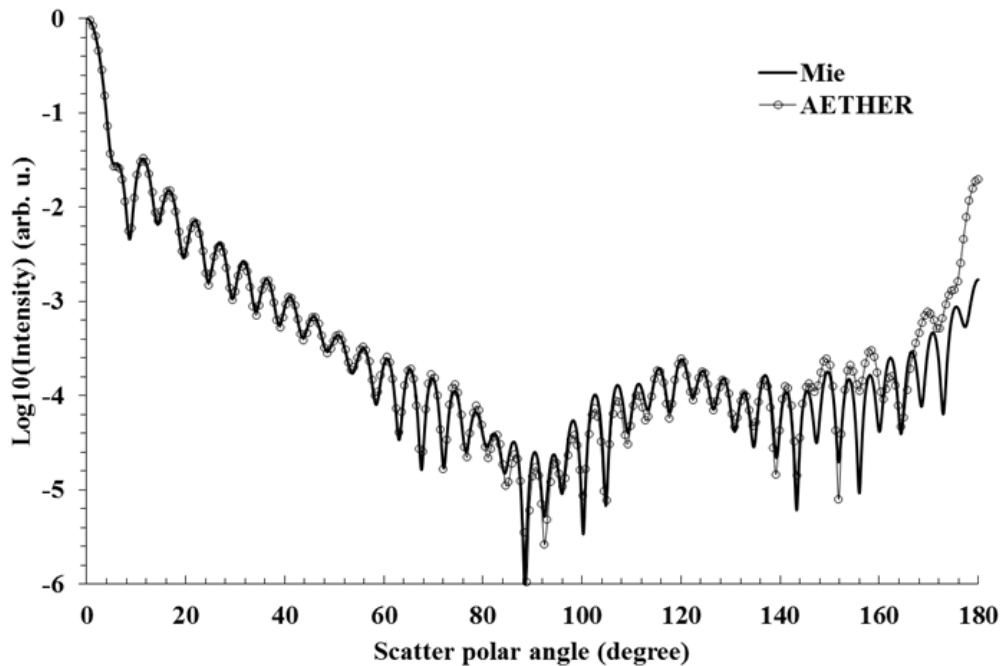


Figure 2.10: AETHER FDTD code validation compared with Mie simulation results.

There is a good agreement between the FDTD and Mie results. The agreement in forward and side directions are excellent. There are deviations in the backward direction but this can be improved by decreasing the size of the time steps. However, decreasing the size of the time step

increases the calculation time significantly. Since the two observation regions/angles of interest in this thesis are located in forward and side directions, the size of the time steps used should be sufficient.

## **2.5. Full angle scattering benefits**

Traditional cytometry is based a technique based on intensities of scattered light in a small cone angles in the forward and side directions. The intensity value in each direction is measured by a photodetector which measures the average light intensity in the small cone angles. The 2D scattered light patterns technique extends the traditional technique by collecting the scattered light in a larger cone angle and also uses a CCD camera which has many photodetectors allowing high angular resolution measurements. The 2D scattered light patterns of cells in previous works have been carried out only in the side direction [8-10, 55, 60]. In this thesis, a major step has been achieved demonstrating 2D scattered light patterns from both forward and side directions can be captured. This ability will provide us with better information about the cell including information about the cell's size, nucleus physical properties and small organelles distributions.

## **2.6. Viewing angle detection**

The three dimensional data from the ATHER code can be plotted on the surface of sphere in spherical coordinates  $(r, \theta, \varphi)$  as shown in Figure 2.11. In this simulation a 3  $\mu\text{m}$  radius bead with refractive index of 1.59 inside a medium with refractive index of 1.334 was assumed. The 632.8nm laser light travels along the Z-axis.

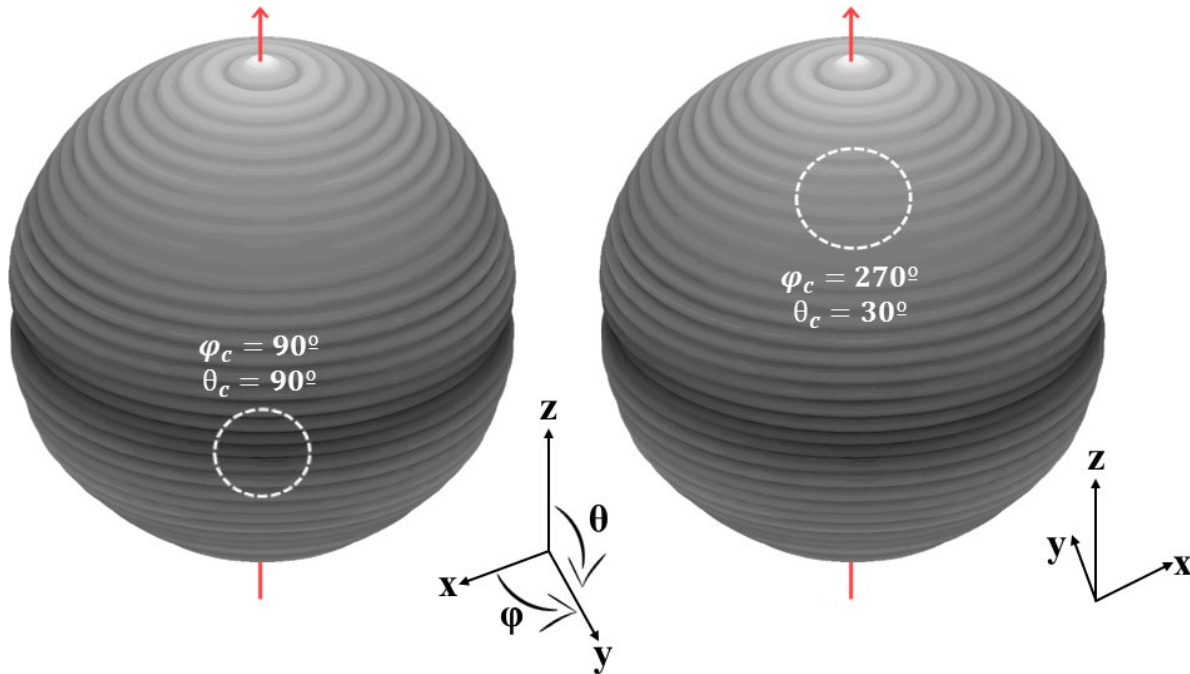
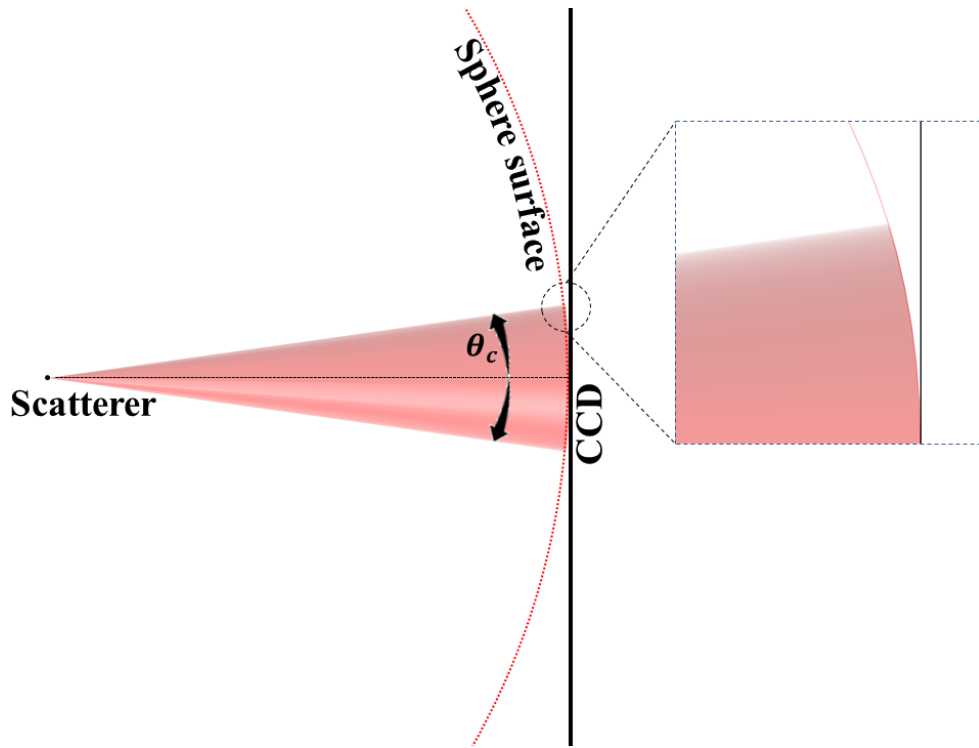


Figure 2.11: Two viewing angles are separated with dashed lines on AETHER simulated results for numerical model of 3  $\mu\text{m}$  radius bead.

To extract the simulation results so that it can be used to compare directly with the experimental 2D simulated scattered light patterns in both the forward and side directions, two separated viewing angles are shown in this figure. The white dashed circle on the right sphere represents the forward direction window specified with central azimuth angle,  $\varphi_c$ , of  $270^\circ$  and central polar angle,  $\theta_c$ , of  $30^\circ$  on the spherical surface. The range of  $\theta$  and  $\varphi$  are confined by optical system numerical aperture as it will be discussed in section 3.1.1. The left is the side direction circular window with  $\varphi_c = 90^\circ$  and  $\theta_c = 90^\circ$  for the range of angles that will be discussed later. Depending on the location of the camera, these windows will move and their place changes on the surface of sphere. In practice, the scattered light patterns in each window will transform on the surface of the flat CCD. There is a slight difference between the patterns on the surface of sphere and that on the flat CCD. This difference is small as the section of the sphere is approximately flat because the range of the viewing is only a fraction of 360 degrees. This

difference can be seen in Figure 2.12. To account for the change in the intensity of the scattered light, simulation data in the two experimental cone angles are multiplied by a  $\cos \theta'$  factor.



**Figure 2.12:** This figure illustrates the small difference of scattered pattern observed on the surface of sphere comparing to the scattered pattern observed on the surface of CCD camera.

The shape and size of the spherical surface element will be changed as it is mapped onto the flat CCD. Figure 2.13 shows the geometry relating the data in simulations and in experiments. The laser beam is in the  $z$ -direction. The light cone in the direction defined by  $\theta_0$ , with a cone angle  $\theta_c$  representing the scattered light collected by the experimental optical system. In Figure 2.13 the lab frame is represented by the Cartesian coordinate  $(X, Y, Z)$  while the frame rotated at an angle  $\theta_0$  with  $Z'$  as the axis of the cone angle is represented by  $(X', Y', Z')$ . Every point on the surface of sphere can be also be represented by in spherical coordinate as  $(r, \theta, \varphi)$  and a rotated spherical coordinate  $(r', \theta', \varphi')$ . The points defined by the light cone can be expressed in  $(r', \theta', \varphi')$  with  $r'=r$ ,  $-\theta_c < \theta' < \theta_c$  and  $0 < \varphi' < 2\pi$ .

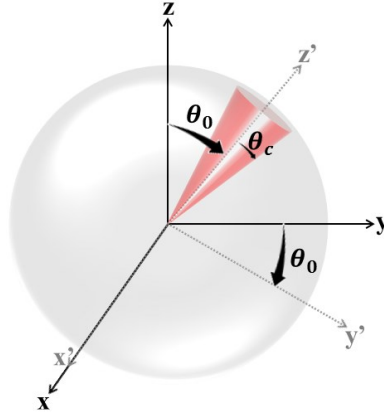


Figure 2.13: This figure shows the viewing cone angle

As follows,  $\theta'$  and  $\varphi'$  are needed to be expressed in terms of  $\theta$  and  $\varphi$  of the original frame, XYZ coordinate, where the numerical calculations are done:

$$z = z' \cos \theta_0 - y' \sin \theta_0 \quad 2.65$$

$$y = z' \sin \theta_0 + y' \cos \theta_0 \quad 2.66$$

$$x = x' \quad 2.67$$

Based on the rotated frame, X'Y'Z' coordinate, on the cone angle the  $x'$ ,  $y'$  and  $z'$  are defined as below:

$$x' = r' \sin \theta' \cos \varphi' \quad 2.68$$

$$y' = r' \sin \theta' \sin \varphi' \quad 2.69$$

$$z' = r' \cos \theta' \quad 2.70$$

Where  $r = r'$ . The spherical coordinates in the original frame ( $r, \theta, \varphi$ ) are defined as follows:

$$\theta = \cos^{-1} \frac{z}{r} = \cos^{-1} \frac{z' \cos \theta_0 - y' \sin \theta_0}{r}$$

Assuming  $\alpha = \frac{z' \cos \theta_0 - y' \sin \theta_0}{r}$ ,

$$\alpha_{r=r'} = \cos \theta' \cos \theta_0 - \sin \theta' \sin \varphi' \sin \theta_0 \quad 2.71$$

With use of similar calculations for  $\varphi$  and assuming  $\beta = \frac{z' \sin \theta_0 - y' \cos \theta_0}{x'}$ , the calculated  $\beta$  will be defined as below:

$$\beta_{r=r'} = \frac{\cos \theta' \sin \theta_0 - \sin \theta' \sin \varphi' \cos \theta_0}{\sin \theta' \cos \varphi'} \quad 2.72$$

Where  $\theta = \cos^{-1} \alpha$ ,  $\varphi = \tan^{-1} \beta$  and  $\theta'$  and  $\varphi'$  varies in the range defined based on the observation region window information.

The observation window on the surface of sphere defined by the cone of light is white circular. Although, this geometry will change as it transforms on the flat surface. These changes are more significant in the forward direction ( $\varphi_c = 270^\circ, \theta_c = 30^\circ$ ). This change is shown in the Figure 2.14. The left picture shows the forward direction circular observation window on the surface of a sphere. The right picture shows the corresponding non-circular white observation window on the flat surface.

To calculate the exact observation region in forward direction plotted on the CCD flat screen, the forward direction white window in Figure 2.14 right picture should be transferred and compressed into red region. This transformation provides better comparisons of experimental and simulated results. This can be attempted as a future work for much accurate studies. Presented forward direction simulated 2D results on this thesis work are cropped red circular region from white region.

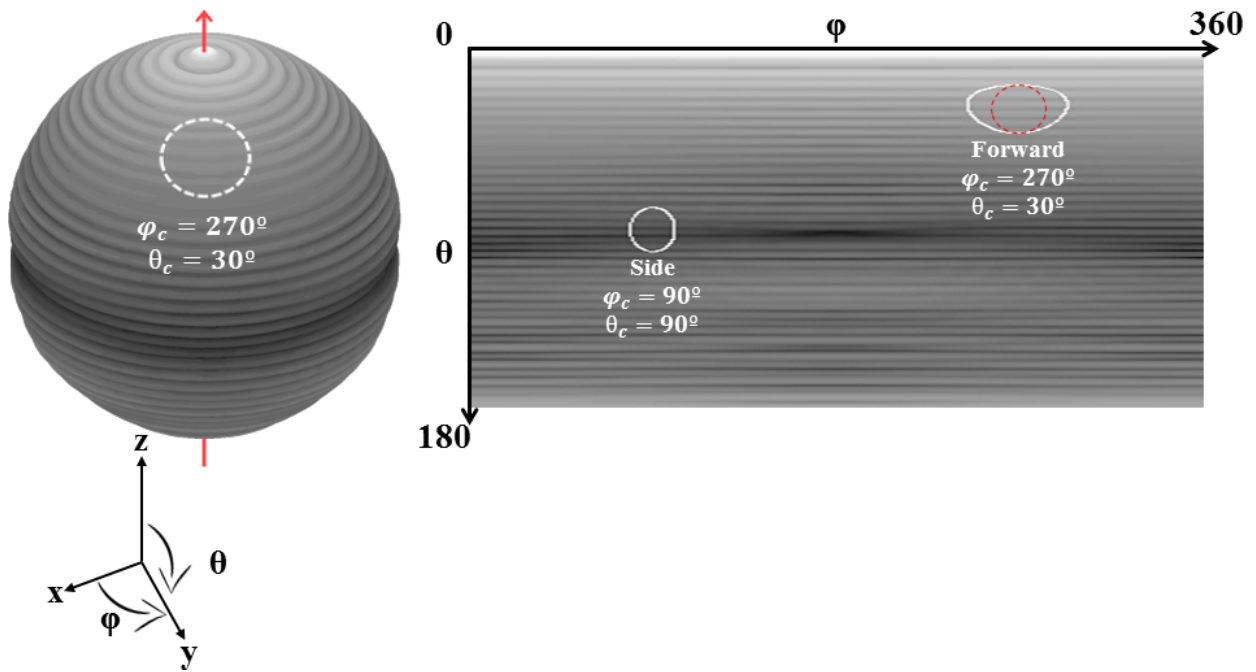


Figure 2.14: This figure shows a simulated scattered pattern mapped on the surface of sphere (left) and the simulated pattern expanded on the flat surface of CCD (right).

## **3. Light scattering study of beads**

### **3.1. Introduction**

Studies of laser light scattering of beads are important since beads are used as a surrogate for cells. Previous studies [8-10, 55, 60] were focused on side scattering direction but in this thesis, studies on both side and forward directions are carried out. A customly designed sample holder and cuvette have been used to minimize optical distortion of the 2D scattered light pattern measurements. This setup is capable of capturing simultaneously 2D scattered light patterns of a single cell in two directions of side and forward, providing us with more information about the cell. The 2D scattered light patterns for spherical polystyrene latex beads of different sizes in two directions are obtained and compared to results from Mie theory calculations. The 2D scattered light patterns of non-spherical polystyrene are also obtained and compared to results from FDTD simulations.

#### **3.1.1. Setup design**

The two ranges of viewing angles in the forward and side directions are defined based on information desirable and limitations of experimental setup. Viewing angles of about  $30^\circ$  respected to the laser beam direction would mainly provide information about the nucleus of the cell in terms of nucleus to whole cell volume ratio [48]. Viewing angles of about  $90^\circ$  in the side direction would mainly provide information on the cell's internal structure such as mitochondria's size and their distributions inside cells [5, 48].

The setup used in this thesis work is shown in Figure 3.1. The laser source is a HeNe laser (Melles Griot, USA) with  $\sim 1$  mW power output at  $\lambda = 632.8$  nm wavelength and the rest of the components are two microscope objectives and two CCD cameras. Other lasers with different wavelengths are also possible candidates as a light source and a brief discussion about the tradeoffs in wavelengths is presented in Appendix A.2.

The HeNe laser that has been used in this project is randomly polarized according to manufacturer specifications. The polarization of the laser has been checked experimentally using a Glen polarizer. The intensities on “s” and “p” directions were fluctuating for about 10 minutes and after it became stable and the intensities on both directions were approximately equal. Most of the data for the 2D light scattering patterns were collected after the laser become stable.

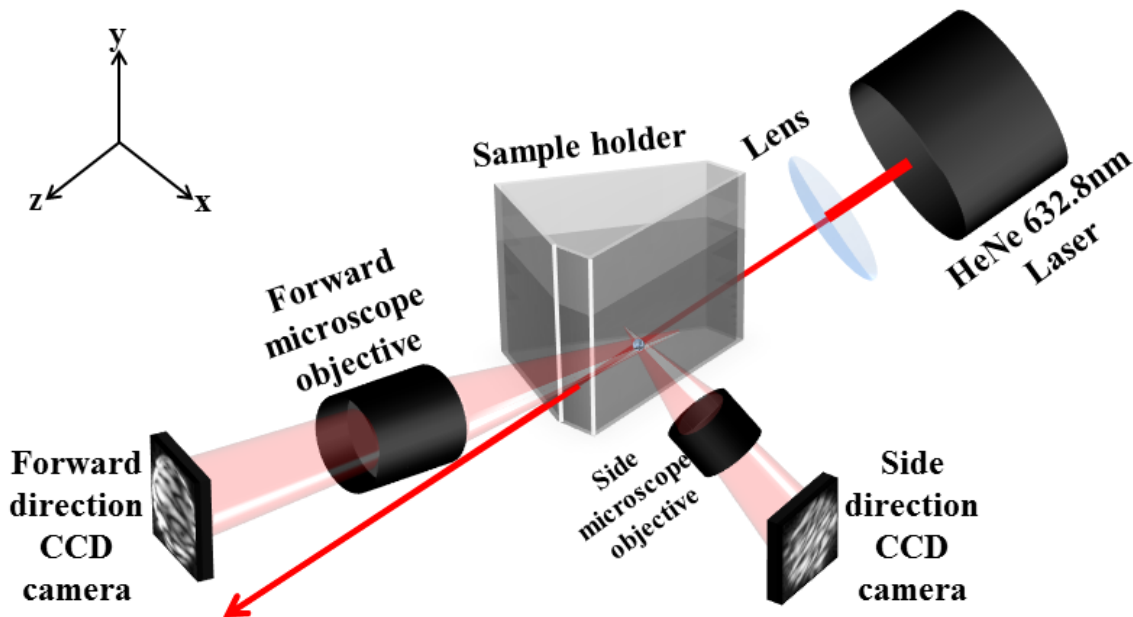


Figure 3.1: Improved new designed experimental setup used in this project. Two viewing windows are shown aligned with side and forward direction's cameras. A laser light will be focused in the middle of new designed cuvette.

The observed 2D scattered light patterns in the forward direction would contain intense unwanted noises if the viewing angles are chosen too close to the laser beam. For the forward

direction, central viewing angle of  $30^\circ$  has been chosen to avoid the intense laser beam blinding the CCD camera.

The optical system for collecting scattered light in forward direction consists of long working distance (LWD) microscope objective, (Mitutoyo infinity-corrected LWD), with numerical aperture (NA) of 0.28 attached to a CCD camera, (ICX445, Sony, Japan), with a 17 cm collecting tube. In the side direction, the viewing angle of  $90^\circ$  has been chosen. The optical system in this direction consists of a microscope objective, (Leitz Wetzlar 10/0.25) with NA = 0.25, with a 16 cm collecting tube, and a CCD camera, (ICX445, Sony, Japan). The range of viewing angles of scattered light collects by the optical system is defined by the microscope objective's numerical aperture (NA). The numerical aperture of an optical system is defined a

$$NA = n \cdot \sin \theta \quad 3.1$$

Where  $n$  is the refractive index of the medium surrounding the beads at the laser wavelength and  $\theta$  is the half-angle of the cone of light that can enter the lens. In most cases in this thesis project, the beads or cells are diluted in a buffer solution of phosphate buffered saline (PBS) with refractive index of 1.334 while the lens is in the air. We have implemented relative refractive index of  $n_{rel} = \frac{n_{PBS}}{n_{air}} = \frac{1.334}{1} = 1.334$  in our calculations. Figure 3.2 illustrates the path of scattered light propagates from the scatterer to the lens. The scattered light travels through three mediums with different refractive indices. Since the glass is in the middle of two other media, PBS and air, its refractive index does not play a role because of the Snell's law ( $\frac{\sin \theta_1}{\sin \theta_2} = \frac{n_2}{n_1}$ ). Using the law,  $n_{PBS} \cdot \sin \theta_1 = n_{glass} \cdot \sin \theta_2$  and  $n_{glass} \cdot \sin \theta_2 = n_{air} \cdot \sin \theta_3$ , led to

$n_{PBS} \cdot \sin \theta_1 = n_{air} \cdot \sin \theta_3$ , and thus the relative refractive index  $n_{rel} = \frac{n_{PBS}}{n_{air}}$  is used in the calculations.

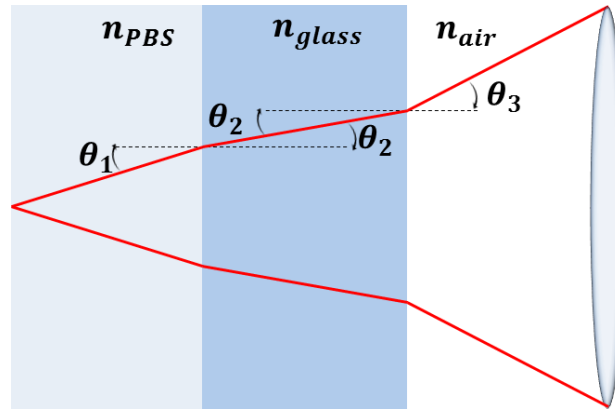


**Figure 3.2:** The scattered light beam will pass three medium with different refractive indices as it propagates from the scatterer to be observed by lens.

As the forward direction optical system equipped with LWD microscope objective with  $NA = 0.28$ , the calculated viewing angles will cover a range of  $\sim 24^\circ$  ( $\theta \approx 12^\circ$ ) in a central viewing angle of  $\theta = 30^\circ$ , leading to a viewing angles of  $18^\circ < \theta < 42^\circ$ . Similarly in the side direction viewing angles of  $79^\circ < \theta < 101^\circ$  ( $\theta \approx 11$ ) will be captured by the  $NA = 0.25$  microscope objective when it is aligned with a central viewing angle of  $\theta = 90^\circ$ . Based on configuration of optical systems, azimuth angle,  $\Delta\phi$ , varies for the same range as  $\Delta\theta$  from  $258^\circ < \phi < 282^\circ$  and  $79^\circ < \phi < 101^\circ$  in forward and side directions respectively.

The customly designed cuvette used in this project was designed to operate in the two ranges of viewing ranges in the forward and side directions. As shown in Figure 3.3, the surface of the forward direction window of the cuvette is normal to the direction of the central viewing angle of  $30^\circ$ . The surface of the side direction window is normal to the other cone viewing angle centered at  $90^\circ$ . The cuvette's windows are made from plain microscope slides approximately 1.0 mm thick and with a refractive index of 1.514.

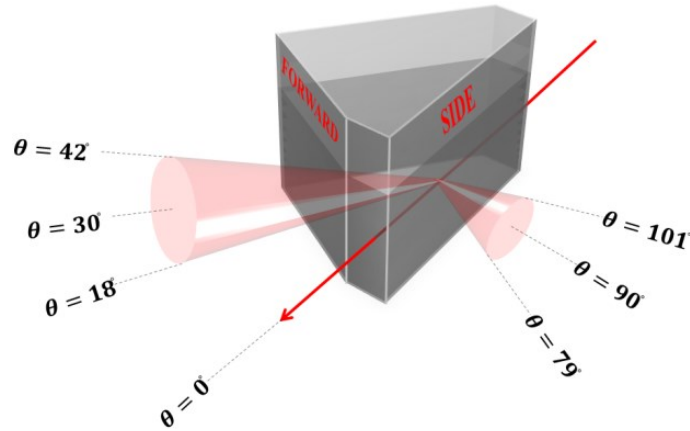
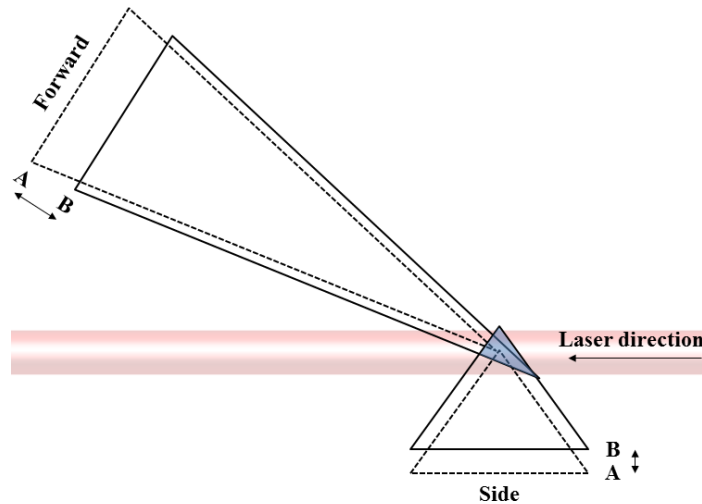


Figure 3.3: The cuvette designed with forward and side direction windows.

The cone angles in both directions and the laser light beam define an observation region. When a scatterer enters this region, its scattered light will be captured simultaneously by the 2 CCD cameras. The lens radius of LWD microscope objective in forward direction is 9 mm while the side direction microscope objective has a lens of 2.75 mm radius size. The LWD microscope objective has focal length of 20 mm and side direction microscope objective has focal length of 4.4 mm. These two microscope objectives define two light cones which the light could get to the CCD cameras. It has been experimentally determined that by defocusing in forward direction optical system for 300  $\mu\text{m}$  and 200  $\mu\text{m}$  in side direction optical system, desirable 2D scattered light patterns can be observed. These movements of cameras will limit volume region of 0.0057  $\text{mm}^3$  and 0.002  $\text{mm}^3$  in forward and side direction cone volumes in common with laser beam. Figure 3.4 shows top view schematic of limited region on each cone volume due to the movements with interact with laser beam as explained. As it is shown, the cone volumes moves from position “A” to “B” along their central defined angles of 30° in forward and 90° in side directions with respect to the laser beam direction. A volume of 0.002  $\text{mm}^3$  will be confined due

to these movements enabling us to capture scattered patterns of beads and cells entering this region (highlighted with blue in Figure 3.4).



**Figure 3.4:** Top view schematic of cone volume movements in forward and side directions from position “A” to “B” for 300  $\mu\text{m}$  in forward and 200  $\mu\text{m}$  in side directions.

In the experiment a 105/125 optical fiber<sup>2</sup> is used for aligning the forward and side direction optical systems as shown in Figure 3.5-A. The laser beam and the optics are aligned so that the image of the laser beam lights up the tip of the optical fiber and it appears on approximately the center of screen of both CCD cameras. CCD cameras were connected to a computer equipped with FlyCap 2 software (provided by PointGrey, CCD cameras manufacturer) to record 30 fps videos of simultaneous 2D scattered light patterns in forward and side direction screens. Focused images of optical fiber simultaneously captured in forward and side directions are shown in Figure 3.5-B and C respectively. Microscope objectives are then defocused for 300  $\mu\text{m}$  and 200  $\mu\text{m}$  in forward and side directions respectively. Defocused images of optical fiber simultaneously captured in forward and side directions are shown in Figure 3.5-B' and C'. Figure 3.5D-D' illustrates focused and defocused images in side direction camera from 10  $\mu\text{m}$  diameter size

<sup>2</sup> 105/125 optical fiber is a fiber with core diameter of 105  $\mu\text{m}$  and cladding diameter of 125  $\mu\text{m}$ .

polystyrene beads sample inside PBS medium (10  $\mu\text{m}$  microsphere bead was used due to availability on the time of experiment).

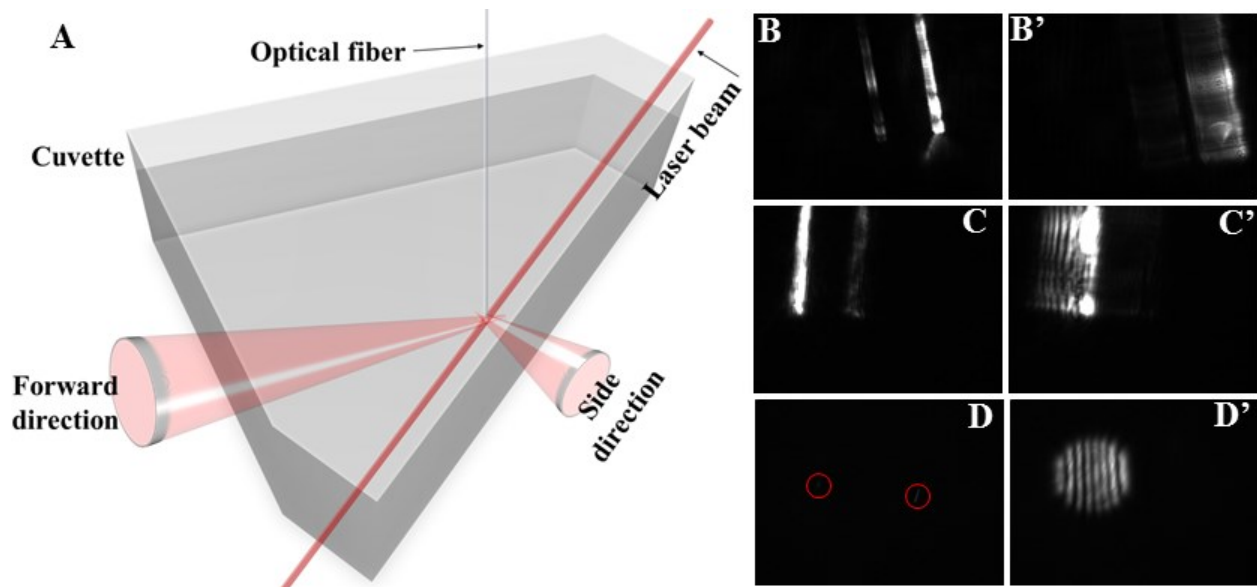


Figure 3.5: Optical fiber used to calibrate and focused two optical systems to same area. Focused images of optical fiber and defocused images are shown. 2 beads captured in (D) are circled red.

### 3.2. Polystyrene spherical beads experimental and simulated results

Samples with PBS solution containing  $1000 \frac{\text{beads}}{\text{mL}}$  of spherical polystyrene latex beads with different diameters of 4  $\mu\text{m}$ , 6  $\mu\text{m}$  and 10  $\mu\text{m}$  beads have been used for experiments. Simulated results of scattered light intensity<sup>3</sup> as a function of viewing angles for these beads in PBS solution using MiePlot is shown in Figure 3.6.

<sup>3</sup> In this thesis, the Mie theory calculations are based on unpolarized incident laser light unless it has been specified otherwise.

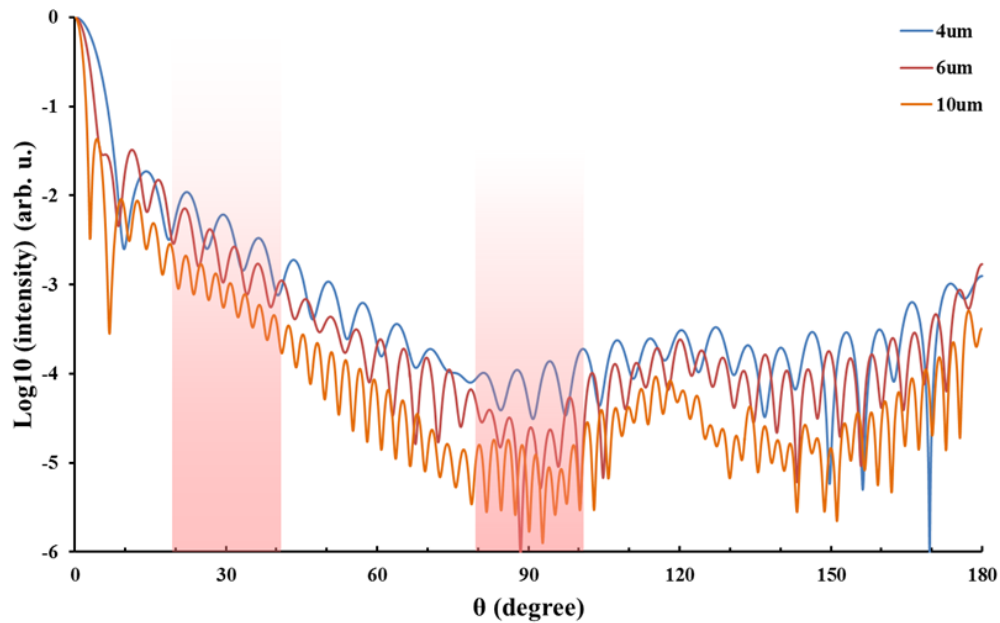


Figure 3.6: Simulated MiePlot results for beads of 4  $\mu\text{m}$ , 6  $\mu\text{m}$  and 10  $\mu\text{m}$  diameter sizes in PBS solution.

The beads and PBS solution have refractive indices of 1.591 and 1.334 respectively at the laser wavelength of 632.8nm [61, 62]. The experimental viewing windows for the angles in forward and side direction angles are highlighted in red color. It can be seen from Figure 3.6 that there are about 3 fringes in forward 2-3 fringes in side direction for 4  $\mu\text{m}$  bead while there are  $\sim 5$  fringes in both direction for 6  $\mu\text{m}$  beads. There are 6-7 and 7-8 fringes in forward and side directions respectively for 10  $\mu\text{m}$  beads. Experimental results for forward and side directions are shown in Figure 3.7. There are good agreements between experimental and simulation results. There is a slight difference between forward patterns and in particular for 10  $\mu\text{m}$  diameter bead experimental results with what it should be expected as vertical fringes. This is due to the effect of pattern transformation from the surface of the sphere on the flat CCD camera as described in section 2.6 that may lead to some pattern deformations that should get considered in future use of this system.

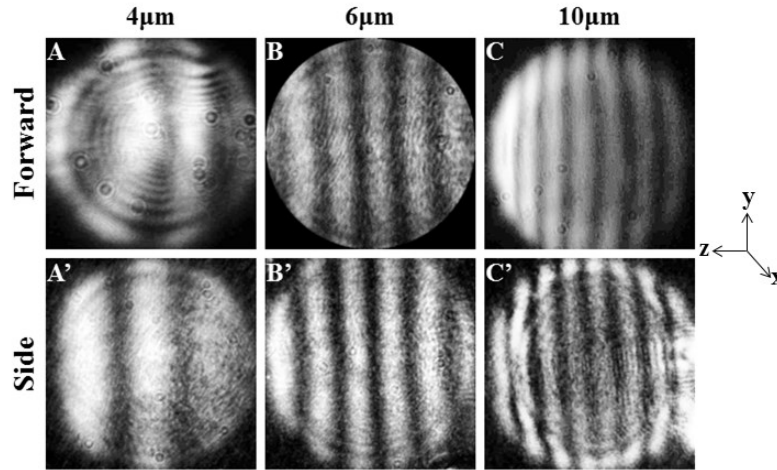
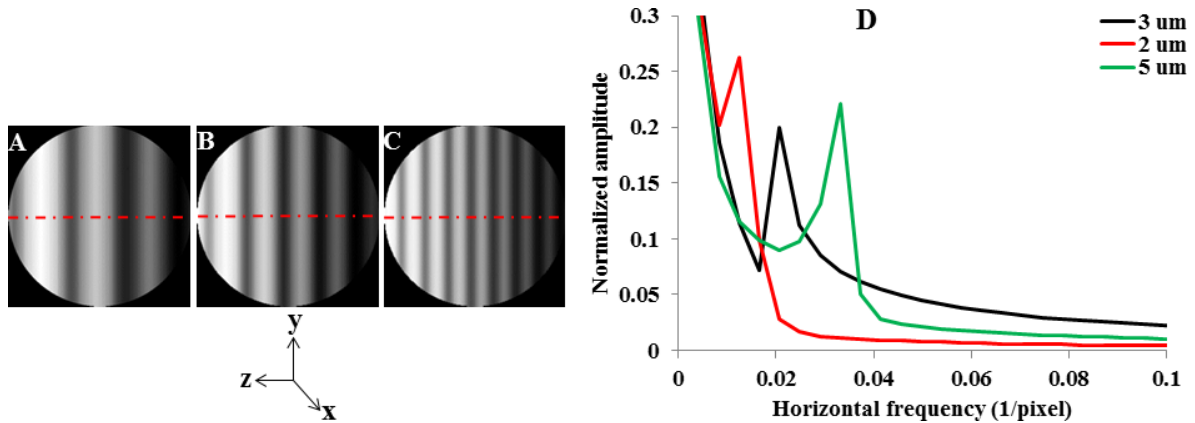


Figure 3.7: Observed forward and side direction scattered patterns from polystyrene latex beads diluted PBS solution. A-A' shows the 2-3 fringes in forward and 4 fringes in side direction. B-B' show 5 fringes in forward and side directions. There are 7 fringes in forward and 8 fringes in side direction of 10  $\mu\text{m}$  bead's scattered patterns (C-C').

### 3.3. Beads radius vs. periodic harmonics

Quantitative comparison of experimental and numerical results is discussed in this section. As presented in Figure 3.7, the number of fringes is increasing as the diameter of beads increases. As the micro-spherical polystyrene beads generate periodic fringes along the horizontal axis, z-axis, 1D FFT has been used to extract the harmonics in horizontal direction of forward direction 2D scattered light patterns as shown in Figure 3.8. A row of data from the middle region of each 2D scattered light pattern function were extracted as shown in red dashed line in Figure 3.8A-C and used as input for the 1D FFT function. Normalized 1D FFT spectrums for beads with various sizes are shown in Figure 3.8D. The output values in the figure were normalized to the maximum value in each output dataset. Presented patterns, Figure 3.8A-C, are simulated forward direction 2D light scattered patterns of 4  $\mu\text{m}$ , 6  $\mu\text{m}$  and 10  $\mu\text{m}$  diameter size plastic respectively. As the bead size increases, the highest frequency peak moves toward the higher frequencies due to increase in the number of the fringes in 2D light scattered patterns. 4  $\mu\text{m}$ , 6  $\mu\text{m}$  and 10  $\mu\text{m}$

diameter size bead have the highest horizontal frequency peak at  $0.0124 \frac{1}{pixel}$ ,  $0.02075 \frac{1}{pixel}$  and  $0.0331 \frac{1}{pixel}$ .



**Figure 3.8:** (A)-(C) shows the simulated forward direction 2D light scattered pattern of 4 μm, 6 μm and 10 μm diameter size plastic bead respectively, dashed red line in the input values for 1D FFT function. (D) shows the measured horizontal frequency peaks of (A)-(C).

1D FFT analysis have been performed for forward direction experimental results shown in Figure 3.7 and the frequencies of the peaks were compared with numerical results. As shown in Figure 3.9, there is a good agreement between experimental and numerical results. The slight difference between the experimental and numerical results could be due to the inaccuracy of the size of the beads and the accuracy of defining the peak in the numerical results due to the resolution of the data. Based on the beads manufacturer data sheet, there are 5% size variations for 4 μm and 10% for 6 and 10 μm diameter size beads. This analysis can be used for practical purposes of size measurements from beads and cells.

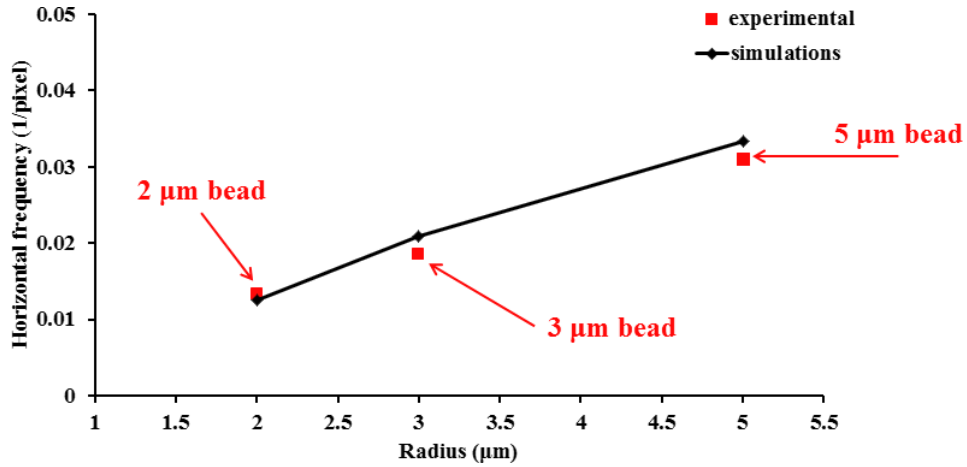


Figure 3.9: Most dominant 1D FFT horizontal frequency comparison of forward direction 2D light scattered patterns of experimental and numerical results for polystyrene beads.

### 3.4. Elliptical polystyrene latex beads

Laser light scattering studies of non-spherical shape latex beads have also been carried out. The experimental results have been compared with results from FDTD simulations. Elliptical beads (Non-Spherical particles, MagSphere, USA) used in this project have dimension of  $r_x = r_z = 2 \mu\text{m}$  (minor radii) and  $r_y = 3 \mu\text{m}$  (major radius) as shown in Figure 3.10. The beads are made from polystyrene having a refractive index of 1.59 at laser wavelength of 632.8 nm.

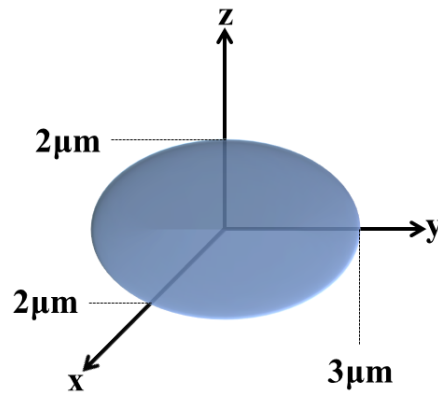


Figure 3.10: Experimental ellipsoid geometry dimensions.

A sample solution of  $1000 \frac{\text{beads}}{\text{mL}}$  has been used in the experiments. The 2D scattered light patterns of the elliptical beads simultaneously recorded in both forward and side directions are

shown in Figure 3.11. The fringes in the elliptical beads' patterns are no longer always vertical in contrast to those in the spherical beads' patterns. Non-vertical fringes in 2D scattered light patterns have been reported previously from non-spherical scatterers [51, 58]. Aptowiz *et al.* [51] have shown in their study of airborne particles when they get deformed led to non-vertical fringes in similar experimental 2D scattered light patterns. Additionally, Lu *et al.* [58] have numerically modeled a biconcave red blood cell (RBC) with different orientation with respect to the laser light direction and skewed fringes are presented in their simulated results.

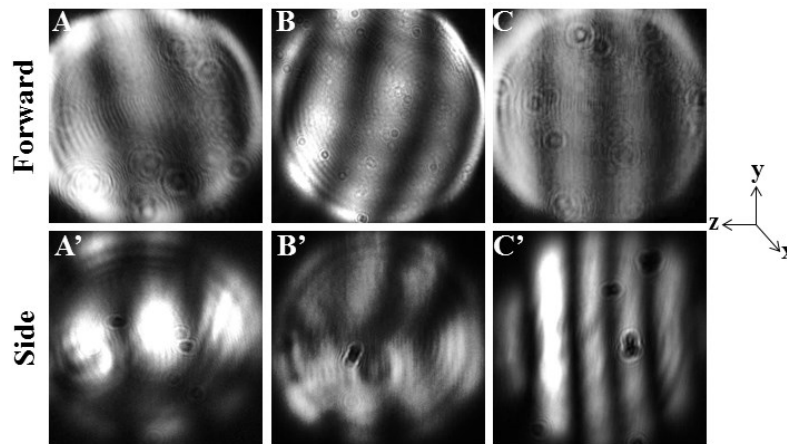


Figure 3.11: Experimentally scattered patterns from elliptical latex beads sample.

Because an elliptical bead no longer has spherical symmetry, its various orientations could lead to the different experimental 2D scattered light patterns shown in Figure 3.11. The orientation effect can be studied by using FDTD simulations<sup>4</sup>. As shown in Figure 3.12, different simulated 2D scattered light patterns have been generated from elliptical beads at different orientations.

<sup>4</sup> In this thesis, FDTD simulations are based on unpolarized incident laser light unless it has been specified otherwise.

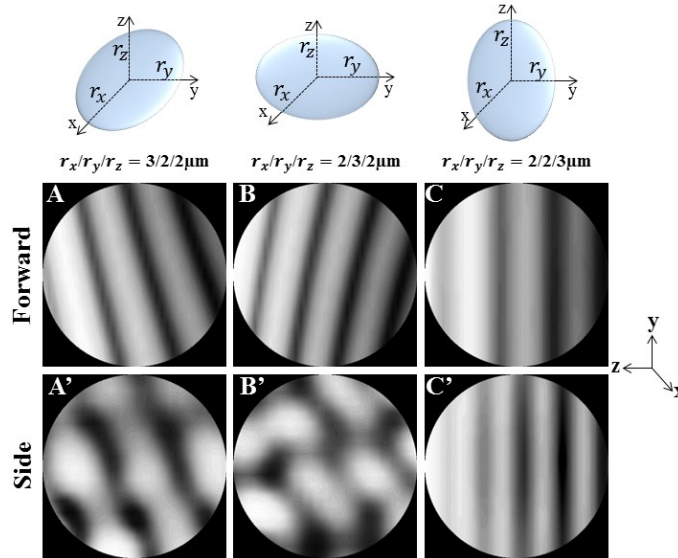


Figure 3.12: Numerical elliptical shape models are presented in this figure. Model A shows the elliptical bead along the X-axis and the scattering patterns are shown. Model B and C show elliptical bead along Y-axis and Z-axis generated scattering patterns respectively.

As an elliptical bead is rotating with respect to the  $z$ -axis (the laser beam direction) the laser beam would see different cross-section of the bead on the XY-plane as shown in Figure 3.13. Areas highlighted with red, green and blue represent the XY-plane cross-sections of elliptical beads in orientation A, B and C respectively. The non-circular cross-sections in orientation and B led to non-vertical fringes while the circular cross-section of orientation C led to the vertical fringes. There are good agreements between the simulated 2D scattered light patterns shown in Figure 3.12 and those observed from experiments shown in Figure 3.11.

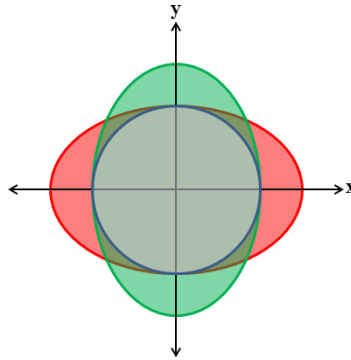


Figure 3.13: This figure illustrates the geometry that laser beam traveling along the Z-axis sees on XY-plane cross-section of each of elliptical bead rotations shown in Figure 3.12.

To further study the effect due to elliptical with different shapes, simulations for elliptical beads with different aspect ratios of major radius,  $r_y$ , over minor radii,  $r_x = r_z$ , have been carried out. As shown in Figure 3.14, simulations have been performed for several aspect ratio of  $\frac{r_z}{r_y}$  from 1 to 0.1 with a fixed major radius of  $r_y = 3 \mu\text{m}$ ,  $n = 1.39$ ,  $n_{\text{medium}} = 1.334$ . Simulated 2D scattered light patterns in forward direction are confined with  $18^\circ < \theta < 42^\circ$  and  $\varphi$  range of  $24^\circ$  while the side direction simulated patterns are confined with  $79^\circ < \theta < 101^\circ$  and  $\varphi$  range of  $22^\circ$ .

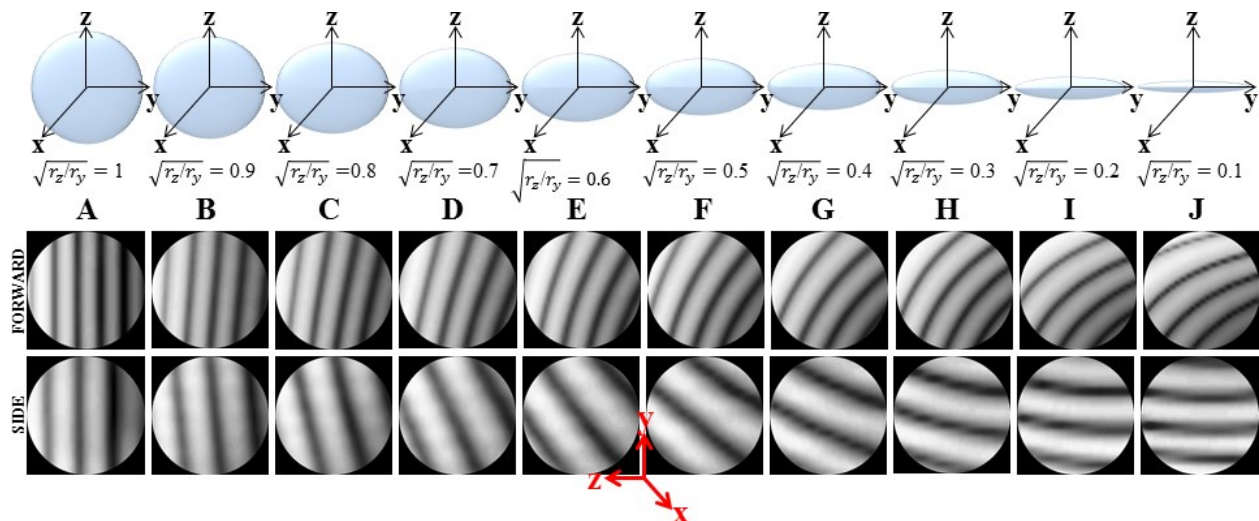


Figure 3.14: Aspect ratio changes are studied with use of numerical modeling and AETHER simulated results presented in this figure. The elliptical aspect ratio of  $\sqrt{\frac{r_z}{r_y}}$  changed from 1-0.1 in presented A-J models. The fringes orient as the aspect ratio varies from A-J.

As it can be seen in Figure 3.14, the fringes in the 2D scattered light patterns in both the forward and side directions become increasingly non-vertical as the aspect ratios increase. To better illustrate the above effect, the simulated 2D scattered light patterns for the full range of the azimuth angles at  $0^\circ < \varphi < 180^\circ$  for the various different aspect ratios are shown in Figure 3.15.

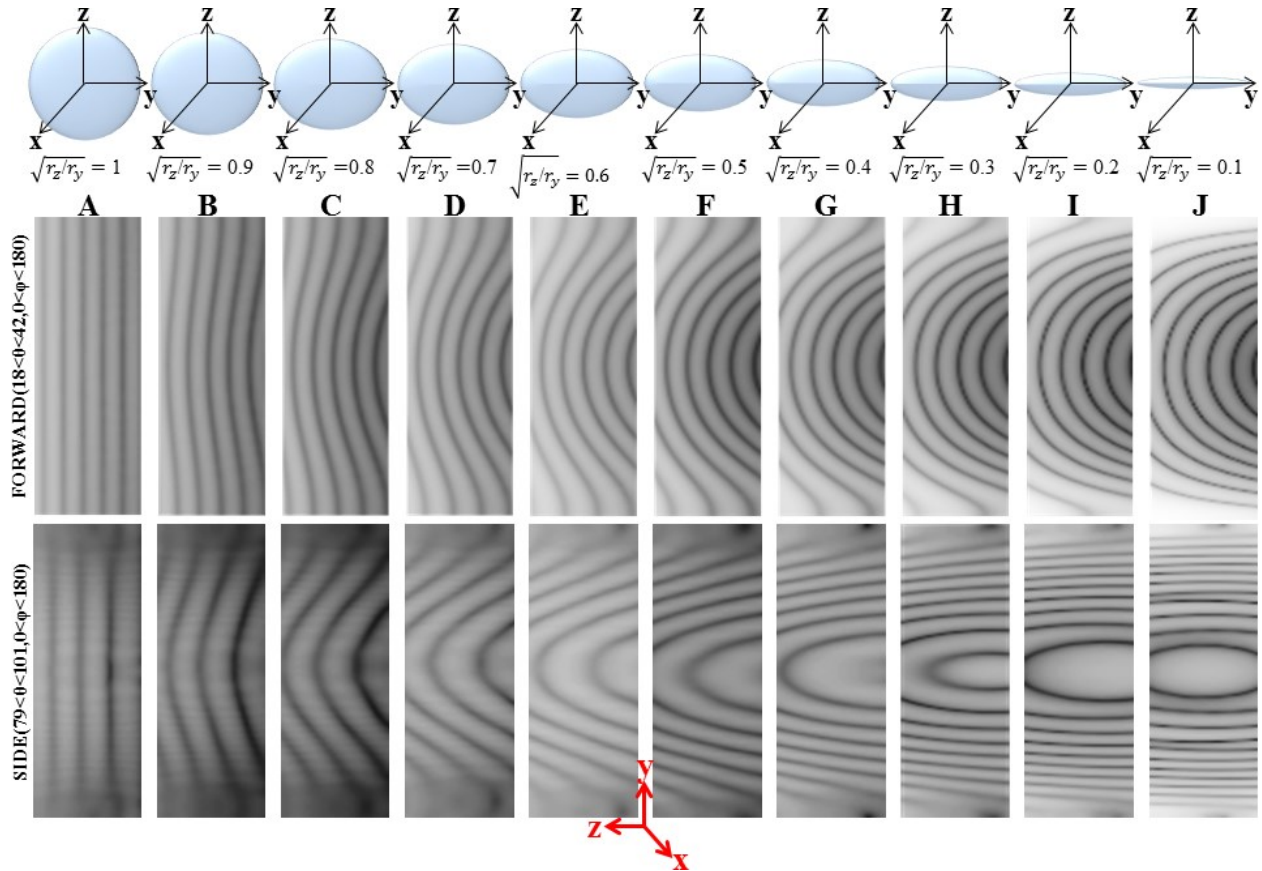
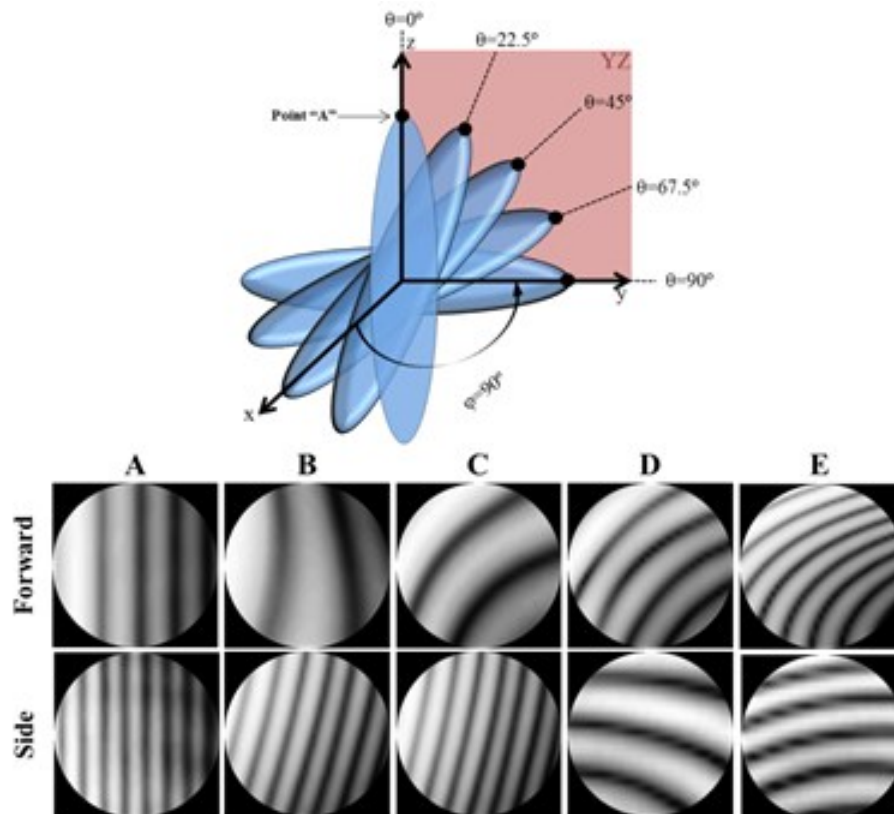


Figure 3.15: Simulated scattered patterns of aspect ratio variations in forward and side directions for  $0^\circ < \varphi < 180^\circ$ .

To further study the orientation effect, FDTD simulations are carried out with an elliptical bead with its major axis oriented at various angles respected to the laser beam direction. In the simulations the polar angles are changed while the azimuth angle is fixed. The simulated 2D scattered light patterns of an elliptical bead ( $n=1.39$ ) with radii  $(r_x, r_y, r_z) = (1 \mu\text{m}, 4 \mu\text{m}, 1 \mu\text{m})$  in a PBS medium ( $n= 1.334$ ) at various orientations are shown in Figure 3.16, in the simulations

the polar angles are changed ( $\theta = 0^\circ, 22.5^\circ, 45^\circ, 67.5^\circ$  and  $90^\circ$ ) while the azimuth angle is fixed at  $90^\circ$ . In general the fringes become increasingly more non-vertical and curved as the values of the polar angle increase. The increase in polar angles would lead to XY cross-section area with shapes increasingly deviate from circular.



**Figure 3.16:** Ellipsoid rotation is shown in this figure. Ellipsoid rotates over fixed  $\phi$  ( $\phi = 90^\circ$ ) for A)  $\theta = 0^\circ$ , B)  $\theta = 22.5^\circ$ , C)  $\theta = 45^\circ$ , D)  $\theta = 67.5^\circ$  and E)  $\theta = 90^\circ$ . Scattered patterns are simulated as shown in two directions of forward and side. Orientation of fringes can be seen due to ellipsoid rotation.

## **4. Light scattering study of cells**

### **4.1. Introduction**

The scattered light from the internal structures of a cell affects the 2D scattered light patterns in different directions differently. The internal components of a cell that are important in laser scattering studies are nucleus, mitochondria and cytoplasm (see section 1.2 for more details). Numerical studies have been carried out to investigate the effects of nucleus, mitochondria and cytoplasm on 2D scattered light patterns from a single cell in both the forward and side directions. The information gained have been used to archive a better understanding of the experimental 2D scattered light patterns from the hematopoietic stem cells and the Very Small Embryonic-like stem cells.

### **4.2. Nucleus**

Nucleus is the control center of the cell. Nucleus protects genetic materials, provides mechanical support and regulates gene expression. For some diseases, the shape of nucleus could change because the nucleus could be susceptible to damage due to mechanical trauma: muscle, bone, nerves. One striking nucleus related disease is progeria or premature aging. Patients exhibit signs of aging, such as hair loss, wrinkled skin, and atherosclerosis in children. For some cells, their nucleus size changes when cells health condition alters. Non regulated gene activity controlled by nucleus can cause disease such as Emery-Dreifuss muscular dystrophy. Emery-Dreifuss muscular dystrophy is a condition that chiefly affects muscles used for movement (skeletal

muscles) and heart (cardiac) muscle. It has been reported that Emery-Dreifuss muscular dystrophy reduces the cell nucleus size [63].

The studies of nucleus size and geometry changes become important to explore nucleus-related diseases. Numerical studies investigating the effect of nucleus sizes and shapes of a cell on its 2D scattered light patterns have been carried out.

#### 4.2.1. Nucleus size changes

The forward scattered light pattern from a cell is dominated by light scattered from the nucleus. To study how the sizes of nucleus affect the forward scattered patterns, simulations have carried out for single fictitious cells consist of A) only a spherical cytoplasm a radius of  $5\ \mu\text{m}$ , B) only a spherical nucleus of a radius of  $3\ \mu\text{m}$  and C) a combination of cases A and B i.e. a nucleus in a cytoplasm with a ratio of nucleus radius to cytoplasm radius of 0.6. The results of the simulations are presented in Figure 4.1. The refractive indices of nucleus and cytoplasm are assumed to be 1.39 and 1.35 respectively at a laser wavelength of  $632.8\text{nm}$ . The laser beam is assumed to be propagated along the Z-axis. The surrounding medium, PBS, has the refractive index of 1.334.

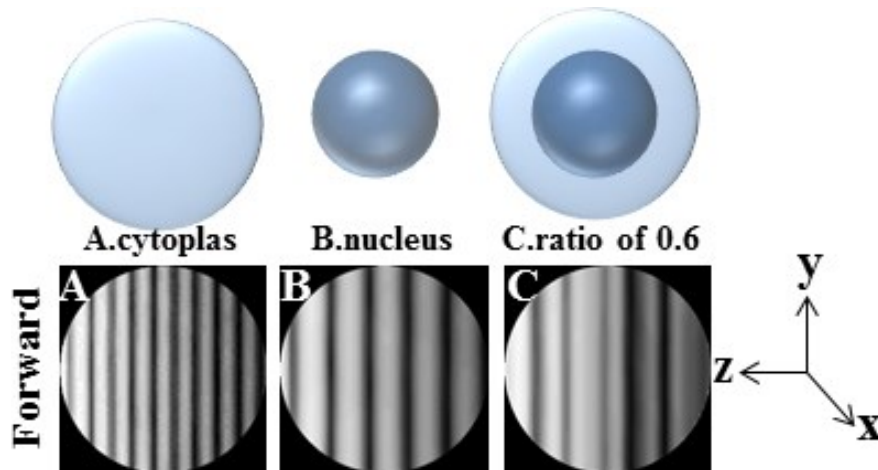


Figure 4.1: This figure shows the simulated forward direction patterns for A) solo cytoplasm, B) solo nucleus and C) cytoplasm and nucleus as whole cell.

Fast Fourier Transform (FFT) is applied to analyze the patterns in Figure 4.1. As shown in Figure 4.2-A, central square area of  $320 \times 320$  pixels is extracted from the simulated 2D scattered light pattern of Figure 4.1-C as an input for 2D FFT MATLAB function. The 2D FFT plot of the pattern of Figure 4.1 as a function of  $k_z$  and  $k_y$  is shown in Figure 4.2-B. Magnitude plot, Figure 4.2-B, shows the 2D FFT plot of the pattern of Figure 4.1-C as a function of  $k_z$  (k-vector component in horizontal axis) and  $k_y$  (k-vector component in vertical axis). The 2D FFT data give the characteristic frequencies of the sinusoid waves in the horizontal and vertical directions that made up the pattern.

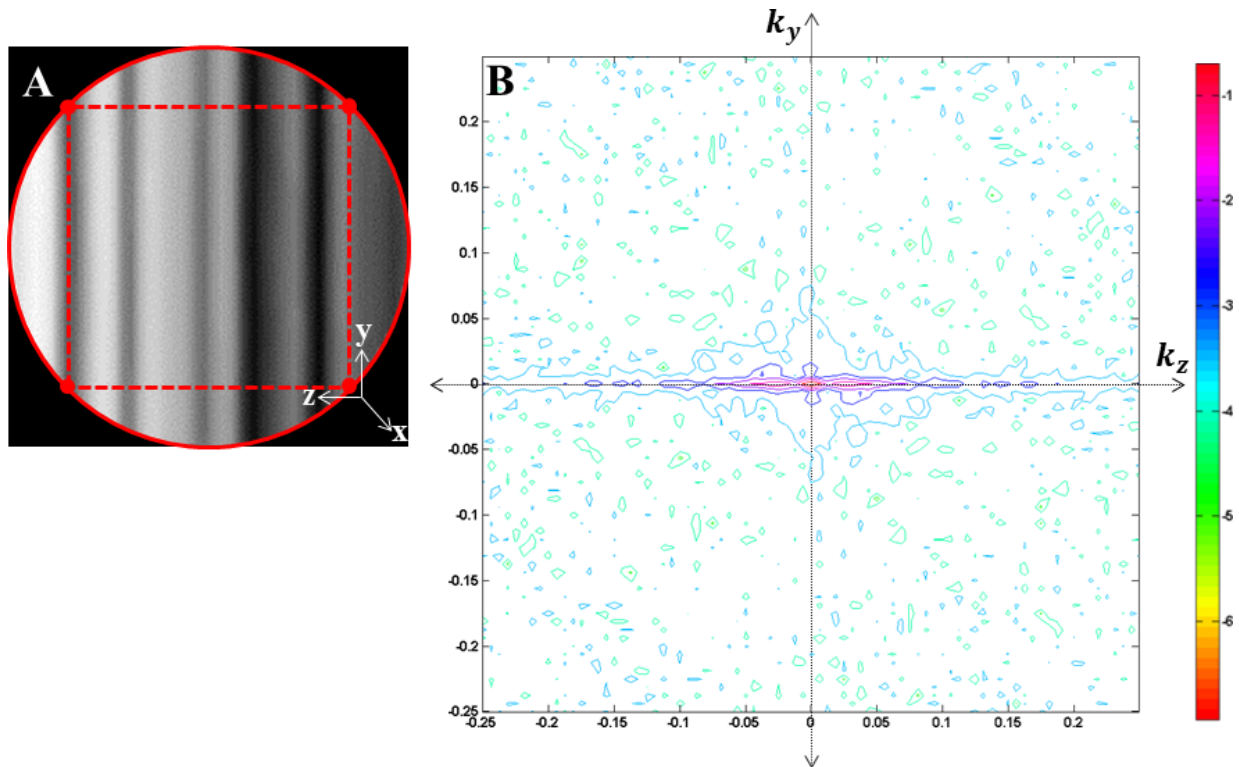


Figure 4.2: (A) Square area to be extracted for 2D FFT process. (B) Frequencies magnitude 2D plot as FFT function output.

Since the patterns in Figure 4.1 are periodic in the horizontal direction, only those 2D FFT data along the horizontal axis (1D FFT spectrum) are important. The calculation in Figure 4.2B was

carried out with increasing resolution by adding 8 data points in between two pixel values using the Matlab's interpolation function. This resulted in an increase of the original  $320 \times 320$  data points from the CCD pixels to the  $3200 \times 3200$  data points used in the calculations.

The horizontal 2D FFT data for patterns in Figure 4.1-A-B-C are presented in Figure 4.3.

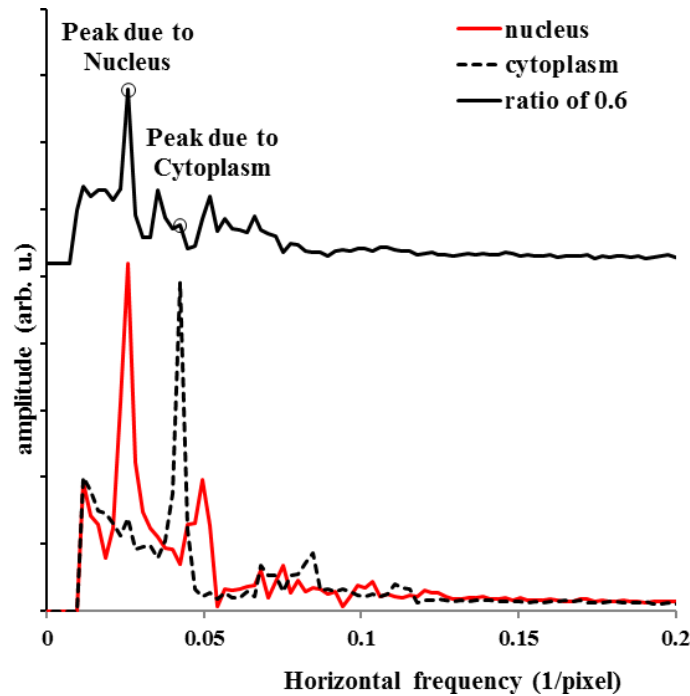


Figure 4.3: 1D FFT analysis of forward patterns in Figure 4.1

The red solid line represents 1D FFT spectrum of the 2D scattered light pattern of nucleus only (Figure 4.1-B). The solid black line represents 1D FFT spectrum of the 2D scattered pattern of nucleus and cytoplasm (Figure 4.1-C). The 1D FFT spectrum has a major peak and a number of smaller peaks. The major peak has the same frequency as that of the nucleus only case (red solid line). The 1D FFT spectrum for the cytoplasm only case is shown in dashed black line has a dominant peak but this peak is not presented in the 1D FFT spectrum of the nucleus in cytoplasm case. These results indicate that the 2D scattered light pattern of a cell in the forward direction is strongly dependent on the properties of the cell's nucleus.

For better understanding of the nucleus size effect on 2D scattered light patterns in the forward direction, different nucleus sizes inside a fixed sized cytoplasm of a radius of  $5\ \mu\text{m}$  are simulated. Both the nucleus and the cytoplasm are assumed to be spherical. The refractive indices of the nucleus and the cytoplasm are 1.39 and 1.35 respectively. Figure 4.4 shows the simulated forward 2D scattered light patterns for various numerical models. The model "A" has only a nucleus with a radius of  $3\ \mu\text{m}$  and no cytoplasm. The forward 2D scattered light pattern of model "A" shows  $\sim 6$  clear vertical straight fringes. The model "B" has a nucleus with a radius of  $3\ \mu\text{m}$  located inside a cytoplasm with radius of  $5\ \mu\text{m}$  giving a ratio of nucleus radius to cytoplasm radius of 0.6. The forward 2D scattered light pattern of model "B" shows  $\sim 6$  somewhat blurred vertical straight fringes. The models "C", "D" and "E" have different ratios of nucleus radius to cytoplasm radius of 0.7, 0.8 and 0.9 respectively. The forward 2D scattered light patterns of model "C", "D", "E" show blurred vertical straight fringes and their numbers of fringes increase as the nuclei increase in size. The final model "F" has only a cytoplasm and no nucleus. The forward scattered 2D light pattern of model "F" shows  $\sim 10$  clear vertical straight fringes.

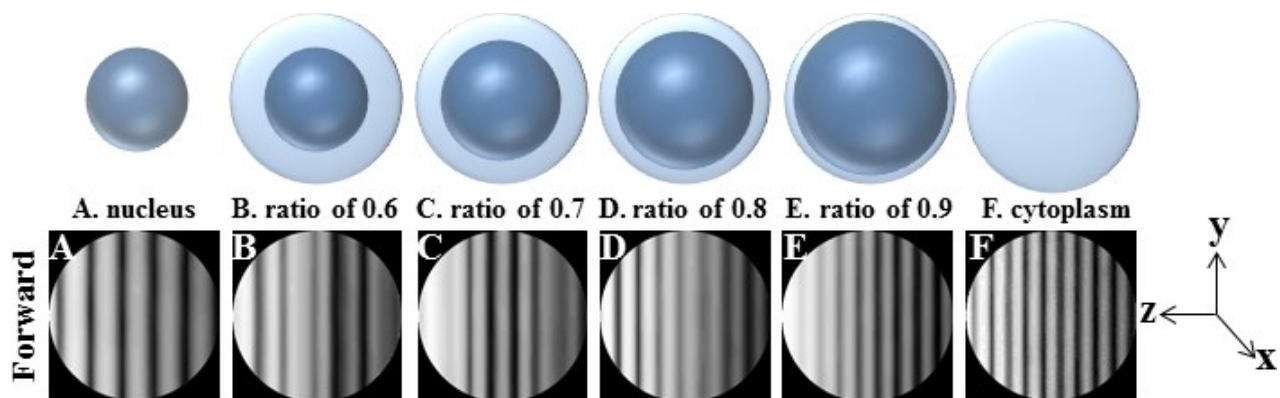


Figure 4.4: Simulated forward 2D scattered light patterns with various nucleus/cytoplasm size ratio.

To provide a more quantitative analysis of the results presented in Figure 4.4, the Fast Fourier Transform (FFT) technique is used. MATLAB's FFT function is used to calculate the 2D FFT spectral of the scattered light patterns. The 1D FFT spectral is the data on the horizontal axis (x-axis) of a 2D FFT spectrum. The 1D FFT spectral of the forward scattered light patterns in Figure 4.4 are presented in Figure 4.5.

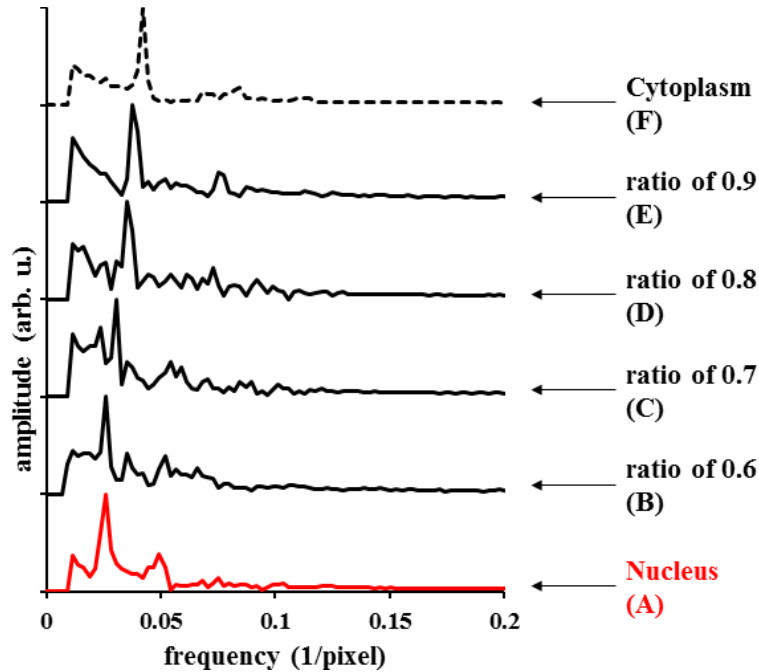


Figure 4.5: 1D FFT spectra of forward scattered light patterns in Figure 4.4.

The 1D FFT spectrum of model “A” with only a nucleus of 3  $\mu\text{m}$  radius shows a dominant peak at a characteristic frequency value of 0.025 which is defined by the nucleus’s radius and refractive index. The 1D FFT spectrum of model “B” with a nucleus of 3  $\mu\text{m}$  radius inside a cytoplasm shows a dominant peak also at a frequency value of 0.025. The 1D FFT spectrum of model “B” follows that of the model “A” closely with the exception that there are smaller peaks in the spectrum of model “B” due to the presence of cytoplasm. The main peaks in the 1D FFT spectral of models “C” to “E” shift towards higher frequencies as the sizes of the nuclei increase.

The 1D FFT spectrum of model “F” for cytoplasm, dashed black line, shows a dominant peak at a characteristic frequency of 0.042.

#### 4.2.2. Non-spherical nucleus

As shown in Chapter 3, the 2D scattered light patterns from latex beads with spherical shape consist of vertical straight fringes while those from latex beads with elliptical shape consist of curved fringes. It is expected that the nucleus shape is an important parameter for the 2D scattered light patterns of cells. In this section, the effect of nucleus with non-spherical shape will be investigated using FDTD simulations. The AETHER codes are used to generate the 2D scattered light patterns on the forward and side directions of three cases: (i) a spherical cytoplasm, (ii) an elliptical nucleus and (iii) a system with an elliptical nucleus inside a spherical cytoplasm. The results are presented in Figure 4.6 (A-A', B- B' and C- C' for (i), (ii) and (iii) respectively). In these simulations, the nucleus has an elliptical shape with radii of  $(r_x, r_y, r_z) = (2, 3, 2) \mu\text{m}$  and the spherical cytoplasm has a radius of  $5 \mu\text{m}$ . Refractive indexes are 1.39, 1.35 and 1.334 for nucleus, cytoplasm and PBS surrounding medium respectively.

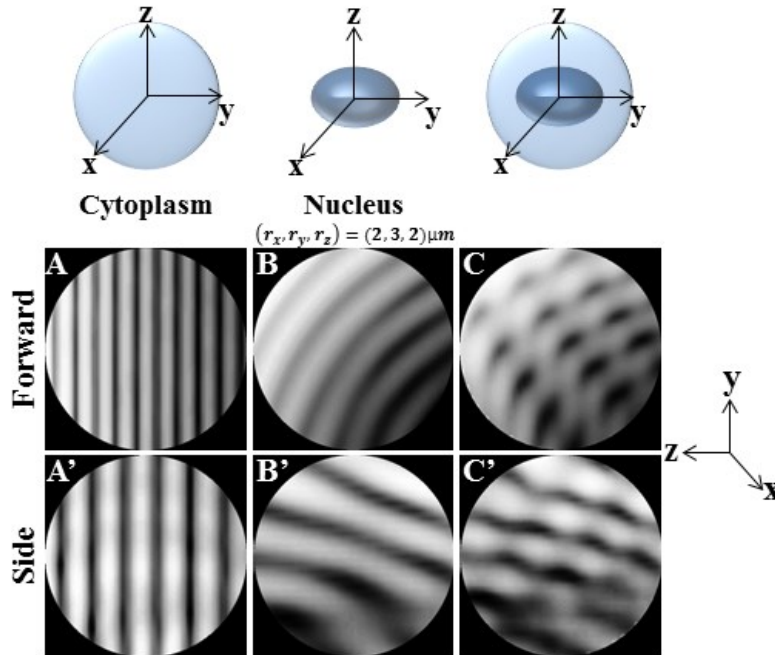


Figure 4.6: The 2D scattered light patterns of spherical cytoplasm only (A-A'), elliptical nucleus only (B-B') and elliptical nucleus inside a spherical cytoplasm (C-C').

In Figure 4.6A-A', due to the spherical shape of the cytoplasm, its 2D scattered light patterns in both directions contain vertical straight fringes. In Figure 4.6B-B', due to the non-spherical shape of the nucleus, its 2D scattered light patterns in both directions contains curved fringes. In Figure 4.6C-C', the 2D scattered light patterns from the elliptical nucleus in spherical cytoplasm in general contain curved fringes which follow closely the curved fringes in B-B' but with some “hot spot” like fluctuations. The 2D scattered light patterns of C-C' are dominated by light scattered from the nucleus because the reflective index of nucleus is higher than that of the cytoplasm. The “hot spot” like fluctuations are due to the presence of the spherical cytoplasm which generates vertical straight fringes.

Apart from the fact that nucleus can have shapes other than spherical, the cytoplasm may also have non-spherical shapes. Different shapes of nucleus and cytoplasm can affect the scattered

light generating complex patterns. The simulated 2D scattered light patterns of nucleus and cytoplasm with various combinations of shapes are shown in Figure 4.7.

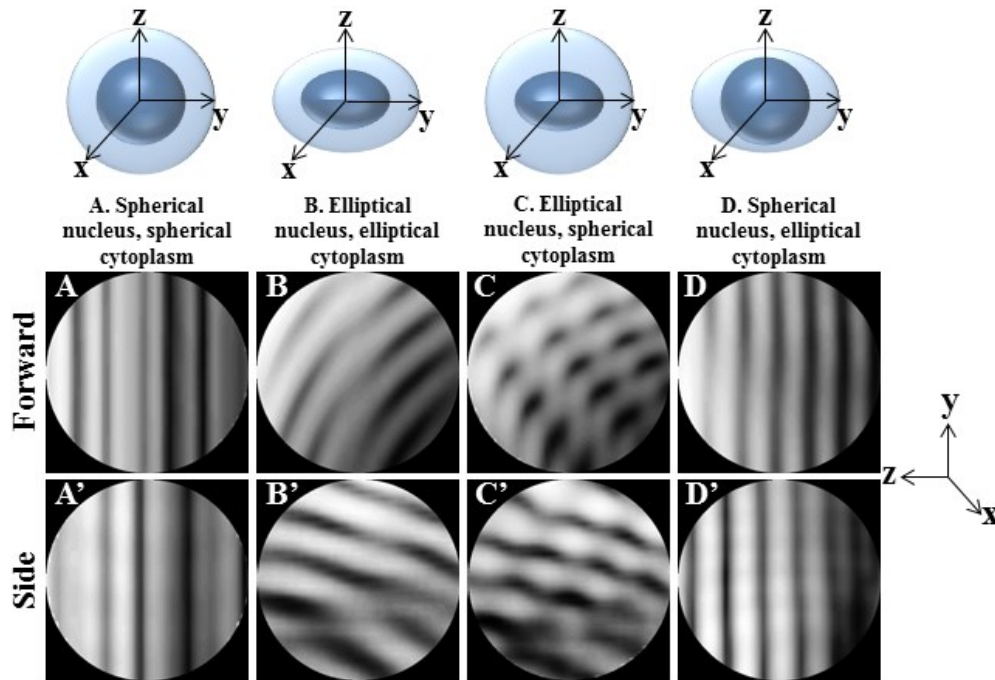


Figure 4.7: Simulated 2D scattered light patterns from systems with nucleus and cytoplasm with various combinations of shapes defined in Table 4.1.

The geometry of nucleus and cytoplasm in each simulation is presented in Table 4.1. In all the simulations, refractive indices of nucleus, cytoplasm, and surrounding medium are assumed to be 1.39, 1.35 and 1.334 respectively.

Table 4.1: Parameters for nucleus and cytoplasm used in the simulations with results presented in Figure 4.7

Numerical model	Cytoplasm ( $\mu\text{m}$ )	Nucleus ( $\mu\text{m}$ )
A	Spherical, $r=5$	Spherical, $r=3$
B	Elliptical, $(r_x, r_y, r_z)=(4,5,4)$	Elliptical, $(r_x, r_y, r_z)=(2,3,2)$
C	Spherical, $r=5$	Elliptical, $(r_x, r_y, r_z)=(2,3,2)$
D	Elliptical, $(r_x, r_y, r_z)=(4,5,4)$	Spherical, $r=3$

In Figure 4.7, the 2D scattered light patterns (A-A') consist of vertical straight fringes because both the nucleus and the cytoplasm are spherical. The information about nucleus and cytoplasm size can be extracted from forward direction pattern using 2D FFT based on pattern's periodicity and dominant frequency values in different directions as discussed before.

The 2D scattered light patterns (B-B') consist of curved fringes with light fluctuations. The 2D scattered light patterns (C-C') consist of curved fringes with fluctuations look like "hot spots". In model "B" both the nucleus and the cytoplasm are spherical and both would generate curved fringes individually. They are more compatible with each other and thus resulted in relatively smoother curved fringes as seen in Figure 4.7B-B'. In model "C" the elliptical nucleus would generate curved fringes while the spherical cytoplasm would generate vertical straight fringes. The curved fringes and the vertical straight fringes are highly contrasted led to resultant curved fringes with "hot spots" like fluctuations as shown in Figure 4.7C-C'. The 2D scattered light patterns (D-D') consist of ~6 straight fringes. In this case the light scattered from the spherical nucleus dominated because of the nucleus's higher refractive index and the numbers of fringes in the patterns are in line with the size of nucleus. Based on the results from these simulations, it can be concluded that nucleus play a crucial role in both forward and side directions in the absence of mitochondria. This information can be used for better understanding of the experimental 2D scattered light patterns from cells to be discussed in later part of this chapter.

### **4.3.Mitochondria**

Mitochondria are the nanometer to micrometer size biological cell internal organelles that due to light diffraction limit, they are not easily observable with traditional microscopy techniques. Mitochondria have an established role to generate energy of the cell. Additionally, it has been

reported that mitochondria play a key role in controlling cell's life and death [64]. It has been studied that during the process of a healthy cell's becoming a malignant cell, the mitochondria's distribution changes in steps [65-67]. A study has reported that defective mitochondrial function is a link to diseases like Parkinson's disease (PD) and Alzheimer's disease (AD) [23]. It has been observed that the defected mitochondria donated by AD and PD patients have abnormal mitochondrial morphology. Clearly, techniques that can obtain information about the states of mitochondria are important for clinical and biological studies. Optical microscopy typically does not provide useful information about mitochondria due to its sub-micron sizes which is normally below the resolution of most optical microscopes. The laser light scattering technique in this thesis can be used to obtain information about the states of mitochondria and our technique is compatible with flow cytometry. In particular, our technique can provide information about the mitochondria's distribution.

The effect of nucleus in generating 2D scattered light patterns in forward and side directions have been discussed. However, those discussed numerical models consisted of nucleus and cytoplasm without the presence of mitochondria. In this section, the mitochondria's effect for 2D scattered light patterns will be discussed and in particularly effect due to changes in the mitochondria's distribution. Mitochondria's effect is more dominant in 2D scattered light patterns in side direction and the effect of 2D light scattered patterns in the side direction due to the changing in the size of mitochondria has been studied by Su et al. [8]. The study concluded that the bigger the size of mitochondria would lead "hot-spot"-like speckles.

### 4.3.1. Mitochondria's distribution

During the process of a healthy cell becoming cancerous and even malignant, the cell mitochondria's distribution changes [65-67]. A healthy cell has dense cluster of mitochondria distributed close to the nucleus of the cell [66]. In a cancerous cell the mitochondria spread out more and the distribution becomes more sparse. When the cell becomes malignant its mitochondria move even further from the nucleus and distribute in a cytoplasm layer close to its membrane [20, 67]. Numerical models presented in this section are based on the above mentioned mitochondria's distribution's changes.

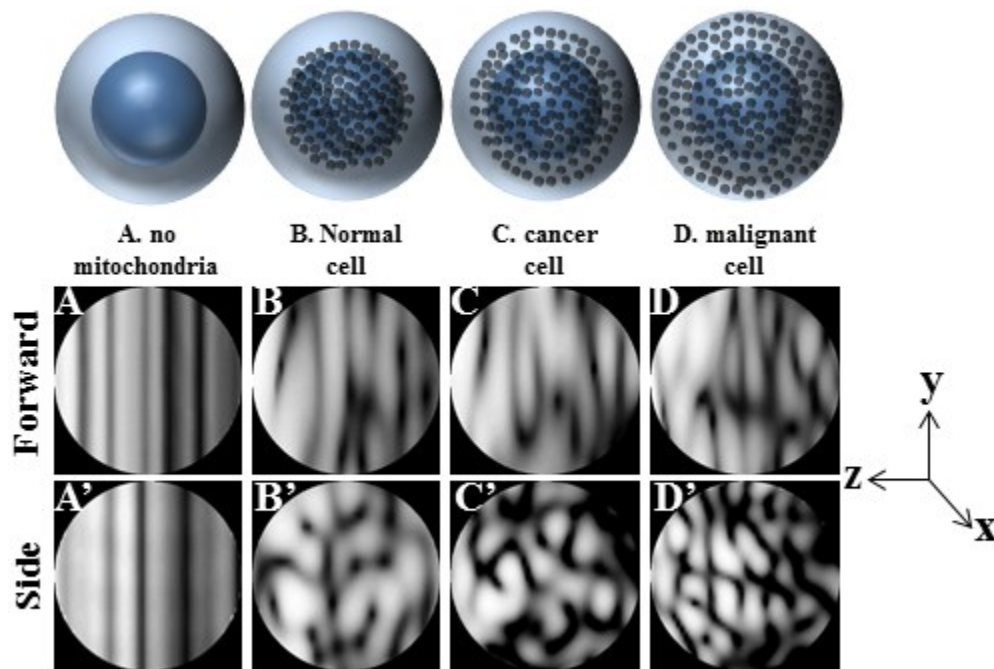


Figure 4.8: The simulated 2D scattered light patterns of due to various mitochondria's distributions.

As shown in Figure 4.8, the mitochondria's distribution changes from numerical model "B" to "D". In all these numerical models, the spherical nucleus has refractive index of 1.39 and cytoplasm has refractive index of 1.35 while the mitochondrion has refractive index of 1.42. Eighty mitochondria each have a radius of 250 nm while the nucleus and cytoplasm have radii of

3  $\mu\text{m}$  and 5  $\mu\text{m}$  respectively. Numerical model "A" (nucleus only) has been presented before and is shown here again for comparison with other models. The 2D scattered light patterns in both forward and side directions of model "A" consist of vertical straight fringes. Going from model "B" to model "D" in Figure 4.8, the mitochondria's distribution changes and the cluster of mitochondria's distribution becomes sparser. Numerical model "B" represents normal cell with mitochondria distributed close to nucleus, eighty spherical mitochondria present a dense cluster distribution close to nucleus in this model. The "hot spots"-like speckles in the 2D scattered light pattern in the side direction are due to the presence of mitochondria [8, 47]. Vertical slightly wiggled fringes can be seen in the 2D scattered light pattern in forward direction, Figure 4.8-B, and speckles in patterns in the side direction, Figure 4.8-B'.

Numerical model "C" represents a cancer cell and its eighty mitochondria are distributed randomly inside the cell. As it can be seen in Figure 4.8-C, the forward scattered light pattern has not changed significantly comparing to Figure 4.8-B and both patterns consists of slightly wiggled vertical lines. The side scattered light pattern in Figure 4.8-C', consists of smaller speckles comparing those in Figure 4.8-B'.

Numerical model "C" represents malignant cell with eighty mitochondria distributed close to cell membrane and far from the nucleus. The simulated 2D scattered light patterns in both forward and side directions are presented in Figure 4.8D-D'. Figure 4.8-D consists of wiggled vertical fringes with some of them are broken lines. The presence of vertical fringes is observable due to nucleus spherical shape while the in-continuity in the fringes is due to the distribution of mitochondria inside the cell and far from the nucleus. The sizes of the speckles in the side

scattered light patterns are decreasing in sizes as the mitochondria's cluster becomes less dense as can be seen from Figure 4.8B'-D'.

The numerical studies presented so far can help us to get a better understanding of the origins of the various structures seen in the 2D scattered light patterns. The summary below will highlight some of the main results that have been achieved from these studies. The structures in the forward scattered light patterns are mainly dictated by the light scattered from the nucleus. The structures are typically vertical straight lines or wiggled straight lines if the nucleus is spherical in shape and the number of fringes typically is related to the size of the nucleus. The structures are typically curved lines if the nucleus is non-spherical in shape. The structures in the forward scattered light patterns can be affected by the presence of the mitochondria and fluctuations in the main structures could produce wiggled lines and even broken lines and the effect of the mitochondria is increasingly larger as the mitochondria are located further away from the nucleus. The structures in the side scattered light patterns are mainly dominated by the light scattered from the mitochondria. The structures are typically speckles and the size of the speckles dependent on mitochondria's cluster density. As the mitochondria's cluster becomes sparse, the sizes of the speckles become smaller.

The ability to capture the 2D scattered light patterns on both forward and side directions simultaneously from the same cell is very useful as it allow us to obtain the information of the cell's nucleus size and shape as well as the mitochondria distribution.

#### **4.4.Light scattering from umbilical cord blood hematopoietic stem cells**

The experimental and simulated 2D scattered light patterns in the forward and side directions from single cells will be presented in this section and the next section. In the experiment, a

sample solution of  $1000 \frac{\text{cells}}{\text{mL}}$  umbilical cord blood hematopoietic stem cells (UCB HSCs) has been diluted from a known source. Five of the simultaneously captured 2D scattered light patterns in forward and side directions are shown in Figure 4.9. Each pair of 2D scattered light patterns of forward and side directions, presented in this figure, originate from one cell's interaction with laser light (in Z direction) as it enters the observation region (see section 3.1.1). As it is illustrated, Figure 4.9A-E show 4 vertical fringes in forward scattered light patterns. Figure 4.9A'-E' show 3-5 large size speckles in side scattered light patterns.

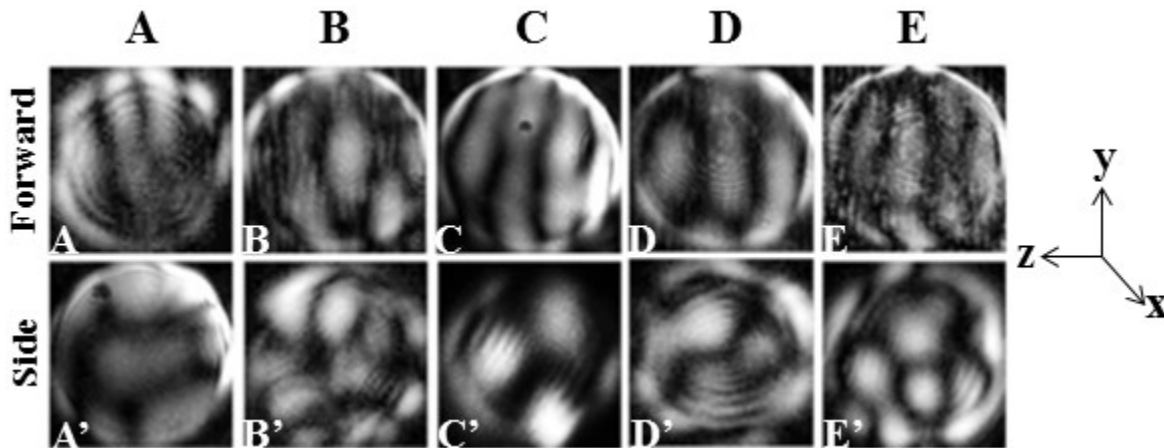
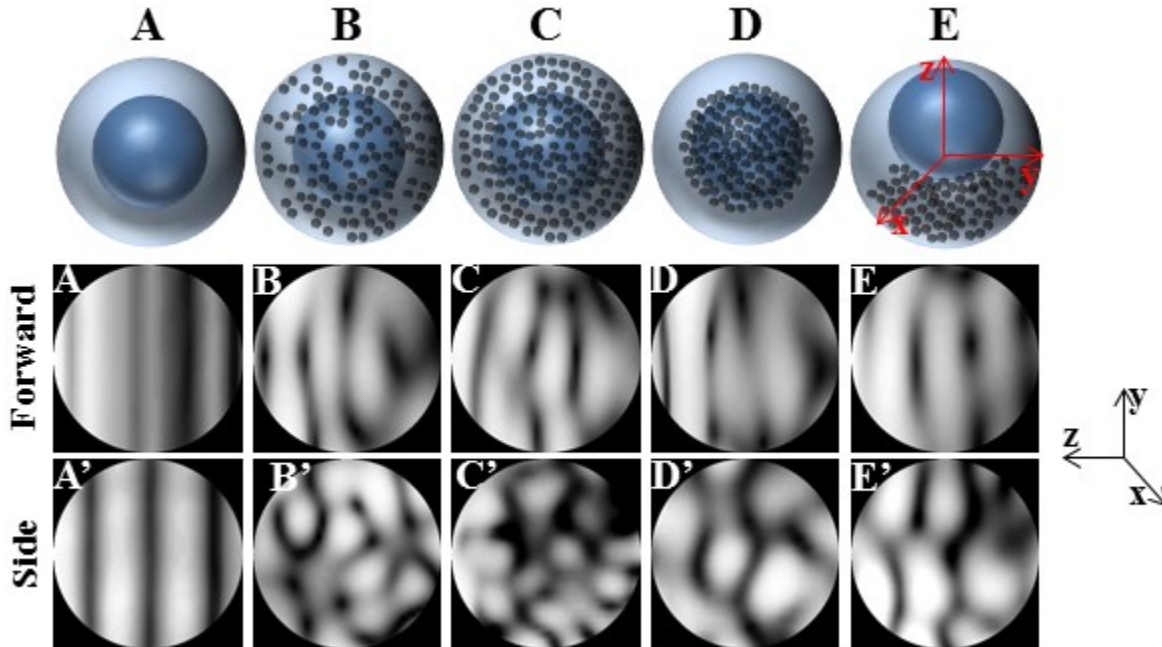


Figure 4.9: Experimental scattered light patterns for UCB HSCs in the forward and side directions.

As discussed already the scattered light patterns in the forward and side directions are mainly due to light scattered from nucleus and mitochondria respectively. The 4 vertical fringes which are mostly straight line-like fringes would indicate that an existence of a mostly spherical nucleus with a radius of  $\sim 2 \mu\text{m}$ . The speckle structures in the 2D scattered light patterns in the side directions (Figure 4.8 A' to E') are consistent with speckle structures in the side 2D scattered light patterns from health UCB  $CD34^+$  cells in the previous study conducted by Su et al.[8]. UCB HSCs may be characterized by the expression of certain hematopoietic antigens,

such as CD34 and CD133 [68]. The antigens used for UCB HSC are CD34, CD59, Thy1/CD90, CD38, CD117 and Lin [69].

To model the experimental 2D scattered light patterns, spherical nucleus and mitochondria with several different distributions inside the cell are used in the FDTD simulations. The simulated 2D scattered light patterns in both forward and side directions are shown in Figure 4.10.



**Figure 4.10:** The simulated 2D scattered light patterns for cell models with spherical nucleus and several different mitochondria distributions.

In the simulations, it is assumed that the nucleus has a radius of  $2\mu\text{m}$  with refractive index of 1.39, the cytoplasm has a radius of  $3.3\mu\text{m}$  with refractive index of 1.35, and eighty mitochondria each has a radius of  $0.25\mu\text{m}$  with a refractive index of 1.42. Model "A" represents a cell with only nucleus and no mitochondria. Models "B" and "C" represent a cancerous cell and a malignant cell with their characteristic mitochondria distributions. Model "B" has its mitochondria sparsely clustered randomly inside the cytoplasm. Model "C" has its mitochondria distributed in a layer of cytoplasm away from the nucleus and close to the membrane. Model "D"

presents a healthy cell with its dense mitochondria's cluster distributed in a thin layer of cytoplasm close to the surface of the nucleus. Model "E" was adapted based from previous study [8] with an aggregated dense mitochondria cluster inside the cytoplasm representing a healthy UCB  $CD34^+$  cell. The stimulated 2D scattered light patterns in the forward direction of models "B" to "F" all consist of 4 similar vertical slightly wiggled fringes and is consistent with the experimental patterns. The stimulated 2D scattered light patterns in the side direction of models "B" to "E" all consist of speckles. The speckles sizes in models "B" and "C" are similar and those in models "D" and "E" are similar. The speckles sizes in models "B" and "C" are smaller than those in models "D" and "E". The experimental 2D scattered light patterns in the side direction also consist of speckles and their sizes are consistent with those in models "D" and "E". Su *et al.* has presented speckle analysis of side scattered 2D light scattered pattern as a function of number of speckles to the size of speckles [8, 9]. Similar speckle analysis of side direction 2D light scattered patterns of numerical model "B", "C", "D" and "E" was compared with side direction 2D light scattered patterns of experimental results in Figure 4.9. The speckle analysis is shown in Figure 4.11. As Figure 4.11 illustrates, the scattered patterns from UCB HSCs have 4 peaks with intensity area of  $1.8 \times 10^4$  pixels in average. This average value is shown in Figure 4.11 with horizontal and vertical bars defining the variation range for all patterns (horizontal bar varies for  $\pm 1$ , vertical bar varies for positive 4000 and negative 5700 pixels). Two red points showing speckle analysis of numerical model "D" and "E" scattered as seen in Figure 4.10D-E. These two points fits inside the range of experimental results speckle's analysis with 4 and 5 number of speckles with average area of  $1.5 \times 10^4$  and  $1.4 \times 10^4$  pixels. Green and blue points are based on speckle analysis of Figure 4.10B-C illustrating numerical models

with mitochondria distribution randomly far from the nucleus and close to cell membrane. The green point is defined by 10 number of peaks with average intensity area of  $1.2 \times 10^4$  while the blue point has 13 number of speckles with average area of  $1 \times 10^4$ . There is a significant difference between the number of speckles and the average area between green and blue points with red and black points. More information about speckle analysis process can be found at Appendix A.3.

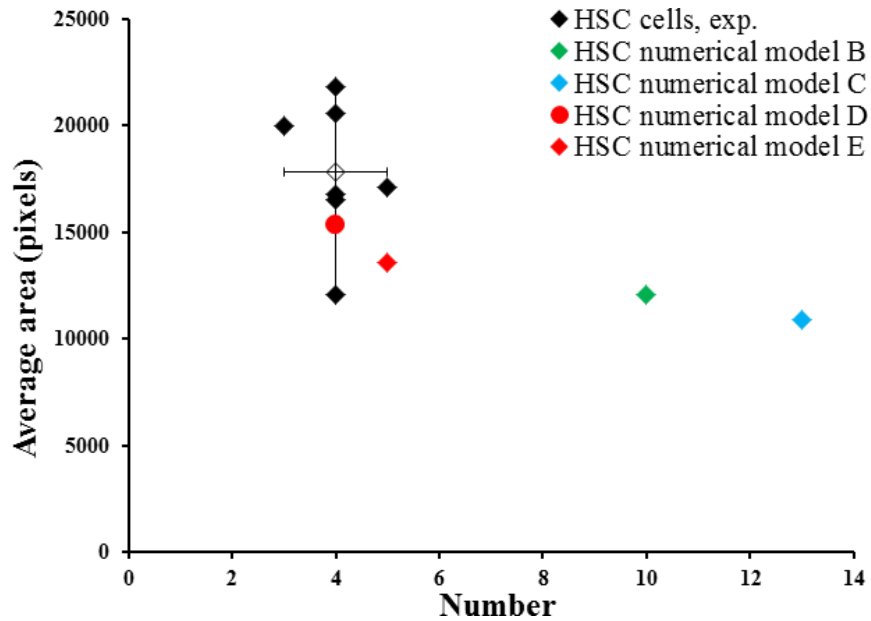


Figure 4.11: The average area ratio over the number of the speckle peaks for UCB HSC's numerical models and experimental results side direction 2D light scattered patterns.

The UCB HSCs in our experiments are consistent with a cell with nucleus with a diameter of  $\sim 4 \mu\text{m}$  and dense mitochondria cluster distributed either around the nucleus or aggregated inside the cell cytoplasm.

#### **4.5.Umbilical cord blood very small embryonic-like stem cells light scattering study**

Development of sorting criteria and better understanding of very small embryonic-like stem cells' (VSEL SC) in particularly their physical properties are important because of the central role that VSELS play in potential clinical applications. The characteristic experimental distributions of scattered light patterns from UCB VSEL stem cells are shown in Figure 4.12. Clearly they are quite distinct from those of UCB HSCs. In contrast to the vertical fringes patterns observed from UCB HSCs in the forward direction, Figure 4.9A-E, the scattered patterns from UCB VSEL stem cells in the forward directions are dominated by non-vertically orientated fringes. There are also differences in the 2D scattered light patterns in the side direction between UCB VSELS and UCB HSCs, Figure 4.9A'-E'. The sizes of the speckles are smaller in case of UCB VSELS in comparison to UCB HSCs. The non-vertical and orientated fringes are due to non-spherical internal/external structures. Examining the experimental 2D scattered light patterns and similar patterns can be grouped into several categories. With the help of the numerical simulations information of the cells in each category can be extracted. It appears that these categories may be related to different growth stages of the UCB VSELS cells.

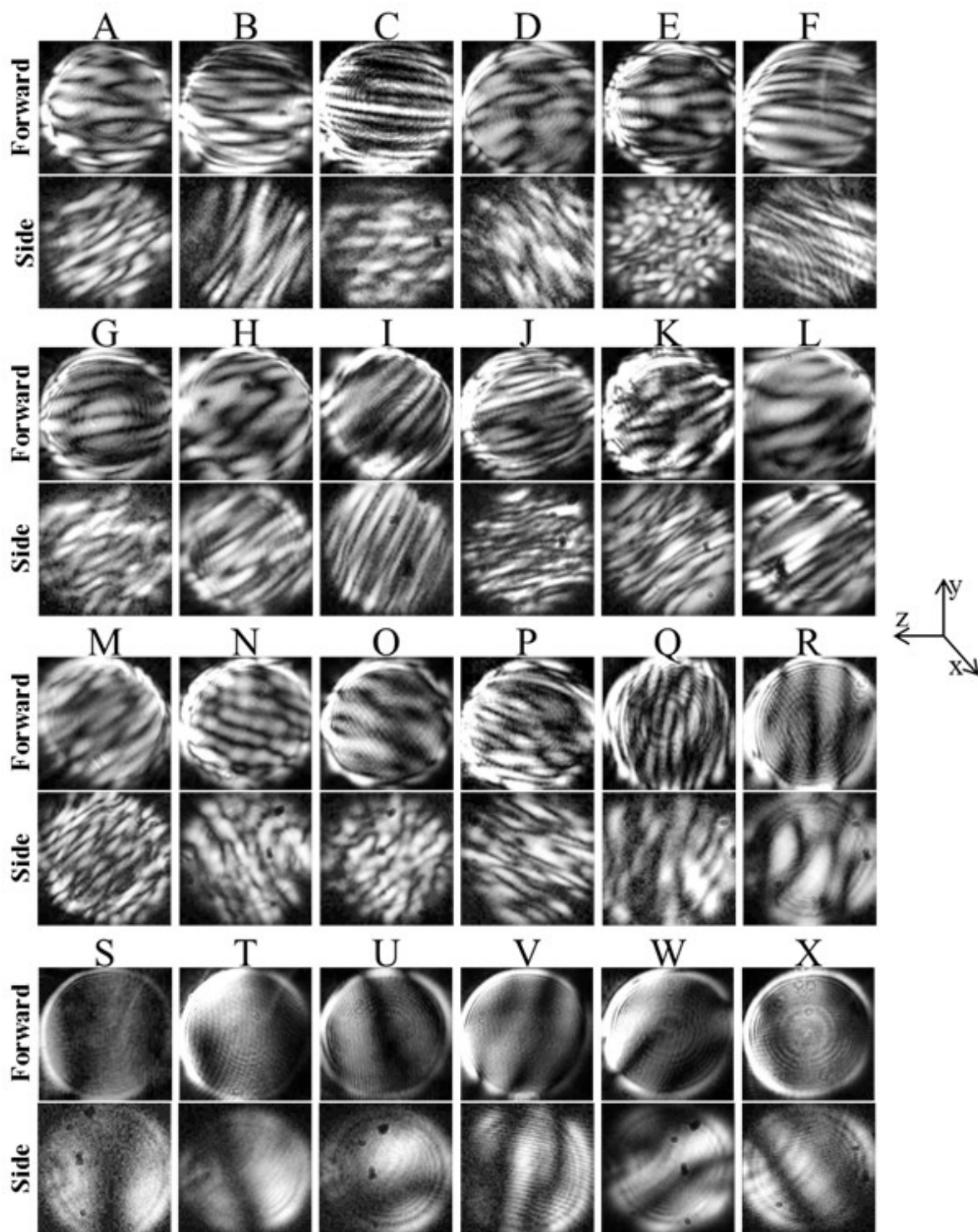
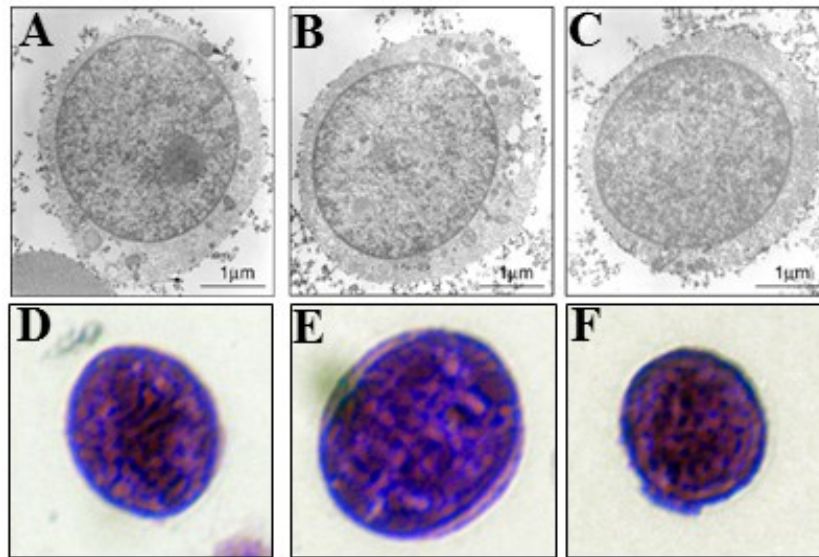


Figure 4.12: Experimental 2D scattered light patterns of UCB VSEL stem cells observed simultaneous in both forward and side directions.

Figure 4.12A-G display 2D scattered light patterns that consist of horizontal fringes in the forward direction while there are small speckle structures in the side directions. Some of these small speckles are periodic in different orientations. Figure 4.12H-R show periodic patterns in non-horizontal orientations in the side and the forward directions and periodic patterns with different orientations in the side directions. The existence of non-spherical structure in the cell is expected to be the reason for these orientations and periodicity. Finally, patterns in Figure 4.12S-X show 1-2 orientated fringes in the forward direction and 1-2 non-horizontal fringes in the side directions. As these patterns are relatively simple when compared to the two previous groups, the cell physical structure is expected to be relatively simple.



**Figure 4.13: Images A-C presents TEM images of CB-derived VSELs. They possess a relatively large nucleus surrounded by a narrow rim of cytoplasm. This narrow rim of cytoplasm possesses a few mitochondria [35]. Non-spherical shape nucleus can be seen in these pictures. D-F pictures show VSEL cells microscope images.**

Recent studies of UCB VSEL stem cells using TEM [35] and microscope images [35, 46] have found that these cells consist of the non-spherical nucleus, Figure 4.13. Additionally, a few mitochondria can be seen in these images [35]. Based on this information and the scattering experimental results, there are several proposed VSEL numerical models that demonstrate

similar patterns to experimental results. As the VSELs change in time [70], their sizes, geometry and morphology can change depending on their different growth stages.

The orientation in pattern's periodicity is expected to come from non-spherical structures in the cell. A numerical model consists of spherical cytoplasm ( $n=1.35$ ) with radius of  $4 \mu\text{m}$ , ellipsoid nucleus ( $n=1.39$ ) with radii's sizes of  $(r_x, r_y, r_z) = (1 \mu\text{m}, 4 \mu\text{m}, 1 \mu\text{m})$  and 20 randomly distributed mitochondria of  $500 \text{ nm}$  diameter ( $n=1.42$ ) were simulated. The laser light propagates along the  $Z$ -axis. Results are as shown in Figure 4.14A-C for this numerical model in three different orientations. As it can be seen, the pattern's periodic direction in forward and side directions are due to ellipsoid nucleus while the generated small size speckles in the side direction are not only due to existence of mitochondria but also due to interference of patterns from ellipsoid nucleus and spherical cytoplasm. This numerical model represents a cell with spherical geometry of  $8 \mu\text{m}$  and internal elliptical shape nucleus of size  $8 \times 2 \mu\text{m}$ .

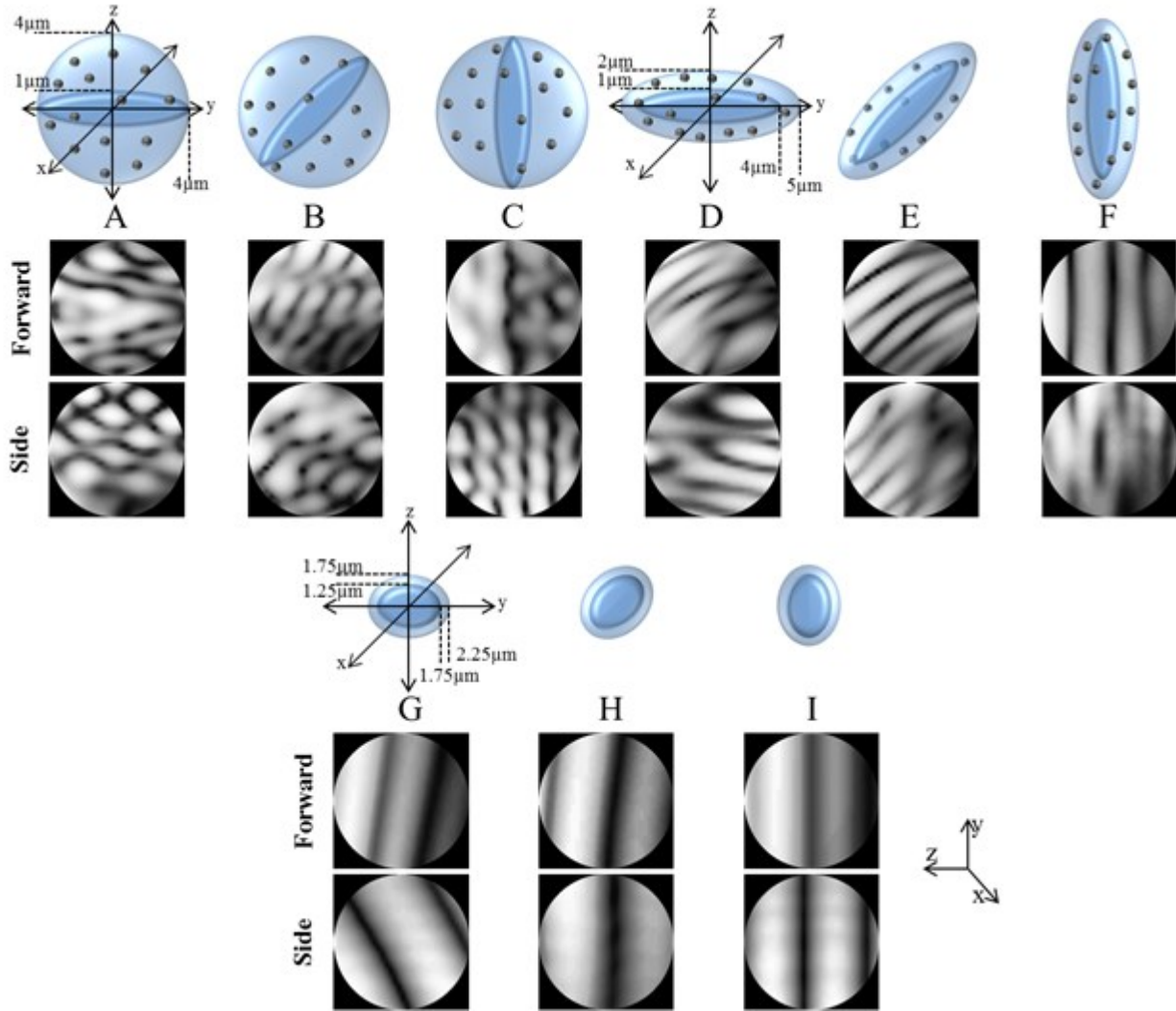


**Figure 4.14: Numerical models used for UCB VSEL simulations. These models consist of spherical/ellipsoid shape nucleus/cytoplasm and some small mitochondria placed in thin rim of nucleus and cytoplasm. Forward and side directions patterns are shown.**

VSEL's experimental results Figure 4.12A-G, have similarities with simulated scattered patterns from first proposed model, Figure 4.14A-C. Based on numerical model's generated patterns and their similarities with experimental results, it speculates that these scattered patterns belong to bigger cells available inside the cell sample in our experiment.

The second numerical model consists of two concentric ellipsoid geometry cytoplasm ( $n = 1.35$ ) with radii's sizes of  $(r_x, r_y, r_z) = (2 \mu\text{m}, 5 \mu\text{m}, 2 \mu\text{m})$  and nucleus ( $n = 1.39$ ) with radii of

$(r_x, r_y, r_z) = (1 \mu\text{m}, 4 \mu\text{m}, 1 \mu\text{m})$  shown in Figure 4.14D-F. Similar to the previous model, there are 20 randomly distributed 500 nm diameter mitochondria inside the cell. The results are shown in Figure 4.14 for this numerical model's different rotation with respect to laser light direction along the Z-axis. As it can be observed, the ellipsoid geometry of this numerical model affects the fringes' orientation and as the model rotates, it changes the fringes' orientations differently. The existence of mitochondria affects the pattern as it generates non-continuous fringes similar to the side direction experimental results Figure 4.12A-R. This numerical model represents a big elliptical shape cell of  $10 \times 4 \mu\text{m}$  with internal elliptical shape nucleus.

The last proposed numerical model is made of two small size concentric ellipsoid geometry nucleus and cytoplasm. The cytoplasm has radii's sizes of  $(r_x, r_y, r_z) = (1.75 \mu\text{m}, 2.25 \mu\text{m}, 1.75 \mu\text{m})$  and nucleus has radii's sizes of  $(r_x, r_y, r_z) = (1.25 \mu\text{m}, 1.75 \mu\text{m}, 1.25 \mu\text{m})$  shown in Figure 4.14. There are no mitochondria in this model as this model since the nucleus has occupied most of the inside volume and leave limited space for mitochondria. The simulated patterns can be found in Figure 4.14G-I. Ellipsoid geometry orients the fringes while model's different rotations will result in fringes different orientations. This numerical model has similarities with the experimental results shown in Figure 4.12S-X. Based on this model's numerical results, it speculates the cells with such scattering patterns are in very early stages of growth and much smaller ( $<5 \mu\text{m}$  diameter) than the other cells in the sample.

The proposed model's results are similar to experimental patterns from UCB VSEL stem cells. As the non-spherical shape nucleus/cytoplasm orient fringes, the small structure speckles can be simulated as the effect of mitochondria existence or spherical shape cytoplasm. The orientation of fringes is related to the rotation of non-spherical nucleus/cytoplasm.

The UCB VSEL stem cells in the sample are expected to be in various stages of growth. Based on the above analysis, the experimental scattered light patterns shown in Figure 4.10 S-X could come from cells in the sample with relatively smaller size ( $<5 \mu\text{m}$  in diameter) with a relatively simple structure which are characteristics of VSEL stem cells in the early stages, while the rest of the experimental patterns could come from relatively larger cells ( $8\text{-}10 \mu\text{m}$  in diameter) with more complex structures characteristics of those VSEL stem cells in more mature stages of growth.

All the numerical models proposed in this thesis are assumed that the experimental 2D scattered light patterns come from a single cell. The effect of the presence of the multiple cells has been studied by Liu *et al.*[71]

## 5. Conclusions

### 5.1. Summary

This thesis reported the numerical and experimental studies of the 2D scattered light patterns from a single latex beads and single cell in forward and side directions. The 2D scattered light pattern technique is a label free technique for cell identification and characterization that could be implemented in flow cytometry replacing the current fluorescence biomarker labeling technique. In this thesis a major step forward has been made in the experimental design for the 2D scattered light pattern measurements demonstrating data can be obtained in the forward and side directions simultaneously. The effects of cell's dominant internal components, nucleus, cytoplasm and mitochondria on the 2D scattered light patterns have been examined using numerical simulations. The nucleus has a dominant effect on 2D scattered light patterns in the forward direction while the mitochondria mainly affect the 2D scattered light patterns in the side direction. The number of fringes in the forward 2D scattered light pattern is dependent on the size of the nucleus. Vertical straight and non-vertical curved fringes in 2D scattered light pattern are due to a nucleus with a spherical shape and a nucleus with non-spherical shape respectively. The size of the speckles presented in the side 2D scattered light patterns dependent on the mitochondria's cluster density and distributions. The experimental 2D scattered light patterns for UCB HSC and UCB VSEL SC have been obtained. There are significant differences between the patterns from these two types of stem cells. Numerical cell models representing a HSC have been developed. There are good agreements between the simulated 2D scattered light patterns using two of the numerical HSC models and those observed experimentally. The experimental

2D scattered light patterns for UCB VSEL SC can be categorized in 3 groups. Group one has non-vertical and non-continuous fringes in the forward scattered light patterns and small size speckle in the side scattered light patterns. Group two has non-vertical and non-continuous fringes in both forward and side scattered light patterns. Group three has straight fringes oriented in various directions in both forward and side scattered light patterns. The proposed numerical cell model for group one consists of an elliptical shape nucleus and spherical cytoplasm with some mitochondria distributed randomly. The proposed numerical cell model for group two consists of elliptical shape nucleus and cytoplasm with randomly distributed mitochondria. The proposed numerical cell model for group three consists of a small size cell with non-spherical shape nucleus and cytoplasm and no mitochondria. There are good agreements between the simulated 2D scattered light patterns using these numerical models and the respected patterns observed experimentally. The numerical cell model for group 3 represent small and simple cells which could be VSEL SCs at an early growth stage while the numerical cell models for group 1 and 2 of represent larger and more complex cells which could be VSEL SCs at later growth stages.

## **5.2.Future work**

To further improve the 2D scattered light pattern technique for label-free cytometry a number of further studies are recommended below:

- Additional improvement of experimental setup allowing the number of photons in the 2D scattered light patterns to be obtained.

- Additional improvement of experimental setup allowing the 2D scattered light patterns to be obtained in wide angular range and in more directions in addition to forward and side.
- Demonstrating the technique can be useful for other applications. Currently, the technique is being used for determining the mechanisms for causing death of the human SH-SY5Y neuroblastoma cells. Labeling is suspected to be the main cause.
- Finding 2D scattered light patterns for a wider range of cells to establish a database. This database can be used for cell identification and sorting.
- Implementing the technique in a microfluidic sorting system or a conventional flow cytometer. The technique can be implemented in a conventional flow cytometer turning it into a label-free cytometer. Such a multi-angle label-free cytometer based on the results in this thesis is shown in Figure 5.1. In Figure 5.1, a narrow stream of cell line is produced using the hydrodynamic focusing technique. The droplets each consists of a single cell enter the laser beam probing region. Two lenses in the forward and side directions are used to collect the scattered light into the CCD cameras obtaining the 2D scattered light patterns of the cell. The patterns are analyzed and comparing with a database containing 2D scattered pattern of various cells to identify the cell type and making sorting decision.

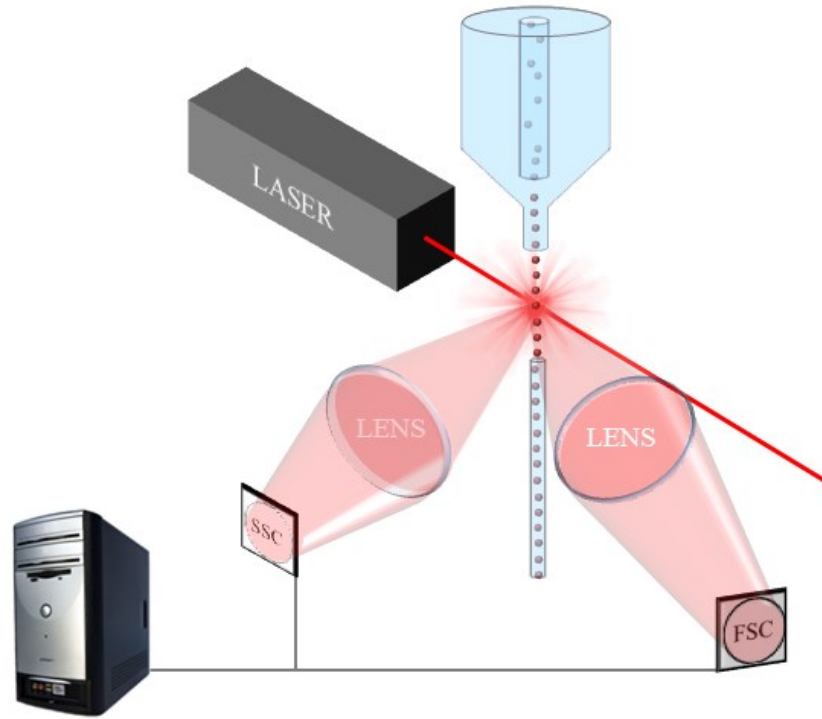


**Figure 5.1:** This figure shows a prototype of identification part of multi-angle label-free cytometer machine (FSC=Forward Scattered Camera, SSC=Side Scattered Camera)

## References

- [1] E. K. Zuba-Surma, I. Klich, N. Greco, M. J. Laughlin, J. Ratajczak, and M. Z. Ratajczak, "Optimization of isolation and further characterization of umbilical cord blood-derived very small embryonic/epiblast-like stem cells (VSELs)," *European journal of haematology*, vol. 84, pp. 34-46, 2010.
- [2] M. Z. Ratajczak, M. Kucia, J. Ratajczak, and E. K. Zuba-Surma, "A multi-instrumental approach to identify and purify very small embryonic like stem cells (VSELs) from adult tissues," *Micron*, vol. 40, pp. 386-393, 2009.
- [3] M. Ratajczak, M. Kucia, and J. Ratajczak, "Very small embryonic-like (vsel) stem cells and methods of isolating and using the same," ed: Google Patents, 2006.
- [4] D. Bhartiya, A. Shaikh, P. Nagvenkar, S. Kasiviswanathan, P. Pethe, H. Pawani, *et al.*, "Very small embryonic-like stem cells with maximum regenerative potential get discarded during cord blood banking and bone marrow processing for autologous stem cell therapy," *Stem cells and development*, vol. 21, pp. 1-6, 2011.
- [5] J. R. Mourant, J. P. Freyer, A. H. Hielscher, A. A. Eick, D. Shen, and T. M. Johnson, "Mechanisms of light scattering from biological cells relevant to noninvasive optical-tissue diagnostics," *Applied Optics*, vol. 37, pp. 3586-3593, 1998.
- [6] A. Dunn and R. Richards-Kortum, "Three-dimensional computation of light scattering from cells," *Selected Topics in Quantum Electronics, IEEE Journal of*, vol. 2, pp. 898-905, 1996.
- [7] R. Drezek, A. Dunn, and R. Richards-Kortum, "Light scattering from cells: finite-difference time-domain simulations and goniometric measurements," *Applied Optics*, vol. 38, pp. 3651-3661, 1999.
- [8] X. Su, Y. Qiu, L. Marquez-Curtis, M. Gupta, C. E. Capjack, W. Rozmus, *et al.*, "Label-free and noninvasive optical detection of the distribution of nanometer-size mitochondria in single cells," *Journal of biomedical optics*, vol. 16, pp. 067003-067003-7, 2011.
- [9] X. Su, S. E. Kirkwood, M. Gupta, L. Marquez-Curtis, Y. Qiu, A. Janowska-Wieczorek, *et al.*, "Microscope-based label-free microfluidic cytometry," *Optics express*, vol. 19, pp. 387-398, 2011.
- [10] X.-T. Su, K. Singh, C. Capjack, J. Petráček, C. Backhouse, and W. Rozmus, "Measurements of light scattering in an integrated microfluidic waveguide cytometer," *Journal of biomedical optics*, vol. 13, pp. 024024-024024-10, 2008.
- [11] L. Perelman, V. Backman, M. Wallace, G. Zonios, R. Manoharan, A. Nusrat, *et al.*, "Observation of periodic fine structure in reflectance from biological tissue: a new technique for measuring nuclear size distribution," *Physical Review Letters*, vol. 80, p. 627, 1998.

- [12] J. R. Mourant, I. J. Bigio, J. Boyer, R. L. Conn, T. Johnson, and T. Shimada, "Spectroscopic diagnosis of bladder cancer with elastic light scattering," *Lasers in surgery and medicine*, vol. 17, pp. 350-357, 1995.
- [13] J. R. Mourant, I. J. Bigio, J. D. Boyer, T. M. Johnson, J. Lacey, A. G. Bohorfoush III, *et al.*, "Elastic scattering spectroscopy as a diagnostic tool for differentiating pathologies in the gastrointestinal tract: preliminary testing," *Journal of Biomedical Optics*, vol. 1, pp. 192-199, 1996.
- [14] J. B. Fishkin, O. Coquoz, E. R. Anderson, M. Brenner, and B. J. Tromberg, "Frequency-domain photon migration measurements of normal and malignant tissue optical properties in a human subject," *Applied Optics*, vol. 36, pp. 10-20, 1997.
- [15] G. J. Tearney, M. E. Brezinski, B. E. Bouma, S. A. Boppart, C. Pitris, J. F. Southern, *et al.*, "In vivo endoscopic optical biopsy with optical coherence tomography," *Science*, vol. 276, pp. 2037-2039, 1997.
- [16] A. Wax, C. Yang, V. Backman, K. Badizadegan, C. W. Boone, R. R. Dasari, *et al.*, "Cellular organization and substructure measured using angle-resolved low-coherence interferometry," *Biophysical journal*, vol. 82, pp. 2256-2264, 2002.
- [17] R. S. Gurjar, V. Backman, L. T. Perelman, I. Georgakoudi, K. Badizadegan, I. Itzkan, *et al.*, "Imaging human epithelial properties with polarized light-scattering spectroscopy," *Nature Medicine*, vol. 7, pp. 1245-1248, 2001.
- [18] V. Backman, V. Gopal, M. Kalashnikov, K. Badizadegan, R. Gurjar, A. Wax, *et al.*, "Measuring cellular structure at submicrometer scale with light scattering spectroscopy," *Selected Topics in Quantum Electronics, IEEE Journal of*, vol. 7, pp. 887-893, 2001.
- [19] J. R. Mourant, M. Canpolat, C. Brocker, O. Espondo-Ramos, T. M. Johnson, A. Matanock, *et al.*, "Light scattering from cells: the contribution of the nucleus and the effects of proliferative status," in *BiOS 2000 The International Symposium on Biomedical Optics*, 2000, pp. 33-42.
- [20] C. Liu, C. Capjack, and W. Rozmus, "3-D simulation of light scattering from biological cells and cell differentiation," *Journal of biomedical optics*, vol. 10, pp. 014007-01400712, 2005.
- [21] G. Cooper and R. Hausman, "The Cell-A Molecular Approach," *Sunderland (MA): Sinauer Associates, Inc*, 2000.
- [22] R. Drezek, M. Guillaud, T. Collier, I. Boiko, A. Malpica, C. Macaulay, *et al.*, "Light scattering from cervical cells throughout neoplastic progression: influence of nuclear morphology, DNA content, and chromatin texture," *Journal of biomedical optics*, vol. 8, pp. 7-16, 2003.
- [23] P. A. Trimmer, R. H. Swerdlow, J. K. Parks, P. Keeney, J. P. Bennett, S. W. Miller, *et al.*, "Abnormal mitochondrial morphology in sporadic Parkinson's and

- Alzheimer's disease cybrid cell lines," *Experimental neurology*, vol. 162, pp. 37-50, 2000.
- [24] H. Liu, B. Beauvoit, M. Kimura, and B. Chance, "Dependence of tissue optical properties on solute-induced changes in refractive index and osmolarity," *Journal of Biomedical Optics*, vol. 1, pp. 200-211, 1996.
- [25] J. Beuthan, O. Minet, J. Helfmann, M. Herrig, and G. Müller, "The spatial variation of the refractive index in biological cells," *Physics in medicine and biology*, vol. 41, p. 369, 1996.
- [26] A. Brunsting and P. F. Mullaney, "Differential light scattering from spherical mammalian cells," *Biophysical journal*, vol. 14, pp. 439-453, 1974.
- [27] B. Alberts, D. Bray, and J. Lewis, "Molecular Biology of the Cell," *Garland Science, New York*, p. 507, 1994.
- [28] P. H. O'Farrell, J. Stumpff, and T. T. Su, "Embryonic cleavage cycles: how is a mouse like a fly?," *Current Biology*, vol. 14, pp. R35-R45, 2004.
- [29] J. Hipp and A. Atala, "Sources of stem cells for regenerative medicine," *Stem Cell Reviews*, vol. 4, pp. 3-11, 2008.
- [30] S. Leedham, M. Brittan, S. McDonald, and N. Wright, "Intestinal stem cells," *Journal of cellular and molecular medicine*, vol. 9, pp. 11-24, 2005.
- [31] H. Ali and F. Al-Mulla, "Defining umbilical cord blood stem cells," 2012.
- [32] S. Knudtzon, "In vitro growth of granulocytic colonies from circulating cells in human cord blood," *Blood*, vol. 43, pp. 357-361, 1974.
- [33] H. Vaziri, W. Dragowska, R. C. Allsopp, T. E. Thomas, C. B. Harley, and P. M. Lansdorp, "Evidence for a mitotic clock in human hematopoietic stem cells: loss of telomeric DNA with age," *Proceedings of the National Academy of Sciences*, vol. 91, pp. 9857-9860, 1994.
- [34] M. Z. Ratajczak, *Adult stem cell therapies: alternatives to plasticity*: Springer, 2014.
- [35] M. Kucia, M. Halasa, M. Wysoczynski, M. Baskiewicz-Masiuk, S. Moldenhawer, E. Zuba-Surma, *et al.*, "Morphological and molecular characterization of novel population of CXCR4<sup>+</sup>; SSEA-4<sup>+</sup>; Oct-4<sup>+</sup>; very small embryonic-like cells purified from human cord blood—preliminary report," *Leukemia*, vol. 21, pp. 297-303, 2007.
- [36] C. McGuckin, N. Forraz, M. O. Baradez, S. Navran, J. Zhao, R. Urban, *et al.*, "Production of stem cells with embryonic characteristics from human umbilical cord blood," *Cell proliferation*, vol. 38, pp. 245-255, 2005.
- [37] M. C. Yoder, L. E. Mead, D. Prater, T. R. Krier, K. N. Mroueh, F. Li, *et al.*, "Redefining endothelial progenitor cells via clonal analysis and hematopoietic stem/progenitor cell principals," *Blood*, vol. 109, pp. 1801-1809, 2007.
- [38] J. Case, L. E. Mead, W. K. Bessler, D. Prater, H. A. White, M. R. Saadatzaheh, *et al.*, "Human CD34<sup>+</sup> AC133<sup>+</sup> VEGFR-2<sup>+</sup> cells are not endothelial progenitor cells

- but distinct, primitive hematopoietic progenitors," *Experimental hematology*, vol. 35, pp. 1109-1118, 2007.
- [39] A. Habich, M. Jurga, I. Markiewicz, B. Lukomska, U. Bany-Laszewicz, and K. Domanska-Janik, "Early appearance of stem/progenitor cells with neural-like characteristics in human cord blood mononuclear fraction cultured in vitro," *Experimental hematology*, vol. 34, pp. 914-925, 2006.
- [40] L. Bużańska, E. Machaj, B. Zabłocka, Z. Pojda, and K. Domańska-Janik, "Human cord blood-derived cells attain neuronal and glial features in vitro," *Journal of cell science*, vol. 115, pp. 2131-2138, 2002.
- [41] G. Kögler, S. Sensken, J. A. Airey, T. Trapp, M. Müschen, N. Feldhahn, *et al.*, "A new human somatic stem cell from placental cord blood with intrinsic pluripotent differentiation potential," *The Journal of experimental medicine*, vol. 200, pp. 123-135, 2004.
- [42] O. K. Lee, T. K. Kuo, W.-M. Chen, K.-D. Lee, S.-L. Hsieh, and T.-H. Chen, "Isolation of multipotent mesenchymal stem cells from umbilical cord blood," *Blood*, vol. 103, pp. 1669-1675, 2004.
- [43] L. Hou, H. Cao, D. Wang, G. Wei, C. Bai, Y. Zhang, *et al.*, "Induction of umbilical cord blood mesenchymal stem cells into neuron-like cells in vitro," *International journal of hematology*, vol. 78, pp. 256-261, 2003.
- [44] M. W. Lee, Y. J. Moon, M. S. Yang, S. K. Kim, I. K. Jang, Y.-w. Eom, *et al.*, "Neural differentiation of novel multipotent progenitor cells from cryopreserved human umbilical cord blood," *Biochemical and biophysical research communications*, vol. 358, pp. 637-643, 2007.
- [45] M. Kucia, W. Wojakowski, R. Reza, B. Machalinski, J. Gozdzik, M. Majka, *et al.*, "The migration of bone marrow-derived non-hematopoietic tissue-committed stem cells is regulated in an SDF-1-, HGF-, and LIF-dependent manner," *Archivum immunologiae et therapiae experimentalis*, vol. 54, pp. 121-135, 2006.
- [46] R. Danova-Alt, A. Heider, D. Egger, M. Cross, and R. Alt, "Very small embryonic-like stem cells purified from umbilical cord blood lack stem cell characteristics," *PloS One*, vol. 7, p. e34899, 2012.
- [47] L. Zhang, Y. Qin, K.-X. Li, X. Zhao, Y.-F. Xing, H. Zhao, *et al.*, "Light scattering properties in spatial planes for label free cells with different internal structures," *Optical and Quantum Electronics*, vol. 47, pp. 1005-1025, 2015.
- [48] D. Watson, N. Hagen, J. Diver, P. Marchand, and M. Chachisvilis, "Elastic light scattering from single cells: orientational dynamics in optical trap," *Biophysical journal*, vol. 87, pp. 1298-1306, 2004.
- [49] A. Taflove and S. C. Hagness, "Computational electrodynamics: the finite-difference time-domain method," *Norwood, 2nd Edition, MA: Artech House, 1995, 1995.*

- [50] G. F. Crosta, Y.-L. Pan, K. B. Aptowicz, C. Casati, R. G. Pinnick, R. K. Chang, *et al.*, "Automated classification of single airborne particles from two-dimensional angle-resolved optical scattering (TAOS) patterns by non-linear filtering," *Journal of Quantitative Spectroscopy and Radiative Transfer*, vol. 131, pp. 215-233, 2013.
- [51] K. B. Aptowicz, Y.-L. Pan, S. D. Martin, E. Fernandez, R. K. Chang, and R. G. Pinnick, "Decomposition of atmospheric aerosol phase function by particle size and asphericity from measurements of single particle optical scattering patterns," *Journal of Quantitative Spectroscopy and Radiative Transfer*, vol. 131, pp. 13-23, 2013.
- [52] H. M. Shapiro, *Practical flow cytometry*: John Wiley & Sons, 2005.
- [53] W. T. Grandy Jr and W. T. Grandy, *Scattering of waves from large spheres*: Cambridge University Press, 2005.
- [54] C. F. Bohren and D. R. Huffman, "Absorption and scattering by a sphere," *Absorption and Scattering of Light by Small Particles*, pp. 82-129, 1983.
- [55] X.-T. Su, "Light Scattering in an Integrated Microfluidic Waveguide Cytometer," PhD, University of Alberta, Edmonton, AB, 2008.
- [56] H. C. Hulst and H. Van De Hulst, *Light scattering by small particles*: Courier Corporation, 1957.
- [57] P. Laven. (2015). *Mieplot v.1.45*. Available: <http://www.philiplaven.com/mieplot.htm>
- [58] J. Q. Lu, P. Yang, and X.-H. Hu, "Simulations of light scattering from a biconcave red blood cell using the finite-difference time-domain method," *Journal of Biomedical Optics*, vol. 10, pp. 024022-02402210, 2005.
- [59] R. L. Schoch, L. E. Kapinos, and R. Y. Lim, "Nuclear transport receptor binding avidity triggers a self-healing collapse transition in FG-nucleoporin molecular brushes," *Proceedings of the National Academy of Sciences*, vol. 109, pp. 16911-16916, 2012.
- [60] M. Z. Islam, X. Su, S. E. Kirkwood, K. Singh, J. N. McMullin, W. Rozmus, *et al.*, "Development of an optomicrofluidic flow cytometer for the sorting of stem cells from blood samples," in *Photonics North 2009*, 2009, pp. 73860C-73860C-8.
- [61] X. Ma, J. Q. Lu, R. S. Brock, K. M. Jacobs, P. Yang, and X.-H. Hu, "Determination of complex refractive index of polystyrene microspheres from 370 to 1610 nm," *Physics in medicine and biology*, vol. 48, p. 4165, 2003.
- [62] O. Zhernovaya, O. Sydoruk, V. Tuchin, and A. Douplik, "The refractive index of human hemoglobin in the visible range," *Physics in medicine and biology*, vol. 56, p. 4013, 2011.
- [63] C. Sewry, S. Brown, E. Mercuri, G. Bonne, L. Feng, G. Camici, *et al.*, "Skeletal muscle pathology in autosomal dominant Emery-Dreifuss muscular dystrophy with lamin A/C mutations," *Neuropathology and applied neurobiology*, vol. 27, pp. 281-290, 2001.

- [64] S. Desagher and J.-C. Martinou, "Mitochondria as the central control point of apoptosis," *Trends in cell biology*, vol. 10, pp. 369-377, 2000.
- [65] L. Liu, A. Vo, G. Liu, and W. L. McKeehan, "Distinct structural domains within C19ORF5 support association with stabilized microtubules and mitochondrial aggregation and genome destruction," *Cancer research*, vol. 65, pp. 4191-4201, 2005.
- [66] P. L. Gourley, J. K. Hendricks, A. E. McDonald, R. G. Copeland, K. E. Barrett, C. R. Gourley, *et al.*, "Ultrafast nanolaser flow device for detecting cancer in single cells," *Biomedical microdevices*, vol. 7, pp. 331-339, 2005.
- [67] W. D. Thomas, X. D. Zhang, A. V. Franco, T. Nguyen, and P. Hersey, "TNF-related apoptosis-inducing ligand-induced apoptosis of melanoma is associated with changes in mitochondrial membrane potential and perinuclear clustering of mitochondria," *The Journal of Immunology*, vol. 165, pp. 5612-5620, 2000.
- [68] H. Mayani and P. M. Lansdorp, "Biology of human umbilical cord blood-derived hematopoietic stem/progenitor cells," *Stem Cells*, vol. 16, pp. 153-165, 1998.
- [69] Y. Sonoda, "Immunophenotype and functional characteristics of human primitive CD34-negative hematopoietic stem cells: the significance of the intra-bone marrow injection," *Journal of autoimmunity*, vol. 30, pp. 136-144, 2008.
- [70] M. Kucia, R. Reca, V. Jala, B. Dawn, J. Ratajczak, and M. Ratajczak, "Bone marrow as a home of heterogenous populations of nonhematopoietic stem cells," *Leukemia*, vol. 19, pp. 1118-1127, 2005.
- [71] S. Liu, L. Xie, Y. Yang, X. Qiao, K. Song, B. Kong, *et al.*, "Label-free analysis of single and multiple cells with a 2D light scattering static cytometer," in *SPIE BiOS*, 2015, pp. 93281B-93281B-5.

# Appendices

## A.1. AETHER code compilations and code run

This section discusses in details the mechanics of compiling, running and outputting the results from AETHER codes.

### A.1.1. Compiling and running AETHER codes

AETHER is a Maxwell equations solver written in FORTRAN language. To use this code, a computer with sufficient memory is needed. For our calculations, we used Westgrid clusters. Different free license softwares such as PuTTY and WinSCP can be used to connect to the clusters and control the home directory for further uses. AETHER codes, involve of six “\*.f90” format file, 2 input file and .pbs file, are transformed to the designated folder in Westgrid cluster (Hungabee, Bugaboo, Jasper and more). “\*.f90” format files are working as functions designated for different part of calculations. Each function generated results can be stored and transformed for other functions use. These functions are listed as follows:

- 1) AETHERCELL\_core.f90
- 2) AETHERCELLL\_const.f90
- 3) AETHERCELLL\_main.f90
- 4) AETHERCELLL\_far.f90
- 5) AETHERCELLL\_resub.f90
- 6) AETHERCELLL\_inci.f90

Function 1 calculates electric and magnetic fields using Yee algorithm. Function 2 captures input data from input files and define internal parameters. Function 3 is a link between all other

functions and controls the whole process. Function 4 calculates the far-field values of calculated data in nearfield. Function 5 is designated to control and save the process in case the user wants to halt to resume the calculations. Function 6 is used to calculate the incident light values on total-field/scattered-field interface. There are two other input files to define the medium, size and location of cell cytoplasm, nucleus and mitochondria that provide information for function 1. Additionally information about laser wavelength, polarization and other information are also stored in these two files. `*.pbs` file is a file where the information needed for cluster is stored. This file calls `“job file”` and provide information of needed memory, number of nodes, job name and others for cluster. Cluster uses this file to track the process and locate the needed files during the calculations and retaining results back. It is recommended to discuss with Westgrid support team to prepare a good `“*.pbs”` file for future use of code.

Depending on the cluster’s specifications, special FORTRAN compiler should be installed and started. `“ifort”` was used to compile codes. Compiling mentioned functions are done using below Linux command:

```
ifort -O2 -openmp ihesam AETHERCELL_const.f90 AETHERCELL_far.f90 AETHERCELL_core.f90  
AETHERCELL_inci.f90 AETHERCELL_resub.f90 AETHERCELL_main.f90
```

This command line will compile the codes and translated data will be stored in `“ihesam”`. Next, `“ihesam”` should be submitted to the cluster as a runnable file for machine. `“AETHERCELL_input1”` is a file used to define codes input values. Information in this file should involve details of medium refractive index, cytoplasm refractive index, calculation cube size in X,Y and Z directions, size of nucleus, number of mitochondria, incident light wavelength and polarization, incident light input power and calculation resolution. `“AETHERCELL_input2”` defines

the location and sizes of cell nucleus and each mitochondrion. After putting requested information needed to start the calculations in input files, the “\*.pbs” file should be submitted to the cluster using below line:

```
qsub *.pbs
```

The calculation will be started and the log will be saved in a “.txt” file. After calculations are done, the code will start to generate results in separate files. Each of these files provides information of different part of calculations. “\*.130” file is a file where information about calculated time-averaged intensity of each point is stored.

### **A.1.2. Extracting and plotting results input values**

“Omega” is a script written in Matlab to extract results from “\*.130” file(s). This code is capable to produce 3D matrix of calculated points and draw normalized overall scattered patterns. The code also uses spherical to flat screen projection function to define individual viewing windows in forward and side directions. This code also plots simulated results on a surface of sphere for better comparison with experimental results and understanding.

“Omega” is accessible to use through below direct link:

<https://goo.gl/5NybT0>

### **A.1.3. Spherical polystyrene bead**

The input file used to simulate spherical beads contains information as below:

```
n_multi,cp_period,Grid_max,refract_1,refract_2=
6.000000000000000      1000      60 1.334000000000000
1.590000000000000
```

```

X_sample,Y_sample,Z_sample,r_cell,n_cyto=
6.000000000000000E-006 6.000000000000000E-006 6.000000000000000E-006
3.000000000000000E-006      0
omega,power_in,e_amplitude,pola_angle,=
2.976693374381879E+015 1.000000000000000 1.000000000000000
0.000000000000000E+000
a_cyto,b_cyto,c_cyto,a_nucl,b_nucl,c_nucl,=
3.000000000000000E-006 3.000000000000000E-006 3.000000000000000E-006
3.000000000000000E-006 3.000000000000000E-006 3.000000000000000E-006
Alpha,Beta,Gamma,=
0.000000000000000E+000 0.000000000000000E+000 0.000000000000000E+000
n_theta,L_liao=
300      3
n_boundary,n_tfsf,n_nearfield =
25      9      6
run_flag=      2

```

This input file model a 6  $\mu\text{m}$  diameter bead with refractive index of 1.59 surrounded in a saline solution with refractive index of 1.334. The incident laser has frequency of 2.9766 or 632.8nm wavelength. Extracted results are shown in Chapter 3.

**A.1.4. Non-spherical polystyrene bead input values**

Non-spherical beads are modeled with different radii's in X,Y and Z direction while in case of rotation values for Alpha, Beta and Gamma can be modified for rotations along X, Y, and Z axis respectively.

n\_multi,cp\_period,Grid\_max,refract\_1,refract\_2=

6.0000000000000000 1000 60 1.3340000000000000

1.5900000000000000

X\_sample,Y\_sample,Z\_sample,r\_cell,n\_cyto=

6.0000000000000000E-006 6.0000000000000000E-006 6.0000000000000000E-006

3.0000000000000000E-006 0

omega,power\_in,e\_amplitude,pola\_angle,=

2.976693374381879E+015 1.0000000000000000 1.0000000000000000

0.0000000000000000E+000

a\_cyto,b\_cyto,c\_cyto,a\_nucl,b\_nucl,c\_nucl,=

2.0000000000000000E-006 3.0000000000000000E-006 2.0000000000000000E-006

2.0000000000000000E-006 3.0000000000000000E-006 2.0000000000000000E-006

Alpha,Beta,Gamma,=

0.0000000000000000E+000 0.0000000000000000E+000 0.0000000000000000E+000

n\_theta,L\_liao=

300 3

n\_boundary,n\_tfsf,n\_nearfield =

25      9      6

run\_flag=      2

This input file models a  $4 \times 6 \mu\text{m}$  non-spherical bead with refractive index of 1.59 surrounded by saline solution. Incident laser has wavelength of 632.8nm.

### A.1.5. Biological cell input values

Cells have internal structure that should be considered during simulations. “AETHERCELL\_input2” should provide information about location and sizes of cell nucleus and mitochondria. While a\_cyto,b\_cyto and c\_cyto define X,Y and Z direction length for cytoplasm, a\_nucl,b\_nucl and c\_nucl are dedicated for nucleus dimensions in X,Y and Z directions. “AETHERCELL\_input1” used for UCB VSEL first numerical model is as follows:

n\_multi,cp\_period,Grid\_max,refract\_1,refract\_2=

6.000000000000000      10000      20    1.334000000000000

1.350000000000000

X\_sample,Y\_sample,Z\_sample,r\_cell,n\_cyto=

8.000000000000000E-006    8.000000000000000E-006    8.000000000000000E-006

4.000000000000000E-006      20

omega,power\_in,e\_amplitude,pola\_angle,=

2.976693374381879E+015    1.000000000000000      1.000000000000000

0.000000000000000E+000

a\_cyto,b\_cyto,c\_cyto,a\_nucl,b\_nucl,c\_nucl,=

4.000000000000000E-006 4.000000000000000E-006 4.000000000000000E-006

1.000000000000000E-006 4.000000000000000E-006 1.000000000000000E-006

Alpha,Beta,Gamma,=

0.000000000000000E+000 0.000000000000000E+000 0.000000000000000E+000

n\_theta,L\_liao=

300 3

n\_boundary,n\_tfsf,n\_nearfield =

25 12 9

run\_flag= 2

Based on above input data, the cytoplasm has spherical shape with 4  $\mu\text{m}$  radius size and refractive index of 1.35. The nucleus has non-spherical shape of 1x4  $\mu\text{m}$  radii size. The refractive index and offset location for mitochondria and each mitochondrion is defined in “AETHERCELL\_input2” as below:

0.000000000000000E+000 0.000000000000000E+000 0.000000000000000E+000

0.000000000000000E+000 1.390000000000000

2.663624000000000E-006 -1.666014000000000E-006 -1.888133000000000E-006

2.250000000000000E-007 1.420000000000000

-2.796412000000000E-006 1.287446000000000E-006 -1.830830000000000E-006

2.250000000000000E-007 1.420000000000000

-2.747958000000000E-006 -1.394794000000000E-006 -1.888133000000000E-006

2.250000000000000E-007 1.420000000000000

-2.514153000000000E-006 -1.341986000000000E-006 -2.261105000000000E-006  
2.250000000000000E-007 1.420000000000000  
-1.063169000000000E-006 -1.006032000000000E-006 -2.998993000000000E-006  
2.250000000000000E-007 1.420000000000000  
1.147129000000000E-006 1.606475000000000E-006 2.900142000000000E-006  
2.250000000000000E-007 1.420000000000000  
1.254468000000000E-006 1.187361000000000E-006 2.974878000000000E-006  
2.250000000000000E-007 1.420000000000000  
-2.548222000000000E-006 2.217536000000000E-006 1.347296000000000E-006  
2.250000000000000E-007 1.420000000000000  
-1.903811000000000E-006 2.043054000000000E-006 -2.447468000000000E-006  
2.250000000000000E-007 1.420000000000000  
-1.935443000000000E-006 -1.950405000000000E-006 -2.490529000000000E-006  
2.250000000000000E-007 1.420000000000000  
1.171657000000000E-006 -1.081709000000000E-006 -2.990944000000000E-006  
2.250000000000000E-007 1.420000000000000  
1.333105000000000E-006 1.729398000000000E-006 2.832217000000000E-006  
2.250000000000000E-007 1.420000000000000  
-1.164285000000000E-006 -1.474670000000000E-006 2.935897000000000E-006  
2.250000000000000E-007 1.420000000000000  
-2.968666000000000E-006 -1.315009000000000E-006 -1.158500000000000E-006

2.2500000000000000E-007 1.4200000000000000  
 2.2571390000000000E-006 -2.5474110000000000E-006 1.1585000000000000E-006  
 2.2500000000000000E-007 1.4200000000000000  
 -2.2908360000000000E-006 2.1548780000000000E-006 -2.0000000000000000E-006  
 2.2500000000000000E-007 1.4200000000000000  
 -1.1583200000000000E-006 -2.9914510000000000E-006 -1.0951640000000000E-006  
 2.2500000000000000E-007 1.4200000000000000  
 -1.4761440000000000E-006 1.7156690000000000E-006 2.8058530000000000E-006  
 2.2500000000000000E-007 1.4200000000000000  
 -2.2229600000000000E-006 -1.7321900000000000E-006 2.4029500000000000E-006  
 2.2500000000000000E-007 1.4200000000000000  
 2.3996300000000000E-006 1.2697570000000000E-006 -2.4029500000000000E-006  
 2.2500000000000000E-007 1.4200000000000000

The first line of this file is dedicated for offset values for nucleus location inside the cell while the refractive index of 1.39 is defined for nucleus. Next lines define mitochondria X, Y and Z location while each has radius size of 250 nm and refractive index of 1.42.

## **A.2. Comments on laser used for light scattering of cells**

A Helium Neon continuous wave (CW) laser with wavelength of 632.8 nm has been the main light source used in this thesis work. However, there are other potential widely available CW lasers that could be potential candidates including lasers with wavelengths of 405 nm, 532 nm,

658 nm and 780 nm. Here, I will briefly discuss the trade-offs of these various options. Laser wavelength of 405nm has a short wavelength and the highest photon energy among these candidates and it thus has the most chance of damaging cells. Laser wavelength of 532 nm or 632.8 nm is typically used for cells studies using lasers and it includes the FACS machines. Available 532 nm laser source had a high power that produces unwanted background light due to laser reflection from other surfaces and adjacent beads or cells. Scattered light intensities increase with photon energies in the optical regime and thus the longer laser wavelength of 780 nm would lead to lower scattered light intensities. Thus 532 nm and 632.8 nm are the optimum choices for laser scattering of cell studies.

Mie theory simulations of light scattering patterns of 6  $\mu\text{m}$  and 10  $\mu\text{m}$  polystyrene microsphere beads with refractive index of 1.59 (at  $\lambda = 632.8$  nm) surrounded in PBS medium with refractive index of 1.334 (at  $\lambda = 632.8$  nm) are shown Figure A.1 and A.2 in respectively. As shown in Figure A.1 plots “A” and “B”, comparison between wavelength 632.8 nm with 405 nm and 780 nm in forward and side directions, scores 405 nm that produces higher number of fringes with better contrast of local maxima and minima of each peak. Although, as 405 nm has higher photon energy and there is a bigger chance of damaging the cells. 780 nm wavelength produces less number of fringes and it has lower scattered intensity light due to its lower photon energy. Based on what has been discussed, 632.8 nm is a good choice in compare to 405nm and 780 nm with adequate photon energy and easily detectable scattered light.

Comparison between other wavelengths of 532 nm and 658 nm with 632.8 nm shows similar results as shown in plots “C” and “D”. All these wavelengths show similar scattered light

contrast with almost similar resolution of 5 and 5-6 fringes in forward and side directions. Any laser source with a wavelength range of 532-658 nm can be used depending on the availability.

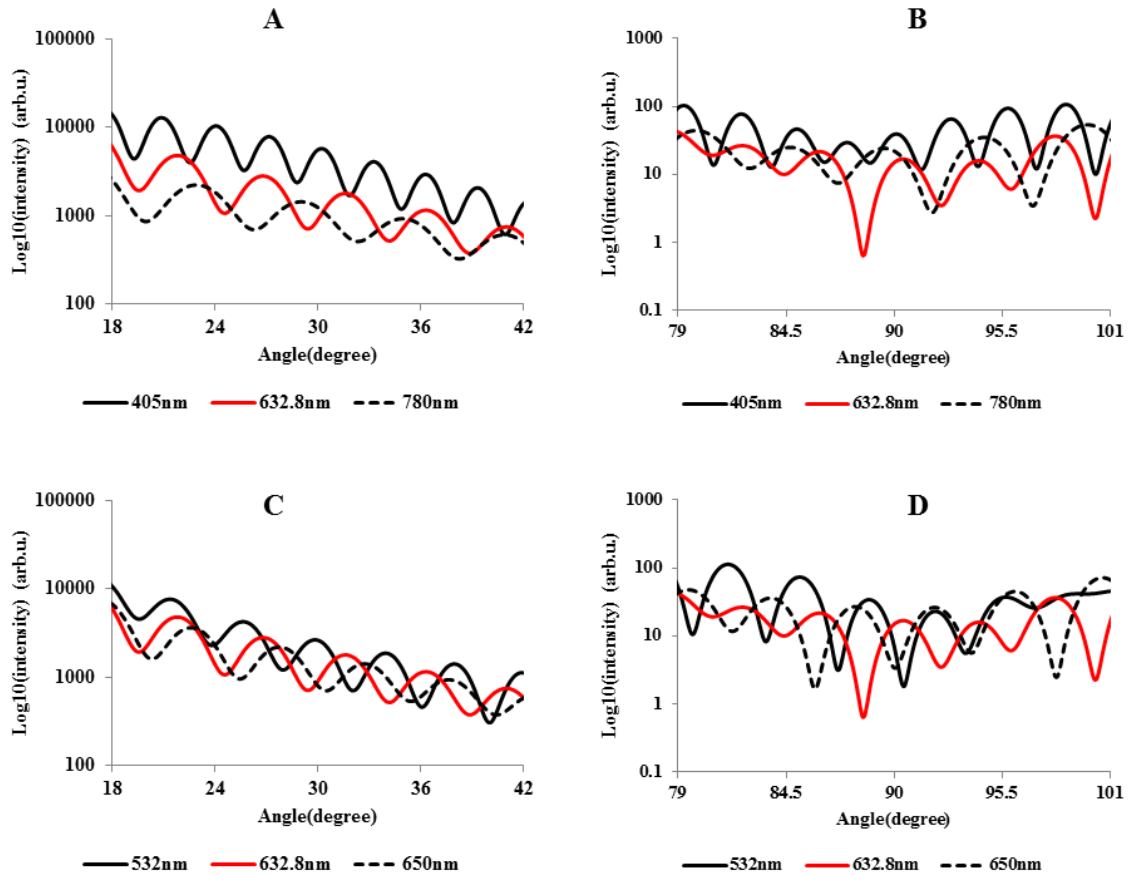


**Figure A.1:** Different laser wavelength study for 6  $\mu\text{m}$  polystyrene bead is presented in both forward and side directions. Plot “A” compares forward direction results for 632.8nm with 405nm and 780 nm and plot “B” do similar comparison in side direction. Plot “C” compares forward direction results for 632.8nm with 532 nm and 650 nm and plot “D” do similar comparison in side direction.

10  $\mu\text{m}$  bead’s simulated scattered results of forward and side directions for different wavelengths are shown in Figure A.2. Plotted results have similar understanding as what has been described for 6  $\mu\text{m}$  bead. Comparing the results and based on the availability of the laser sources, 632.8nm was practiced in this thesis project.

Practically observed scattered patterns in side direction of 6  $\mu\text{m}$  and 10  $\mu\text{m}$  at 405 nm and 658 nm were compared with simulated Mie theory results. Good agreement exists between

experimental and simulated results number of the fringes. Depending on the resolution needed and useful laser power, different wavelengths other than 632.8nm may be applied for further applications. Further studies may be implemented for counting the number of photons in each pattern for better understanding and comparisons between collected results.

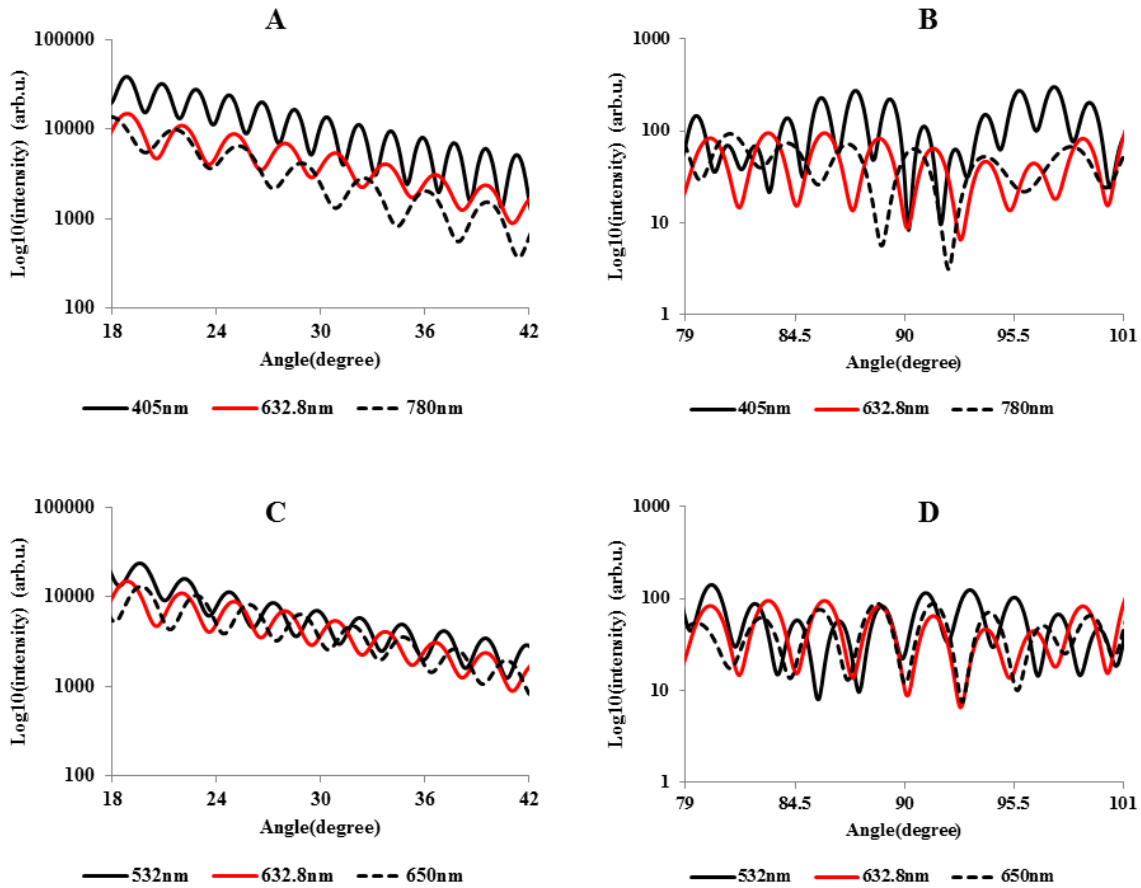


**Figure A.2: Different laser wavelength study for 10  $\mu\text{m}$  polystyrene bead is presented in both forward and side directions. Plot “A” compares forward direction results for 632.8nm with 405nm and 780 nm and plot “B” do similar comparison in side direction. Plot “C” compares forward direction results for 632.8nm with 532  $\mu$  and 650 nm and plot “D” do similar comparison in side direction.**

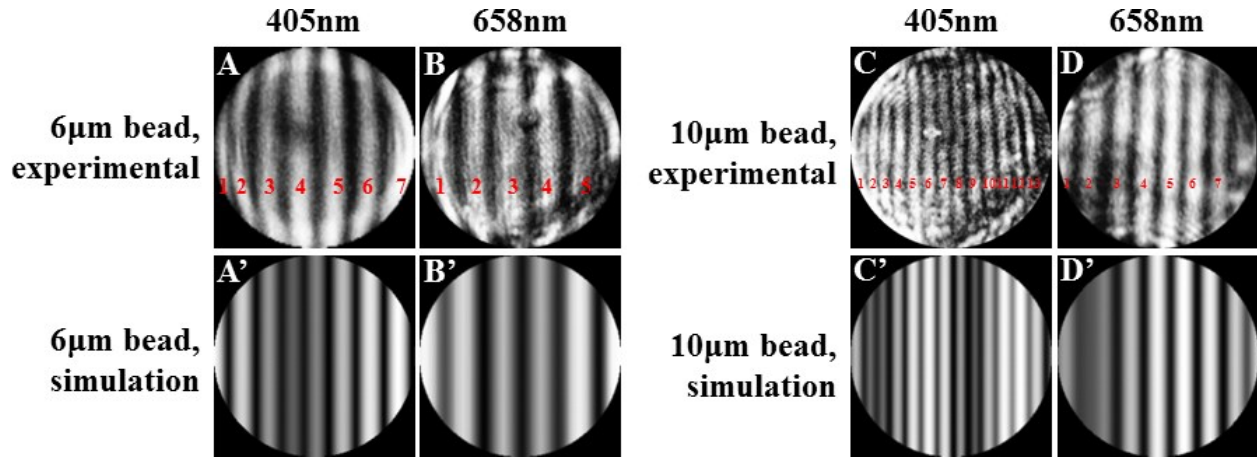


Figure A.3: 6  $\mu\text{m}$  bead experimentally side scattered patterns are observed as shown in “A” and “B”. Mie theory 2D simulated patterns are shown in “A’” and “B’”. 10  $\mu\text{m}$  bead experimental and simulated results are shown in “C”, “D”, “C’” and “D’”.

### A.3. Speckle analysis

Speckle analysis has been used to compare generated results in side direction 2D light scattered patterns of UCB HSCs. This has been preceded by identifying local maxima and counting them. The size of each speckle is characterized by calculating an area corresponding to half value of its maximum intensity (FWHM). The number of speckles and the average area were used to construct a 2D plot that includes results of experimental measurements and simulations. Contour plots make it easier to calculate the area of each intensity peak based on FWHM value. As shown in Figure A.4, contour function were used to plot 10 levels contour map of grayscale 2D light scattered pattern “A” as shown in “B”. In this pattern there are 10 local maximas. The size of each local maxima was characterized as a corresponding area confined from the maximum of the peak to the half value of its maximum. In this particular case the average area of all 10 local maximas is 12091 pixels. All the compared patterns were resized to the same image size of  $600 \times 600$  pixels and 8-bit image grayscale type.

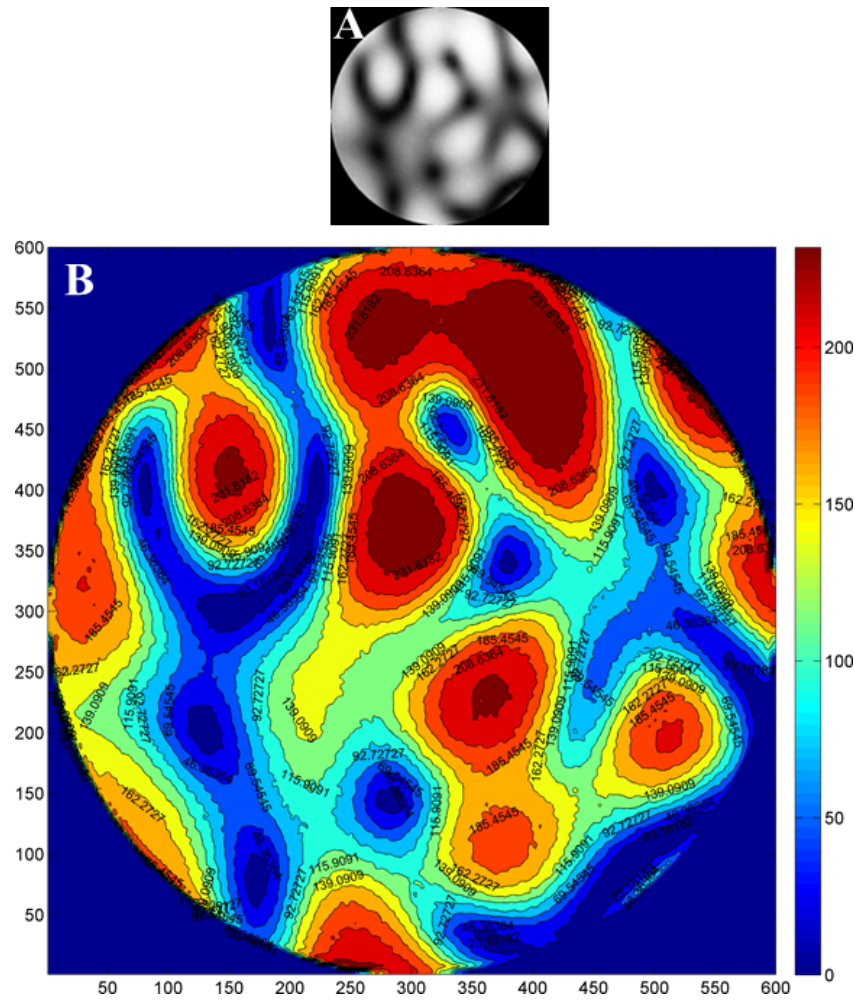


Figure A.4: Contour function was used to calculate the FWHM value of each local maxima.